REPUBLIC OF TURKEY

YILDIZ TECHNICAL UNIVERSITY

GRADUATE SCHOOL OF SCIENCE AND ENGINEERING

INVESTIGATION, DESIGN AND CHARACTERIZATION OF LUMINESCENCE PROPERTIES OF RARE EARTH ELEMENTS ON GLASS-CERAMIC COATINGS

Abdi SOYLU

MASTER OF SCIENCE THESIS

Department of Metallurgical and Materials Engineering

Material Program

Supervisor

Assoc. Prof. Dr. Buğra ÇİÇEK

June, 2023

REPUBLIC OF TURKEY

YILDIZ TECHNICAL UNIVERSITY

GRADUATE SCHOOL OF SCIENCE AND ENGINEERING

INVESTIGATION, DESIGN AND CHARACTERIZATION OF LUMINESCENCE PROPERTIES OF RARE EARTH ELEMENTS ON GLASS-CERAMIC COATINGS

A thesis submitted by Abdi SOYLU in partial fulfillment of the requirements for the degree of MASTER OF SCIENCE is approved by the committee on 23.06.2023 in Department of Metallurgical and Materials Engineering, Material Program.

Assoc. Prof. Dr. Buğra ÇİÇEK
Yıldız Technical University
Advisor

Approved By the Examining Committee

Assoc. Prof. Dr. Buğra ÇİÇEK, Advisor
Yildiz Technical University _____

Assoc. Prof. Dr. Metin GENÇTEN, Member
Yildiz Technical University _____

Prof Dr. Recep ARTIR, Member
Marmara University _____

I hereby declare that I have obtained the required legal permissions during data collection and exploitation procedures, that I have made the in-text citations and cited the references properly, that I haven't falsified and/or fabricated research data and results of the study and that I have abided by the principles of the scientific research and ethics during my Thesis Study under the title of Investigation, Design and Characterization of Luminescence Properties of Rare Earth Elements on Glass-Ceramic supervised by my supervisor, Assoc. Prof. Dr. Buğra ÇİÇEK. In the case of a discovery of false statement, I am to acknowledge any legal consequence.

Abdi SOYLU

Signature

Dedicated to my family

and my best friends

ACKNOWLEDGEMENTS

First and foremost, I would like to express my heartfelt gratitude to my respected advisor Assoc. Prof. Buğra Çiçek, who never withheld his support from me throughout the project.

I will always remember the motivation that my dear friend Nurullah Çöpoğlu provided me during the project and also his priceless friendship.

I also would like to thank all the members of Akcoat Advanced Chemical Coating Materials Co.'s Enamel Solutions Research & Development Department, especially Tamer Cengiz and Murat Kaya, for providing me with unique and invaluable knowledge and experience.

I extend my gratitude and appreciation to our mentor, Dr. Oğuz Karaahmet, who always aims to improve and guide us in our professional lives.

Above all, I would like to express my gratitude to my family, who supported me in every situation, never withheld their love, and stood behind me in all my decisions, as well as my friends whom I love as much as my family.

Abdi SOYLU

TABLE OF CONTENTS

LIST OF SYMBOLS viii
LIST OF ABBREVIATIONS ix
LIST OF FIGURES x
LIST OF TABLES xii
ABSTRACT xiii
ÖZET xv
1 INTRODUCTION 1
1.1 Literature Review 1
1.2 Objectives of Thesis 4
1.3 Hypothesis 4
2 GLASS-CERAMIC 5
2.1 Definition 5
2.2 Manufacturing Methods of Precursor Glass 8
2.3 Characteristics of Glass-Ceramics 9
2.4 Usage Area of Glass-Ceramics 9
3 GLASS-CERAMIC COATING 16
3.1 Definition of Glass-Ceramic Coating on Metal Substrates (i.e. Enamel) 16
3.2 Chemical Design of Glass-Ceramic Coating 17
3.3 Adhesion Mechanism 22
3.4 Properties of Glass-Ceramic Coating 24
3.5 Application Areas of Glass-Ceramic Coatings 31
3.6 Coating Methods for Glass-Ceramic Coatings 32
4 LUMINESCENCE MATERIALS 35
4.1 Definition of Luminescence 35
4.2 Type of Luminescence 37
4.3 Types of Phosphorus 38
4.4 Mechanism of Long-Lasting Luminescence 39
4.5 The Mechanism of Energy Transfer Method 44
4.6 Activator Atoms 44
4.7 Some of Application Areas 47
5 EXPERIMENTAL PROCEDURE 49
5.1 Materials 49

5.2 Synthesis of Pr^{+3}/Dy^{+3} co-doped and Er^{+3}/Dy^{+3} co-doped $SrAl_2Si_2O_8$ 49
5.3 Frit Preparation 50
5.4 Sample Preparation 50
5.5 Coating Procedures 52
6 CHARACTERIZATION PROCEDURE **54**
6.1 Chemical analysis 54
6.2 Phase Analysis 54
6.3 Microstructural analysis 54
6.4 Thermal Analysis 55
6.5 Optical Analysis 55
6.6 Chemical Corrosion Resistance Analysis 55
6.7 Surface Profilometer 55
6.8 Gloss Determination 56
6.9 Thickness measurement 56
7 RESULT AND DISCUSSION **57**
7.1 Characterization of Glass-Ceramic Coating 57
7.2 Characterization of $SrAl_2Si_2O_8$ 61
7.3 Characterization of Coating Samples (with added $SrAl_2Si_2O_8:Pr^{3+},Dy^{3+}$) 68
7.4 Characterization of Coating Samples (with added $SrAl_2Si_2O_8:Er^{3+},Dy^{3+}$) 80
7.5 Comparison of The Photoluminescent Characteristics of $SrAl_2Si_2O_8:Pr^{3+}$, Dy^{3+} and $SrAl_2Si_2O_8:Er^{3+}$, Dy^{3+} Doped Coatings 92
CONCLUSIONS **94**
REFERENCES **96**
PUBLICATIONS **108**

LIST OF SYMBOLS

°C	Celcius Degree
cm	Centimeter
Dy	Dysprosium
eV	Electronvolt
W	Watt
ΔE	Energy Difference
Er	Erbium
GPa	Giga Pascal
GU	Gloss
g	Gram
c	Heat Capacity
MPa	Mega Pascal
μm	Micrometer
mL	Mililiter
nm	Nanometer
N	Newton
Pr	Praseodymium
Ra	Average Roughness
sec	Second
Δt	Temperature Difference
λ	Thermal Conductivity
β	Volumetric Thermal Expension
wt%	Weight Percent

LIST OF ABBREVIATIONS

ADL	Activities of Daily Life
CIE	Commission Internationale de l´Eclairage
CB	Conducting Band
DIN	Deutsche Institut für Normung
DTA	Differential Thermal Analysis
EDS	Energy-Dispersive X-Ray Spectroscopy
EN	European Norm
GC	Glass-Ceramic
IEI	International Enamellers Institute
ISO	International Organization for Standardization
ISC	Intersystem Crossing
LED	Light Emitting Diode
LCD	Liquid Crystal Display
LPP	Luminescent Persistent Phenomenon
Min	Minute
PersL	Persistant Luminescence
PEI	Porcelain Enamel Institute
SEM	Scanning Electron Microscopy
UK	United Kingdom
VB	Valance Band
VEA	Vitreous Enamel Association
XRD	X-Ray Diffraction
XRF	X-Ray Fluorescence

LIST OF FIGURES

Figure 2.1 The process of converting the precursor glass into a glass-ceramic structure involves a series of steps, which (a) commence with the creation of nuclei, (b) succeeded by the development of crystals on the nuclei, and (c) culminate in the formation of the glass-ceramic. **7**

Figure 2.2 The association between crystal development and uniform nucleation during temperature change. **7**

Figure 3.1 The illustration of Ellingham's diagram **23**

Figure 3.2 The association between temperature change and viscosity in a glass structure. **28**

Figure 4.1 The depiction of the hole model proposed by Matsuzawa et al. through the utilization of $SrAl_2O_4:Eu^{2+},Dy^{3+}$. **41**

Figure 4.2 The depiction of the electron model proposed by Aitasalo et al. through the utilization of $CaAl_2O_4:Eu^{2+},Dy^{3+}$. **42**

Figure 4.3 The long-lasting luminescence mechanism proposed by Dorenbos et al. ... **42**

Figure 4.4 Trap depths belonging to rare earth element **43**

Figure 4.5 The diagram presented is a simplified form of the Jablonsky diagram. **44**

Figure 4.6 The internal structure of a fluorescent tube **47**

Figure 4.7 The cathode ray tube **48**

Figure 5.1 Representation of the steps involved in the synthesis process of the Pr^{+3}/Dy^{+3} co-doped and Er^{+3}/Dy^{+3} co-doped $SrAl_2Si_2O_8$ systems. **50**

Figure 5.2 Representation of the steps involved in the coating process. 53

Figure 7.1 Specific temperature points and behaviors of traditional coating samples in the analysis of the thermal microscope. **59**

Figure 7.2 SEM images of standart coat at a) 100µm and b) 50µm and mapping images of c) standart, d) Fe, e) Ca, f) Ti, g) Zn and h) C elements using EDS analysis. **60**

Figure 7.3 SEM images of the (a) standard coating show (d) the dentritic structures formed between the metal substrate (downside) and the ground coating (upside), as well as (c) the adhesion between the ground coat (downside) and intermediate coat (upside) and (b) between the intermediate coat(downside) and top coat (upside). **61**

Figure 7.4 The Raman spectrum analysis of the $SrAl_2Si_2O_8$ glass-ceramic system. **64**

Figure 7.5 The differential thermal analysis (DTA) of the $SrAl_2Si_2O_8$ glass-ceramic system. **65**

Figure 7.6 X-ray diffraction (XRD) analysis graphs of the precursor glass structure of $SrAl_2Si_2O_8$ and the after-crystallization process conducted at varying temperatures of 700°C, 763°C, 820°C, and 1000°C. **66**

Figure 7.7 Scanning electron microscopy (SEM) images were obtained for glass-ceramic coatings containing different ratios of $SrAl_2Si_2O_8:Pr^{3+},Dy^{3+}$, with measurements taken at 100 μm and 50 μm. **69**

Figure 7.8 3D topography maps for standard glass ceramic coating and glass ceramic coating doped with $SrAl_2Si_2O_8:Pr^{3+}$, Dy^{3+}. **73**

Figure 7.9 Emission graph of various proportions of $SrAl_2Si_2O_8:Pr^{3+}$, Dy^{3+} particles doped and undoped transparent glass-ceramic coating..... **75**

Figure 7.10 Illustration of the energy band diagrams that show the energies of Pr^{3+} and Dy^{3+}..... **76**

Figure 7.11 CIE 1931 chromatography diagram of glass-ceramic coatings with various proportions of $SrAl_2Si_2O_8:Pr^{3+}$, Dy^{3+}. **79**

Figure 7.12 Scanning electron microscopy (SEM) images were obtained for glass-ceramic coatings containing different ratios of $SrAl_2Si_2O_8:Er^{3+}$, Dy^{3+}, with measurements taken at 100 μm and 40 μm. **81**

Figure 7.13 3D topography maps for standard glass ceramic coating and glass ceramic coating doped with $SrAl_2Si_2O_8:Er^{3+}$, Dy^{3+}. **85**

Figure 7.14 Emission graph of various proportions of $SrAl_2Si_2O_8:Er^{3+}$, Dy^{3+} particles doped and undoped transparent glass-ceramic coating. **87**

Figure 7.15 Illustration of the energy band diagrams that show the energies of Er^{3+} and Dy^{3+}..... **89**

Figure 7.16 CIE 1931 chromatography diagram of glass-ceramic coatings with various proportions of $SrAl_2Si_2O_8:Er^{3+}$, Dy^{3+}. **92**

LIST OF TABLES

Table 2.1 An overview of the main crystalline phases, their properties, and application areas of selected glass-ceramic systems. **9**

Table 3.1 The functions of the oxides present in the glass-ceramic system, as well as the sources of these oxides in the raw materials utilized in the system. **18**

Table 3.2 The categorization of oxides based on their roles in the glass structure **20**

Table 3.3 The coefficients of cubical thermal expansion that several glass-ceramic coatings and some metals exhibit. **25**

Table 5.1 The theoretical composition of oxides in the specimens. **49**

Table 5.2 The recipes of the ground, intermediate and top coats. 51

Table 5.3 Denotations of the samples. **52**

Table 5.4 Elemental composition of metal substrate **53**

Table 7.1 The oxide composition of traditional coatings. **57**

Table 7.2 Specific temperature points and behaviors of traditional coating samples in the analysis of the thermal microscope.. ..... **59**

Table 7.3 The XRF analysis result of $SrAl_2Si_2O_8$ system. **62**

Table 7.4 The result of the cold citric acid test applied to samples that is standard, 5Pr, 10Pr, 20Pr and 40Pr 70

Table 7.5 Gloss analysis at 60° for standard glass-ceramic coating and glass-ceramic coating doped with $SrAl_2Si_2O_8:Pr^{3+},Dy^{3+}$ **71**

Table 7.6 The roughness values (Ra) for the standard glass ceramic coating and the glass ceramic coating doped with $SrAl_2Si_2O_8:Pr^{3+}$, Dy^{3+}, computed using the ConfoMAP software on 3D surface topography. **72**

Table 7.7 CIE 1931 chromaticity coordinates of $SrAl_2Si_2O_8:Pr^{3+}$, Dy^{3+} particles doped and Undoped transparent glass-ceramic coatings. **78**

Table 7.8 The result of the cold citric acid test applied to samples that is standard, 5Er, 10Er, 20Er, 40Er. **82**

Table 7.9 Gloss analysis at 60° for standard glass-ceramic coating and glass-ceramic coating doped with $SrAl_2Si_2O_8:Er^{3+}$, Dy^{3+} **83**

Table 7.10 The roughness values for the standard glass ceramic coating and the glass ceramic coating doped with $SrAl_2Si_2O_8:Er^{3+}$, Dy^{3+} , computed using the ConfoMAP software on 3D surface topography. **84**

Table 7.11 CIE 1931 chromaticity coordinates of $SrAl_2Si_2O_8:Er^{3+}$, Dy^{3+} particles doped and undoped transparent glass-ceramic coatings. **91**

ABSTRACT

Investigation, Design and Characterization of Luminescence Properties of Rare Earth Elements on Glass-Ceramic Coatings

Abdi SOYLU

Department of Metallurgical and Materials Engineering

Master of Science Thesis

Supervisor: Assoc. Prof. Dr. Buğra ÇİÇEK

Glass-ceramic materials are inorganic composites made of ceramic crystals produced in a glass matrix by controlled crystallization. Glass-ceramic composites are impact-resistant, chemically stable, thermally shock-resistant, and optically adjustable. Due to its vitreous composition, glass-ceramic coating technique protects metal substrates and improves their appearance.

The global issue of areas requiring electric illumination, especially those with high energy consumption and the resulting increase in carbon footprint, as billboards, signboards, etc., is cause for concern. It is crucial to employ ecologically sustainable materials in these fields. Glass-ceramic coatings that exhibit luminescent properties are known for their advantageous attributes, including superior chemical stability, notable impact resistance, and attractive appearance. These features render them a valuable asset in promoting energy efficiency and mitigating carbon emissions.

The objective of this investigation is to gain luminescent characteristics to glass-ceramic coatings through the incorporation of $SrAl_2Si_2O_8$: Pr^{3+}, Dy^{3+} and $SrAl_2Si_2O_8$: Er^{3+}, Dy^{3+} glass-ceramic systems into the glass-ceramic coating. Erbium, praseodymium, and dysprosium were incorporated into the $SrAl_2Si_2O_8$ matrix to generate luminescent centers, owing to their strong emission characteristics arising from electronic transitions. After

melting at 1550°C for 1 hour, the glass-ceramic systems $SrAl_2Si_2O_8:Pr^{3+}$, Dy^{3+} and $SrAl_2Si_2O_8:Er^{3+}$, Dy^{3+} were produced via melt-quenching method. The metal substrate samples were prepared for the top coat application by applying ground and intermediate coat. The aforementioned substances were incorporated into the SiO_2-B_2O_3-Na_2O-ZnO-based transparent glass-ceramic coating in proportions of 5%wt, 10%wt, 20%wt, and 40%wt as a milling additive, and subsequently administered to the intermediate coat through the aqueous spray application technique. The glass-ceramic particles of $SrAl_2Si_2O_8:Pr^{3+}$, Dy^{3+} and $SrAl_2Si_2O_8:Er^{3+}$, Dy^{3+} conducted multiple analyses including X-ray fluorescence (XRF), X-ray diffraction (XRD), differential thermal analysis (DTA), and Raman spectroscopy. The instruments, including SEM, spectrofluorometry, and optic microscope for 3D surface mapping, were employed to examine the coated sample surfaces.

Upon conducting spectrofluorometric analysis on the samples, it was observed that the transparent glass-ceramic coating sample that remained unmodified did not demonstrate any discernible emission peaks. As the number of doping substances was elevated in the doped specimens, various emission peaks were observed at particular wavelengths, and their intensities progressively amplified. The coatings doped with $SrAl_2Si_2O_8:Pr^{3+}$, Dy^{3+} exhibited emissions at 485 nm and 575 nm, which corresponded to the $Pr^{3+}(^3P_0 \rightarrow {}^3H_4)$, $Dy^{3+}(^4F_{9/2} \rightarrow {}^6H_{15/2})$, and $Dy^{3+}(^4F_{9/2} \rightarrow {}^6H_{15/2})$ energy band transitions, respectively. The coatings that were doped with $SrAl_2Si_2O_8$: Er^{3+}, Dy^{3+} exhibited emissions at distinct wavelengths, namely 450 nm, 480 nm, 500 nm, 550 nm, 570 nm, and 660 nm, which corresponded to the $Dy^{3+}(^4I_{15/2} \rightarrow {}^6H_{15/2})$, $Dy^{3+}(^4F_{9/2} \rightarrow {}^6H_{15/2})$, $Er^{3+}(^2H_{11/2} \rightarrow {}^4I_{15/2})$, $Er^{3+}(^4S_{3/2} \rightarrow {}^4I_{15/2})$, $Dy^{3+}(^4F_{9/2} \rightarrow {}^6H_{13/2})$, and $Dy^{3+}(^4F_{9/2} \rightarrow {}^6H_{11/2})$ energy band transitions.

This research has proposed a resolution, specifically for sectors that consume high levels of energy, such as the advertising and lighting industries, through the integration of luminescent characteristics into glass-ceramic coatings. Furthermore, the aforementioned solution exhibits characteristics that are both environmentally sustainable and durable, including energy efficiency, low carbon emissions, ease of production, high chemical stability, and high impact resistance.

Keywords: Luminescence, Glass-Ceramic, Coating, Rare-Earth Elements

ÖZET

Cam-Seramik Kaplamalarda Nadir Toprak Elementlerinin Lüminesans Özelliklerinin İncelenmesi, Tasarımı ve Karakterizasyonu

Abdi SOYLU

Metalurji ve Malzeme Mühendisliği Departmanı

Yüksek Lisans Tezi

Danışman: Doç. Dr. Buğra ÇİÇEK

Cam-seramik malzemeler, cam matris içerisinde kontrollü kristalizasyon yöntemi ile oluşturulan seramik kristaller içeren bir inorganik kompozit malzemedir. Cam seramik kompozit malzemeler, yüksek darbe dayanımı, yüksek kimyasal kararlılık, yüksek termal şok dayanımı, ayarlanabilir optik özellikleri gibi birçok özelliklere sahiptir. Cam-seramik kaplama teknolojisi, metal altlığın korunması ve cam-seramik kaplamanın vitröz yapısı sayesinde kaplanan metale estetik bir görünüm kazandırmaktadır.

Özellikle elektrik ile aydınlatma gerektiren alanlar, yüksek enerji tüketimi ve buna bağlı olarak artan karbon ayak izi küresel bir sorun teşkil etmektedir. Bu alanlarda çevre dostu malzemelerin kullanımı oldukça önemlidir. Bu nedenle yüksek kimyasal kararlılık, yüksek darbe direnci ve estetik görünüme sahip olan cam-seramik kaplamalar kazandırılan lüminesans özellik ile enerji tasarrufu ve düşük karbon salınımına katkı sağlamaktadır.

Bu araştırma, $SrAl_2Si_2O_8:Pr^{3+}$, Dy^{3+} ve $SrAl_2Si_2O_8:Er^{3+}$, Dy^{3+} cam-seramik sistemlerinin cam-seramik kaplamaya dahil edilmesiyle cam-seramik kaplamalara lüminesans

özellikleri kazandırmayı amaçlamaktadır. Erbiyum, praseodim ve disprosyum, elektronik geçişlerden kaynaklanan güçlü emisyon özelliklerinden dolayı, lüminesans merkezleri oluşturmak için $SrAl_2Si_2O_8$ matrisine dahil edilmiştir. 1550°C'de 1 saat eritildikten sonra eriterek söndürme yöntemiyle $SrAl_2Si_2O_8:Pr^{3+}$, Dy^{3+} ve $SrAl_2Si_2O_8:Er^{3+}$, Dy^{3+} cam-seramik sistemler üretilmiştir. Metal altlık numunelerin üzerine astar kat ve ara kat uygulaması yapılarak üst kat uygulamaya hazır hale getirilmiştir. Elde edilen bu malzemeler, transparan cam-seramik kaplama içerisine ağırlıkça %5, %10, %20 ve %40 oranlarda değirmen katkısı olarak eklenmiş ve sulu sprey uygulama yöntemi ile ara kat üzerine uygulanmıştır. $SrAl_2Si_2O_8$: Pr^{3+}, Dy^{3+} ve $SrAl_2Si_2O_8$: Er^{3+}, Dy^{3+} cam-seramik partikülleri XRF, XRD, DTA ve raman gibi çeşitli analizlere tabi tutulmuştur. Kaplanmış numune yüzeylerinin incelemesi için SEM, spektroflorometre ve 3D yüzey haritalaması için optik mikroskop gibi çeşitli araçlar kullanıldı.

Spektroflorometre analizleri yapılan numuneler için, katkılanmamış transparan cam-seramik kaplama numunesi herhangi bir emisyon pikine sahip olmamasına rağmen, katkılanmış numunelerin ağırlıkça katkı yüzdesi arttıkça belirli dalgaboylarında emisyon pikleri oluştuğu ve bu piklerin giderek yoğunlaştığı gözlemlenmiştir. Bu emisyonlar, $SrAl_2Si_2O_8:Pr^{3+}$, Dy^{3+} katkısı yapılmış kaplamalar için 485 nm ve 575 nm dalgaboylarında gerçekleşmiştir ve bu emisyonlar sırasıyla $Pr^{3+}(^3P_0 \rightarrow {}^3H_4)$, $Dy^{3+}(^4F_{9/2} \rightarrow {}^6H_{15/2})$ ve $Dy^{3+}(^4F_{9/2} \rightarrow {}^6H_{15/2})$ enerji band geçişlerini temsil eder. $SrAl_2Si_2O_8:Er^{3+}$, Dy^{3+} katkısı yapılmış kaplamalar için ise 450nm, 480nm, 500nm, 550nm, 570nm, ve 660nm dalgaboylarında emisyon gerçekleşmiştir ve Bu emisyonlar sırasıyla $Dy^{3+}(^4I_{15/2} \rightarrow {}^6H_{15/2})$, $Dy^{3+}(^4F_{9/2} \rightarrow {}^6H_{15/2})$, $Er^{3+}(^2H_{11/2} \rightarrow {}^4I_{15/2})$, $Er^{3+}(^4S_{3/2} \rightarrow {}^4I_{15/2})$, $Dy^{3+}(^4F_{9/2} \rightarrow {}^6H_{13/2})$, ve $Dy^{3+}(^4F_{9/2}$ - $^6H_{11/2})$ enerji band geçişlerini temsil etmektedir.

Bu çalışma, cam-seramik kaplamalara lüminesans özellik kazandırılması ile özellikle reklam ve aydınlatma endüstrisi gibi enerji sarfiyatının yüksek olduğu alanlara çözüm olacağı düşünülmektedir. Ayrıca enerji verimliliği, düşük karbon salınımı, kolay üretilebilir olması, yüksek kimyasal kararlılığı ve yüksek darbe dayanımı ile çevre dostu ve uzun ömürlüdür.

Anahtar Kelimeler: Lüminesans, Cam-seramik, Kaplama, Nadir Toprak Elementleri

1
INTRODUCTION

1.1 Literature Review

The discovery of lighting has significantly enhanced the standards of human life, resulting in notable transformations. The progression of lighting technology, which originated with the use of wood flames experienced a notable acceleration with the introduction of electricity. The advancement of lighting technologies has been accelerated by the innovation of incandescent lamps, which have subsequently led to the emergence of fluorescent and LED innovations. The aforementioned occurrences have had a notable impact on both our professional and personal spheres [1].

The term "luminescence," derived from the Latin word "lumen," which means "light," was used in 1888 by German scientist Eilhard Wiedemann to characterize all light phenomena that did not rely on temperature increase. The first philosophical study of the luminescence phenomena may be found in Aristotle's "De Anima," [2] where he recorded his observations of nature and his surroundings. An important discovery was made by Italian chemist Vincentinus Casciarolo at the beginning of the 17th century. At the base of a volcano, he discovered barium sulfate ($BaSO_4$), a brilliant and heavy stone. It changed into a material that emitted red light in the absence of sunlight when he heated it up in a furnace [3]. He so created the name "phosphor" and categorized it as a luminous substance. The investigation of inorganic luminescent materials through systematic scientific studies was initiated in the 19th century by notable scientists such as Becquerel, Verneul, Lenard, and Stoke. In 1852, G.C. Stoke, a physicist from Britain, demonstrated that the exposure of a substance to light of a specific wavelength resulted in the emission of light of longer wavelength [4].

Until the early 1900s, Philip E.A. Lenard and his colleagues [5] undertook extensive research on phosphors within the confines of Germany. This involved the synthesis of diverse phosphors, including sulfides and selenites of alkaline earth metals, as well as ZnS, which were doped with luminescent activators to generate luminescent centers in the host material. During the 1930s, P. W. Pohl and his associates developed phosphors consisting of single crystals. They also worked alongside F. Seitz in the United States to

establish configuration-coordinate models for luminescent centers, which served as the basis for contemporary luminescence physics. The discovery made by McKeag and his colleagues [6] in 1942 involved the substitution of calcium and antimony for cadmium in the $3Cd_3(PO_4)_2 \cdot CdCl_2:Mn^{2+}$ compound, resulting in the absorption of UV light and subsequent emission of white light by the phosphor. During the initial years of the 1950s, DL lamps is the European type were manufactured by utilizing a combination of $Ca_3(PO_4)_2$ phosphor and $Mg_3(AsO_4)_2$ phosphor. Until the early 2000s, the lighting industry underwent numerous advancements, culminating in the replacement of chemically unstable precursors with $Sr_2Al_2O_4$ phosphors [7].

In 1996, the $Sr_2Al_2O_4$: Eu^{2+}, Dy^{3+} phosphor was discovered by T. Matsuzawa and colleagues [8]. This phosphor exhibited superior chemical stability and thermal durability, higher luminance intensity, and significantly longer afterglow time compared to conventional phosphors. The discovery was made through research conducted on the $Sr_2Al_2O_4$: Eu^{2+} phosphor previously discovered by Abbsuscato [3].Therefore, owing to its ability to emit light for a duration of 16 hours, it had the possibility to offer illumination throughout the night. This invention promised potential for diverse applications, including but not limited to display technologies [3], [6], [9]. Despite possessing more effective phosphorescent and stability features, the utility of aluminates has been progressively constrained owing to their susceptibility to degradation upon exposure to moisture, leading to their gradual replacement by silicate phosphors. The commercial utilization of aluminate phosphors has been progressively expanding since their initial discovery [10].

Aluminosilicate compounds are good candidates as host structures due to several advantages, such as excellent physical and chemical properties, high efficiency and thermal stability [11]–[13]. In 2007, Zhiyu Wang et al. reported luminescence resulting from the co-doping of Eu^{2+} and Dy^{3+} into the $SrAl_2Si_2O_8$ host structure. The solid solution made from Sr-feldspar ($SrAl_2Si_2O_8:Eu^{+2},Dy^{+3}$) was synthesized through solid-state reaction by Zhiyu Wang et al. It was found that the material exhibits light emission within a wavelength spectrum of 406nm to 440nm, and the luminescence intensity can be modified by the Sr concentration [14].

Bismuth phosphate glasses with fluorides, with varying modifiers, doped with Pr^{3+} and Dy^{3+}/Pr^{3+} ions were procured and analyzed by M. Kumar and his collaborators through regular glass melting techniques. The researchers noted that the aforementioned systems

possess appealing characteristics, including elevated refractive indices, comparably economical cost, and reduced melting points. The study conducted a comparison of optical improvements and improve bandwidths in various bismuth phosphate glasses, specifically in Pr^{3+}-doped and Dy^{3+}/Pr^{3+}-codoped glasses. The researchers observed that all of the acquired glasses displayed a prominent orange-red luminescence [15].

The spectroscopic properties of titanium tellurite glasses were examined by Z. Xiao and colleagues through the inclusion of Er^{3+} and Dy^{3+} dopants. This investigation involved the examination of alterations in the spectroscopic characteristics of the titanium tellurite glass system through the incorporation of Dy^{3+} dopants at varying mole ratios. The specimens were procured through conventional melting techniques at a temperature of 900°C and underwent precursor glass annealing and cooling procedures. The researchers were able to obtain five distinct photoluminescence emissions at wavelengths of 484 nm, 574 nm, 523 nm, 546 nm, and 656 nm as a consequence of their experiments. The researchers arrived at the conclusion that the magnitudes of stated wavelengths could be modified through the control of the concentration of the corresponding rare earth element within the glass composition. Furthermore, they posited that these glass materials could be effectively utilized in the development of lighting systems and displays featuring a diverse range of colors [16].

The objective of X. Zhang et al. was to achieve a durable phosphorescent coating by incorporating $SrAl_2O_4:Eu^{2+},Dy^{3+}$ phosphor into enamel coating. In order to attain the desired outcome, the researchers incorporated $SrAl_2O_4:Eu^{2+},Dy^{3+}$ phosphor as a 20% mill addition into a B_20_3-ZnO-PbO-$Si0_2$-based glass system, resulting in the production of a luminescent enamel coating. The enamel coating was applied onto a metal substrate and subsequently subjected to a firing process at a temperature of 800°C for a duration of 5 minutes. Following a methodical coating process, a smooth finish was achieved. The researchers noted that the material exhibited a robust and high-intensity photoluminescent property upon excitation by sunlight or synthetic lamps. Additionally, they noticed that the material emitted light for a duration of 12 hours even after the excitation source was discontinued [17].

Rossi et al. successfully synthesized a luminescent pigment through the incorporation of Eu_2O_3 and Dy_2O_3 into an amorphous matrix composed of Al_2O_3, SiO_2, MgO, SrO, and B_2O_3. The process of applying enamel coating to metal plates involves a three-coat application technique. The final enamel coat is formulated using the luminescent pigment

as a 50% mill additive. Consequently, an enamel coating that emits light is acquired. The present study investigates the performance of luminescent pigments in enamel coating, which contain varying amounts of Eu_2O_3 and Dy_2O_3. The use of a novel method resulted in a luminous enamel layer that showed dual emission peaks, namely blue and green. The green peak demonstrated a positive correlation with the concentration of dysprosium. The researchers noted that the exceptional resistance properties of conventional enamel systems remained unaffected by the existence of the luminescent enamel layer [18].

1.2 Objectives of Thesis

Glass-ceramic coatings are coverings that are put to steel and ensure both improved functional and aesthetic properties. In addition to improving the visual qualities of glass-ceramic coatings, the use of luminous materials that release light when triggered in glass-ceramic coatings is appropriate for use in numerous situations that require illumination. The objective of this research is to develop environmentally sustainable and energy-efficient glass-ceramic coatings with luminescent properties by incorporating $SrAl_2Si_2O_8:Pr^{3+}$, Dy^{3+} and $SrAl_2Si_2O_8:Er^{3+}$, Dy^{3+} into the coating system, while maintaining the superior technical characteristics of glass-ceramic coatings.

1.3 Hypothesis

The present study is specifically focused on the procedure of gaining luminescent properties to glass-ceramic coatings, an area that has been rarely explored in literature. The thermal resistance properties of $SrAl_2Si_2O_8:Pr^{3+}$, Dy^{3+} and $SrAl_2Si_2O_8:Er^{3+}$, Dy^{3+} provide maintain their characteristics during the vitrification process of coating at elevated temperatures. The inclusion of $SrAl_2Si_2O_8:Pr^{3+}$, Dy^{3+} and $SrAl_2Si_2O_8:Er^{3+}$, Dy^{3+} as milling additives in the glass-ceramic coating composition is hypothesized to the acquisition of luminescent characteristics to glass-ceramic coatings.

Moreover, it is anticipated that raising the concentration of $SrAl_2Si_2O_8:Pr^{3+}$, Dy^{3+} and $SrAl_2Si_2O_8:Er^{3+}$, Dy^{3+} in the coating system would lead to an amplified in emission intensity. Furthermore, it is expected that elevated concentrations would result in a rise in the surface roughness of the coating. Another forecast points that the particles of $SrAl_2Si_2O_8:Pr^{3+}$, Dy^{3+} and $SrAl_2Si_2O_8:Er^{3+}$, Dy^{3+} possess notable chemical stability, thereby augmenting the coating's stability against weak acids.

2
GLASS-CERAMIC

2.1 Definition

In the 1950s, glass ceramics were discovered and described by Dr. Stookey, a famous glass scientist. In accordance with his study, glass-ceramics were created using special glasses that included the nucleating chemicals required for the creation of their distinctive crystalline structure. The glass is melted, formed, and then crystallized under highly regulated conditions to produce this composition [19]. Although Stookey is credited with originating this definition, earlier experimenters had conducted thorough inquiries into the feasibility of producing a dense ceramic substance by means of glass objects' crystallization as early as the 1700s. The material in question piqued the interest of Stookey, who proceeded to conduct extensive research on it. As a result of his investigations, he was able to introduce it to the market as a novel type of material possessing highly sought-after characteristics.

Dr. Stookey was performing a silver precipitation experiment in the laboratory using lithium silicate glass, which is known for its superior chemical stability and is commonly used in the creation of permanent photographic images. For the precipitation study, Stookey discovered via the heat recorder that the furnace temperature unintentionally increased to 850 °C overnight after the glass samples were placed in the oven to maintain them at around 450 °C. Thinking that the glass had undergone a state of melting and the furnace had malfunctioned, Stookey made the observation that the sample had not undergone any melting and had retained its original state upon removal. During the process of removing the glass from the stove, an unintended incident occurred where it fell to the ground; however, it remained intact and did not shatter. On the contrary, it had felt like metal. Stookey inspects the glass subsequent to this peculiar circumstance. After careful consideration, he arrived at the conclusion that the ceramic object he had produced exhibited exceptional resilience [20].

Dr. Stookey's research was ongoing and recalled the examination of reports that suggest lithium aluminosilicate crystals possess notably low thermal expansion properties. Hummel (1951) identified the β-spodumene phase as possessing thermal expansion properties that are nearly zero [21]. It was noticed by Dr. Stookey that the nucleation of low thermal expansion phases, similar to lithium disilicate, would hold greater

significance if achieved. Dr. Stookey conducted research on various materials, including zinc sulfide and titania. However, he made a significant observation regarding the durability of titania-doped aluminosilicate glass-ceramics, which prompted him to pursue commercialization. This product has found applications in diverse fields, ranging from rocket nose cones to Corning Ware cookware [22].

The field of glass-ceramics has undergone notable advancements over the years, leading to their widespread utilization across various industries including ceramics, glass, metals, and nanomaterials. As various fields, including ceramics, glass, metals, and nanotechnology, progressed, there was a convergence of these disciplines, resulting in the amalgamation of glass-ceramic materials with glass-crystal composites. Deubener et. al. provided a contemporary definition of glass-ceramics as inorganic, non-metallic substances that undergo regulated crystallization of glasses through diverse processing techniques. These materials have both residual glass and at least one functional crystalline phase, with the crystalline phase volume percentage ranging from ppm to over 100% [21], [23].

Glass-ceramics are composed of polycrystalline substances that have undergone regulated thermal processing to supplant the nucleation and crystal growth mechanisms that take place in glasses that are suitable for crystallization. Nucleating agents, such as titanium dioxide (TiO_2), chromium (III) oxide (Cr_2O_3), zirconium dioxide (ZrO_2), phosphorus pentoxide (P_2O_5) oxide groups, and fluorides, are incorporated into the glass matrix to serve as nucleation centers within the matrix. The nuclei undergo growth and subsequently develop into crystals through controlled thermal conditions, ultimately yielding one or multiple crystalline phases. The crystals exhibit diverse morphologies as rods, sheets, and spheres, and typically possess dimensions below 1 μm. The mechanical properties of glass-ceramic structures, including toughness, impact resistance, and wear resistance, are widely acknowledged. Figure 2.1 depicts the mechanism involved in the formation of glass-ceramics [21], [24].

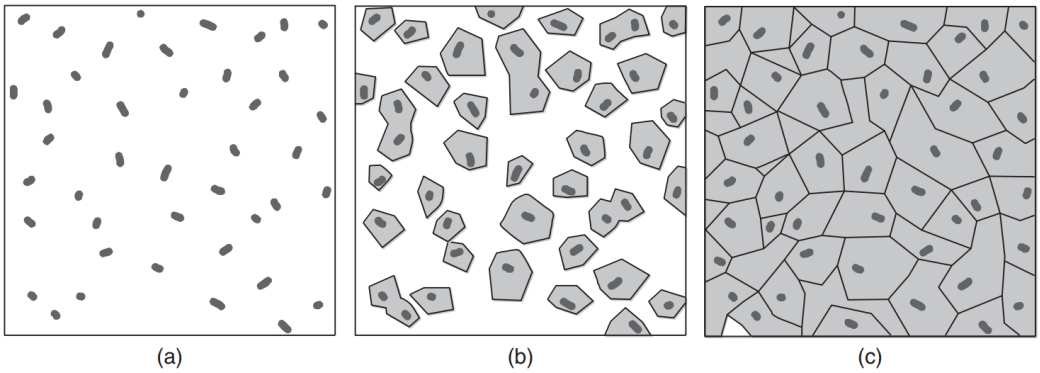


Figure 2.1 The process of converting the precursor glass into a glass-ceramic structure involves a series of steps, which (a) commence with the creation of nuclei, (b) succeeded by the development of crystals on the nuclei, and (c) culminate in the formation of the glass-ceramic [20].

The main step of glass-ceramic manufacturing, referred to as controlled crystallization or crystallization heat treatment, endeavors to transform amorphous glass into polycrystalline ceramic. The figure 2.2 illustrates the influence of temperature on the processes of nuclei formation and crystal growth. The capacity of glass to undergo crystallization can be identified as the underlying cause for its propensity to generate nuclei and foster crystal growth. When a sufficient number of nuclei, typically ranging from 10^{12} to 10^{15} nuclei within a volume of 1 cm^3, are attained through heterogeneous nucleation below the temperature at which melting is in equilibrium, a temperature range that is semi-stable is generated. This temperature range enables the growth of crystals. [25], [26]

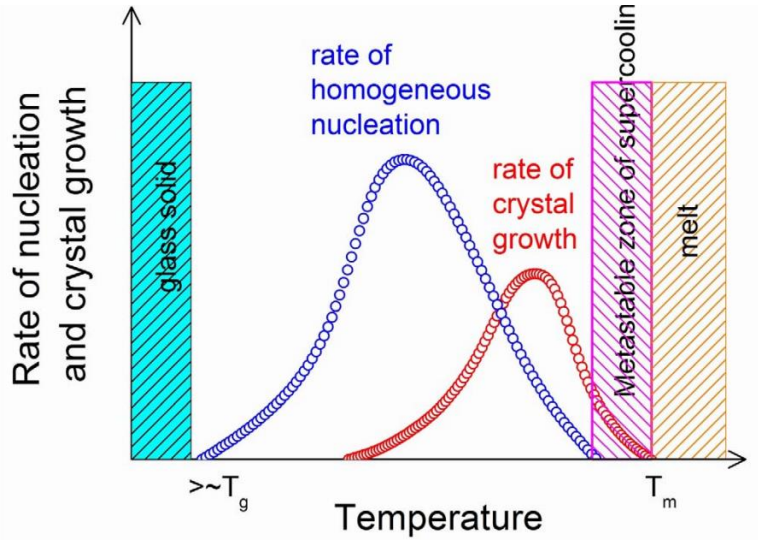


Figure 2.2 The association between crystal development and uniform nucleation during temperature change [27].

2.2 Manufacturing Methods of Precursor Glass

2.2.1 Pressing Method

This process involves the application of pressure between a mold and a plunger to shape the glass. Different types of pressing tools, including air vacuum and metal presses, can be employed [20].

2.2.2 Casting Method

In order to utilize this traditional method, it is imperative that the viscosity of the glass be kept to a minimum and that the temperature exceed the glass transition temperature. This methodology has the potential to be implemented within the field of dentistry [20].

2.2.3 Spinning (centrifugal casting) Method

The utilization of a rotating conical mould distinguishes this technique from conventional casting due to its indispensable nature. The prescribed range for viscosity in this particular procedure is 30 to 100 Pa.s. This is the process by which cathode ray tubes, the traditional television display technology, were manufactured [20].

2.2.4 Rolling Process

The process of rolling involves the pouring of molten glass onto a press table that has been cooled with water, followed by the subsequent rolling out of the glass. The recommended range for viscosity is 700 to 1000 Pa.s. This technique can be utilized for the production of flat glasses [20].

2.2.5 Float Process

The Pilkington process, commonly referred to as float glass, is the predominant methodology employed for the manufacture of planar glass. The process entails transferring the liquefied glass onto a molten tin surface, where it undergoes a flattening and solidification process while in motion. The tin bath is kept at low temperatures so that the glass can cool progressively and decrease interior stress. Subsequently, the flat glass is subjected to additional treatment on the annealing line, with the aim of enhancing its robustness and resilience.

2.2.6 Direct Forming or Reforming of Glass-Ceramics

On certain occasions, it is possible to manufacture glass-ceramics using ceramic phases. The remaining glass phases undergo liquefaction and attain malleability.

2.3 Characteristics of Glass-Ceramics

Glass-ceramic composites have controllable thermal expansion qualities, which result in desirable thermal performance. They are frequently employed in technical and industrial applications, especially in kitchen appliances. With the use of crystal and microstructure management, they may produce the necessary transparency, translucency, or opacity due to their glassy phase and pore-free structure. They also enable fluorescent applications and the creation of any desired hue, which is another optical characteristic. Glass-ceramic materials exhibit enhanced chemical stability both with the chemical resistance of the glass matrix and the presence of fiber-shaped crystals that augment their chemical resistance. They are also a great option for medical applications because of their excellent mechanical strength, bioactivity, and biocompatibility. Their toughness values now approach 3 $MPa.m^{1/2}$, and their bending strengths can reach up to 500 MPa. As a result of their excellent insulating capacity, low dielectric constant and loss, high resistance, and breakdown voltage, they are also perfect for a wide range of electrical and magnetic applications [20], [28]–[32].

2.4 Usage Area of Glass-Ceramics

The table 2.1 illustrates a number of industrial applications of glass-ceramics, which are highly favored for their excellent engineering properties.

Table 2.1 An overview of the main crystalline phases, their properties, and application areas of selected glass-ceramic systems [24], [33].

System	Main Crystalline Phase	Property	Application Area
$Li_2O.Al_2O_3.SiO_2$ (ZrO_2, TiO_2)	β-quartz β-spodumene β- eucryptite	Low thermal expansion High temperature resistance	Kitchenware Telescope Mirrors Oven Tops

Table 2.1 An overview of the main crystalline phases, their properties, and application areas of selected glass-ceramic systems (Continue) [24], [33].

$Li_2O.Al_2O_3.SiO_2$ (P_2O_5)	$Li_2O.Al_2O_3.SiO_2$	Dielectric properties Chemical resistance	Electronic Insulation Optical Coding Magnetic Recording Head Electric Sleeve
$MgO.Al_2O_3.SiO_2$ (P_2O_5, TiO_2)	Cordierite ($Mg_2Al_4Si_5O_{18}$)	Radar permeable Low thermal expansion High strength	Missile Cap Radar Dome
$PbO.ZnO.B_2O_3.SiO_2$ (F)	Rankinite ($3CaO.SiO_2$)	Heat & Vacuum insulation	Electrotechnology Microelectronic Circuits Capacitor
$BaO.Al_2O_3.SiO_2$ (TiO_2)	Celsian ($BaAl_2Si_2O_8$) Barium Titanate ($BaTiO_3$)	High strength Thermal shock resistance	Kitchenware Cookware
$SiO_2.Al_2O_3.MgO.K_2O$	Phlogopite [$KMg_3AlSi_3O_{10}(F,OH)_2$]	Turning ability Dielectric properties	Electrotechnology Insulator Hermetic Seals

Table 2.1 An overview of the main crystalline phases, their properties, and application areas of selected glass-ceramic systems (Continue) [24], [33].

$SiO_2.CaO.Na_2O$ (P_2O_5)	Apatite $Ca_5(PO_4)_3(F,Cl,OH)$	Biocompatibility Chemical resistance	Dentistry Prothesis
$SiO_2.Al_2O_3.MgO$ (TiO_2)	Mg-Al Titanate $MgxAl_2(1-x)Ti(1+x)O$	High hardness Resistance	Construction
$SiO_2.Al_2O_3.CaO$ (ZnO)	Wollastonite ($CaSiO_3$)	High hardness Resistance	Architectural Materials
$SiO_2.Al_2O_3.MgO.CaO$ (Sulphide, fluoride)	Wollastonite ($CaSiO_3$) Anorthite ($CaAl_2Si_2O_8$) Diopside ($MgCaSi_2O_6$) Pyroxene [(Na,Ca)(Mg,Fe,Al)(Al,Si)$_2O_6$]	High hardness Abrasion resistance Chemical resistance	Floor Tile Exterior Architectural Materials Pump Pipe

2.4.1 Technical Application

Radomes were the first glass-ceramics that were commercially available. The radar antenna is safeguarded by a structural casing that is resistant to weather conditions. The Radom glass-ceramic material exhibits a high degree of sensitivity to radio waves, resulting in significant attenuation of electromagnetic signals transmitted or received by the antenna, effectively reducing them to a minimum level. The application in question necessitates the presence of specific material properties, namely low dielectric loss, low

dielectric constant, low coefficient of thermal expansion, high strength, and high abrasion resistance [34].

Etched patterned materials are utilized in a variety of fields, including electronics, chemistry, acoustics, optics, mechanics, and biology, due to their high sensitivity tiny scale. These materials play a crucial role in advancing these disciplines. Glass-ceramics used for this purpose are primarily made using the SiO_2-Li_2O system. The fundamental composition of these type of glass is comprised of ions of Ce^{3+} and Ag^{+}. Upon exposure to ultraviolet radiation, the photoelectrons facilitate the oxidation of Ce^{3+} to Ce^{4+} and Ag^{+} to Ag^{0} within the compositions. The controlled crystallization process during heat treatment at 600 °C results in the formation of crystal phases [35].

The final product is generated through the process of utilizing diluted hydrofluoric acid to etch lithium metasilicate crystals. The improved glassy bodies were commercialized by Corning Glass and were marketed under the trademark Fotoform®. Conversely, the unetched configuration was marketed as Fotoceram® with certain alterations [36].

Fluoromica-based glass-ceramics are utilized in the production of machinable materials. MACOR®, a commercially available glass-ceramic material, is notable for its machinability and contains the fluorphlogopite phase ($KMg_3AlSi_3O_{10}F_2$). MACOR®, a versatile material, has been employed in diverse applications, including boundary retainers on spacecraft, electrical insulators, suction feed-throughs, microwave-type component screens, field-ion microscope parts, seismograph coils, and gamma-ray lens frames [37].

Glass-ceramics have been utilized in the production of magnetic memory disks, wherein canasite, lithium disilicate, spinel-enstatite, and spinel are among the frequently employed variants. The fracture toughness and Young's modulus of the material are fundamental parameters that significantly influence its overall performance. An example of this would be that crystals of Gahnite type $ZnAl_2O_4$ or spinel $MgAl_2O_4$, or their solid solution, are required to have a size that is smaller than 0.1μm. Enstatite must possess a fracture toughness exceeding $1MPa.m^{0.5}$. The glass-ceramic variant of spinel-enstatite, which is the predominant option for magnetic memories, exhibits a significantly elevated Young's modulus of 100-165 GPa in comparison to other glass-ceramic materials [20].

The SiO_2-Al_2O_3-Li_2O ternary system is employed in the fabrication of substrates that are utilized in Liquid Crystal Displays (LCDs), which are widely employed in personal

computing devices. In instances where the size of the crystallite is less than the wavelength of visible light, glass ceramics exhibit transparency, and their crystals demonstrate a refractive index that is comparable to that of the initial glass.

2.4.2 Optical Applications

In order to withstand temperature fluctuations, it is necessary for the materials used in telescope mirrors to possess a coefficient of thermal expansion that is as close to zero as possible. This requirement is met by using β-Quartz Solid Solution glass ceramics. Lithium metasilicate and lithium disilicate glass-ceramics are utilized in the production of the Integrated Lens Array, which has an approximate thickness of 20 micrometers [38].

The increasing popularity of luminescent glass-ceramics can be attributed to their high energy efficiency and minimal data loss. The utilization of various materials has been observed in a multitude of applications. For instance, Cr-doped mullite has been employed in solar concentrators, while Cr-doped gahnite spinel has been utilized in tunable lasers and optical memory media. Rare-earth-doped oxyfluorides have been found to be useful in amplification, upconversion, and quantum cutting. Additionally, chromium (Cr^{4+})-doped forsterite, β-willemite, and other orthosilicates have been employed for broad wavelength amplification. Ni^{2+} -doped gallate spinel has been utilized for amplification and broadband infrared sources. Finally, yttrium-(gadolinium)-aluminate garnet glass-ceramic phosphor has been used in applications for white LEDs [20].

Different types of crystal-based glass-ceramics have been employed in the manufacturing of optical components. These include fiber Bragg Grating Athermalization, laser-induced crystallization for optical gratings and waveguides, ferrules for optical connectors, and transparent ZnO glass-ceramics with regulated infrared absorbance and microwave susceptibility [39].

2.4.3 Medical and Dental Glass-Ceramics

This part pertains to two distinct domains of application, namely implantology, which concerns itself with medical prosthetics, and restorative dentistry, which is associated with dental prosthetics [40].

Implantology pertains to the development of medical prostheses that are surgically implanted into the human body, including dental implants, root fillers, and orthopedic and head and neck surgical devices. Restorative materials in dentistry are utilized to restore

natural teeth and comprise of dental inlays, crowns, bridges, and veneers. The materials used in implantology are required to possess biocompatibility and bioactivity, along with a hydroxycarbonate apatite layer that facilitates adhesion with both bones and soft tissues. In addition to enduring mechanical forces such as compression, tensile, shear, toughness, and Young's modulus, they must also exhibit resilience. Although aesthetic properties may not be of utmost importance, restorative dental materials are required to imitate the natural appearance of teeth and exhibit resistance towards abrasion, corrosion, and chemical reactions with food and beverages. The production of both types of materials necessitates precision, with micrometer-level dimensional accuracy and surface properties that are either smooth or rough, depending on the desired degree of roughness.

2.4.4 Electrical and Electronic Applications

Mica-based glass-ceramics are commonly employed as insulating materials due to their elevated dielectric constants. Glass-ceramic systems based on SiO_2–TiO_2–Nd_2O_5 and SiO_2–Al_2O_3–PbO are integrated with sintered ceramics to produce a composite material with a high dielectric constant. The process involves combining inorganic materials with a binder resin, a solvent, and a plasticizer, such as butylmethacrylate, toluene, and dibutylphthalate, respectively. The resulting mixture is then applied to a flat surface using the Doctor Blade Technique, with a thickness that typically ranges from 0.1 to 0.3 mm. Upon subjecting the organics to combustion at a temperature of 400°C followed by sintering of the resultant material at 900°C, a mechanically robust and compact material is produced. The organic materials are blended with the circuit patterns and subsequently deposited onto the surface through a printing process [41].

Glass-ceramic (GC) materials are utilized in electronic packaging applications as well. Advanced ceramics such as ZrO_2 are combined with SiO_2−Al_2O_3−MgO and SiO_2−Al_2O_3−ZnO systems to produce composite materials. The employment of this packaging system has been observed in the context of multilayer chip carriers within IBM's specialized computing systems.

Glass-ceramics with dielectric properties are designed and optimized for use in electronic devices operating in the GHz frequency range. Dielectric oxide ceramics have brought about a significant transformation in the field of microwave wireless communication. These ceramics have enabled the development of resonator and antenna components that are utilized in diverse applications such as GPS systems and mobile phones.

2.4.5 Architectural Applications

The NeopariésTM trademark is utilized by Nippon Electric Glass to denote their foremost glass-ceramic material for construction purposes [42]. The process of producing glass-ceramic entails the utilization of granular glass particles as a fundamental material. The granular glass particles are subsequently shaped into planar or curved panels through employment of a completely automated tunnel furnace capable of achieving temperatures as high as 1100°C. The process of sintering is employed to crystallize wollastonite at temperatures above 950°C, during the heat treatment of granular glass at 850°C. The salient features of these materials encompass their ability to withstand weathering, exhibit nil water absorption, possess lower weight compared to natural stone construction materials, and display exceptional hardness. Furthermore, this classification encompasses windows that possess the ability to withstand fire.

2.4.6 Glass-Ceramics for Energy Applications

Glass-ceramics are essential in improving energy production and management efficacy in diverse applications. The usage of these components is primarily observed in three domains that are associated with the production of energy, specifically, (i) the enhancement of solar energy efficacy, (ii) the constituents of batteries, and (iii) the solid oxide fuel cells [43]. Glass-ceramics possess the potential to serve as substitutes for the cathode, anode, and electrolyte, which are the three primary constituents of batteries.

3
GLASS-CERAMIC COATING

Glass-ceramic coatings, which are additionally known as enamel, exhibit considerable potential as a technology for safeguarding metal substrates and prolonging the longevity of metallic goods [44], [45]. The composition of the glass-ceramic coating involves the incorporation of frits, along with mill additives and flotation compounds, opacifiers, and colorants [46]–[48].

The fundamental components of the structure of the glass-ceramic coating comprise of frit that possesses an amorphous structure. These frits are essentially granules or flakes of glass that are obtained by melting various inorganic oxides at temperatures ranging from 1000-1500 °C, followed by rapid cooling. In order to achieve a consistent particle size, frit is ground into a fine powder using ball mills [49], [50]. In order to generate a glass-ceramic coating on a metallic substrate, a suspension is produced through the mixing of water with frit powder and milling additives. The application of suspension onto the substrate can be achieved through a range of wet techniques, including flow coating, spraying, dipping, and electrophoretic deposition. Powdered frits can be employed through dry techniques like thermal spray coating and electrostatic powder spraying. Following the application of the coating, a crystallization process takes place to generate a glass-ceramic coating on the metallic substrate [47], [50], [51]. The process of devitrification or crystallization takes place subsequent to the application of frit powder onto the substrate. The procedure may vary contingent upon the composition of the coating and the nature of the metallic substrate employed. In the case of applying glass-ceramic coatings onto steel substrates, it is customary to subject them to temperatures ranging from 780 °C to 850 °C. In the event that the coatings are administered onto substrates composed of aluminium, it is possible to subject them to elevated temperatures ranging from 500 °C to 570 °C [47], [51].

3.1. Definition of Glass-Ceramic Coating on Metal Substrates (i.e. Enamel)

The etymology of the term "enamel" can be traced back to the Old French word "esmail" and the German word "smelzan" that originated from it [52]. The contemporary

nomenclature designates enamel as "smalto" in Italian and "email" in both French and German [53]. Enamel is a glass-ceramic coating that is classified as an inorganic material. Its chemical composition contains silicates, which contribute to its high heat capacity. The enamel is recognized for its chemical and abrasion-resistant properties. Enamel is produced by pulverizing frits, which are the fundamental components of enamels, into a fine powder and subsequently administering it onto metallic substrates such as steel, cast iron, copper, or aluminum. The process is followed by heating at temperatures that vary between 500 to 870 °C. Various application techniques are at disposal, such as electrostatic spraying, wet spraying, electrophoretic deposition, and more recently developed thermal spray methods. Enamel coatings possess remarkable engineering characteristics, including elevated-temperature endurance, chemical durability, and mechanical robustness, in addition to aesthetic qualities, rendering it a favored option for a diverse array of commodities, ranging from heating appliances, fireplaces, and stoves, to timepiece dials, culinary utensils, and hot water dispensers [54]. Enamel coatings have emerged as a crucial coating for cookware due to their exceptional technical properties, aesthetically pleasing appearance, and diverse color palette [55]–[57].

Numerous sources and organizations describe enamel differently; nonetheless, the basic explanation is typically similar. According to ISO (International Standards Organization)'s 25.220.50 coded title, the enamel is a "substantially vitreous, or glassy, inorganic coating bonded to metal by fusion at a temperature above 500 °C [58]." However, the VEA (Vitreous Enamel Association) defines enamel as a "thin layer of glass fused onto the surface of a metal at high temperatures [52]," but the PEI defines it as a "substantially vitreous or glassy inorganic coating fused to metal at temperatures surpassing 800°F." The IEI defines enamel as a natural substance formed by heat that is corrosion-resistant, as pure as glass, available in a wide spectrum of colors that are unaltered by time and climatic conditions, and is always recyclable. A coating that gives a worldwide, fully adaptable solution to the requirements of all types of industrial industries [59]".

3.2. Chemical Design of Glass-Ceramic Coating

Glass-ceramic coatings are composed of components known as "frit," which have an amorphous structure. These are semicrystalline vitreous coating materials created by vitrifying and recrystallizing oxides such as SiO_2, B_2O_3, Al_2O_3, Na_2O, NiO, CuO, P_2O_5, and Fe_2O_3 according to the Seger recipe [46]. Its production is investigated under four

major headings: i) producing the frit by the molten material at high temperature via quenching, ii) milling together with frit and other additives, iii) applying the ground mixture to the metal substrate, and iv) vitrification and crystallization at relatively high temperatures (720-850°C) [20]. Because of its crystalline and amorphous structure, the final product produced after the application procedures is resistant to mechanical, chemical, and thermal damage, as well as an attractive coating material [28].

The oxides in Table 3.1 are classified based on their functions in the glass-ceramic system. Silica has the ability to produce glass network at adequately high temperatures (over 1700 °C) in glass-ceramic systems without the presence of any additional components. SiO_2 is the commonly employed glass-ceramic component in glass-ceramic mixtures. Glass-ceramic coatings, for example, are a silica tetrahedra structure with additional materials added as modifiers [60].

Table 3.1 The functions of the oxides present in the glass-ceramic system, as well as the sources of these oxides in the raw materials utilized in the system [55].

Component	Minerals	Functions
SiO_2	Quartz Feldspar	Refractory component, glass forming oxide, raises the glass-transition temperature of vitreous system, adds chemical resistance and increases viscosity.
B_2O_3	Borates	Flux that produces the vitreous matrix, reduces viscosity and increases surface hardness.
Na_2O K_2O Li_2O	Albite Feldspar Microcline Spodumene Petalite Lepidolite	Alkaline components lower the temperature of which glass softening point, reduce its elasticity and increase its brilliance.

Table 3.1 The functions of the oxides present in the glass-ceramic system, as well as the sources of these oxides in the raw materials utilized in the system (Continue) [55].

Al_2O_3	Feldspar Corundum	Increases viscosity and chemical, mechanical and thermal resistance, reduces the expansion coefficient and favours an opaque finish.
ZrO_2	Zirconia	Improves resistance to acids, to knocks and to shocks, acts as an opacifier.
ZnO	Zincite Blende Wurtzite	Excellent flux, lowers the expansion coefficient and improves brilliance and surface quality.
CoO	Cobaltite	A very strong adherence agent, it produces a structure with lots of small, well distributed bubbles.
NiO	Niccolite	A second adherence agent, it produces a structure with a small number of large bubbles.
CuO	Copper Oxide	When combined with primary bonds, it triggers the adherence reaction at lower temperatures.
MnO_2	Manganese Dioxide	Produces brown-coloured frits, intensifies dark colours and acts as an oxidant and as a weak bonding agent.
Sb_2O_3	Antimonite	Produces a high degree of opacity and improves resistance to acids.
TiO_2	Rutile Anatase	Opacifiers, it increases whiteness, brilliance and resistance to acids and heat.

Table 3.1 The functions of the oxides present in the glass-ceramic system, as well as the sources of these oxides in the raw materials utilized in the system (Continue) [55].

BaO CaO MgO	Baryte Witherite Calcite Dolomite Limestone Periclase	Alkaline-earthy components that integrate anti- acid glass-ceramics coating, increasing their resistance, their CaO smelting facility and their viscosity.
P_2O_5	Apatite	Alters the opacity of the finish, improves colour stability and reduces chemical resistance.
CaF_2	Fluorite	Softens glass and influences the opacity

Table 3.1 The categorization of oxides based on their roles in the glass structure

Glass Former	Glass Modifier	Glass Modifier	Adhesion Agents	Nucleating Agents
SiO_2	MgO	Li_2O	MnO_2	TiO_2
GeO_2	CaO	Na_2O	CoO	ZrO_2
B_2O_3	SrO	K_2O	NiO	Fe_2O_3
P_2O_5	BaO			Cr_2O_3
Sb_2O_5	ZnO			P_2O_5

The elements in the chemical composition of glass-ceramic coatings are classified in table 3.2 into five groups based on their function: fluxes, refractories, adhesion agents, opacifiers, and colorants.

3.2.1 Fluxes

The main goal of fluxing agents is to decrease the melting point of SiO_2, which enhances the uniformity of glass-ceramic coatings. Uniformity improves adherence of the glass-ceramic coating to the substrate, resulting in a higher surface finish. Borax ($Na_2[B_4O_5(OH)_4]\cdot 8H_2O$), soda ash ($Na_2CO_3$), soda nitrate ($NaNO_3$), fluorspar ($CaF_2$), cryolite ($Na_3AlF_6$), barium carbonate ($BaCO_3$), magnesium carbonate ($MgCO_3$), litharge (lead (II) oxide), red lead (lead (II, IV) oxide), and zinc oxide (ZnO) are some of the widely used raw materials in flux group [46].

3.2.2 Refractories

Raw materials in this category contribute to the glass network structure and improve the melt's acidic characteristic. Quartz, feldspar, and clay are the most basic raw materials for refractory oxides. They form a quartz glass network and provides mechanical and chemical qualities to the finished product [46].

3.2.3 Adhesion agent

As glass-ceramic coatings are deposited to metal surfaces, it is crucial to provide adhesion mechanisms between the metal and coating. To do this, oxides such as cobalt oxide, nickel oxide, and copper oxide are added to the molten glass. CoO, the most essential adhesion agent, not only promotes adherence, but also imparts a blue hue [46].

3.2.4 Opacifiers

The principal function of the oxides in this category is to provide opacity to the glass-ceramic coating. Antimony oxide, sodium antimonate ($NaSbO_3$), titanium dioxide (TiO_2), zirconium silicate ($ZrSiO_4$), and zirconium oxide make up the majority of this category of oxides. In this category, titanium oxide is the most powerful opacifying oxide. These oxides share refractory characteristics. There are additional supplemental opacifiers like cryolite and fluorspar that boost the melt's fluidity [46], [61].

3.2.5 Colour Agents

Glass-ceramic coatings are distinctive not only for their superior aesthetic qualities. Coatings should thus include a variety of colours and hues. The most often utilized oxides

in this context are cobalt oxide (CoO), copper oxide (Cr_2O_3), iron oxide (Fe_2O_3), manganese oxide (MnO), and nickel oxide (NiO). These oxides may be used as colorant on their own, or they can be tinted by adding pigment to the frits that are created [46].

3.3. Adhesion Mechanism

3.3.1 Diffusion Theory

The dendritic theory also referred to as the diffusion theory, posits that adhesion is facilitated by dendrites, which possess a tooth-like shape and serve a crucial function at the interface. The phenomenon of iron diffusion from the metallic substrate to the glass-ceramic material, and silicon diffusion from the glass-ceramic coating to the substrate material, occurs at the interfaces between the glass-ceramic coating and the metallic substrate. As a result, dendritic structures are formed. The adhesion mechanism between the metal and the glass-ceramic coating is established via the dendritic structures that are generated at the interface of the coating and the metal substrate during the period of cooling subsequent to the firing of the glass-ceramic coating. Consequently, it is postulated that the adhesion mechanism involves with the diffusion process [62].

3.3.2 Chemical Theory

According to this hypothesis, a driving force for the metal to oxidize and build the iron oxide (FeO) molecule is generated during the sintering process when the glass dissolves the already-present oxide layer and comes into contact with the metal [63].

During the firing process of the glass-ceramic coating, reactions that take place in the substrate material [64];

$$Fe_3O_4 \rightarrow Fe^{2+} + 2Fe^{3+} + 4O_2 \quad (1)$$

$$2Fe^{3+} + Fe \rightarrow 3Fe^{2+} \quad (2)$$

Then, the cobalt oxide and nickel oxide in the glass-ceramic coating are transformed into metallic cobalt and iron by the presence of metallic iron in the substrate metal substrate.

$$Fe + CoO \rightarrow FeO + Co \quad (3)$$

$$Fe + NiO \rightarrow FeO + Ni \quad (4)$$

The Ellingham diagram illustrates that the oxygen affinity of a molecule grows as it moves towards the bottom of the diagram. According to the Ellingham diagram shown in Figure 3.1, iron has a higher affinity for oxygen than nickel and cobalt at the temperature at which glass-ceramic is fired. As a direct consequence of this, the majority of adhesive properties come from nickel and cobalt [47], [63].

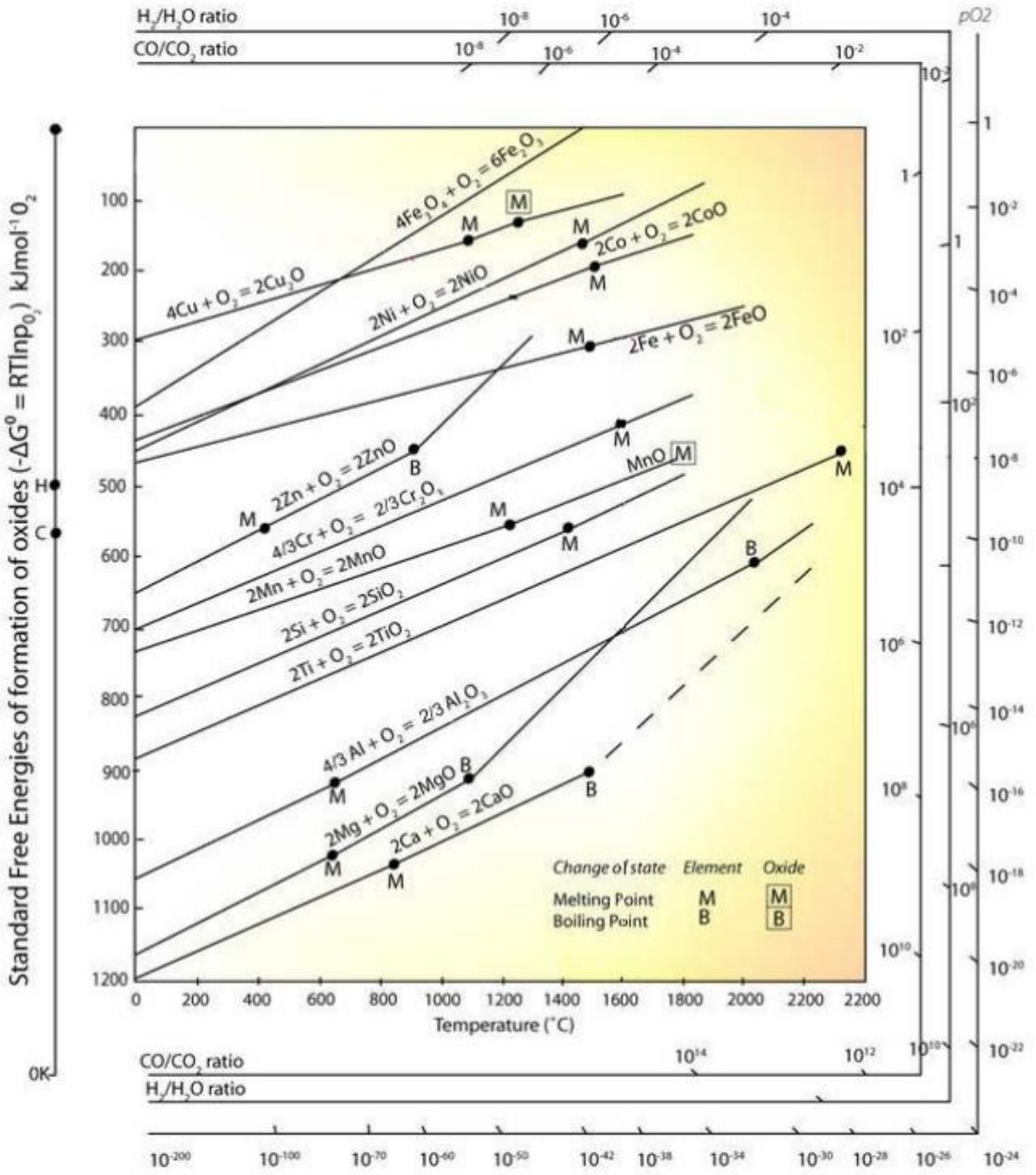


Figure 3.1 The illustration of Ellingham's diagram [47]

3.3.3 Mechanical Theory

The mechanical bond hypothesis pertains to the substrate surface area that contacts the glass-ceramic coating. Before the coating process, the surface of the base material is

chemically (using hydrochloric acid HCl and sulfuric acid H_2SO_4) or physically roughened to improve the contact area between the glass-ceramic coating and the base material. The ground material oxidizes and diffuses into the glass-ceramic system when the coating reaches the firing temperature, generating protrusions known as dendritic structures. It is known that the dendritic structure created at the interface between the base material and glass-ceramic coating also favorably impacts the adhesion mechanism owing to the increase in the adhesion area [60], [65].

3.4.Properties of Glass-Ceramic Coating

3.4.1 Thermal Properties of Glass-Ceramic Coatings

3.4.1.1 Thermal Expansion

The phenomenon of thermal expansion describes when the volume or length of a substance grows as its temperature rises. In other words, it is possible to determine the changes in volume or length occurring in a material by observing them at 1 unit temperature change. The coefficient of thermal expansion is calculated by multiplying the unit shape change by the temperature difference. The linear thermal expansion coefficient describes the change in material length per each 1 °C increase in temperature. The linear thermal expansion coefficient (α) is computed using the following equation:

$$\alpha = \frac{1}{l} x \frac{\Delta l}{\Delta t} \quad (5)$$

where l is the length of the material, Δl is the temperature-induced elongation, and Δt is the temperature difference.

The volumetric thermal expansion coefficient describes how the volume of a material increases for each degree Celsius of temperature increase. The relationship between the volumetric thermal expansion coefficient (β) and the linear thermal expansion coefficient (α) for materials that are isotropic, such as amorphous structures and glasses, is as follows:

$$\beta = 3 \times \alpha \quad (6)$$

The interaction between glass-ceramic coatings and metal depends on their thermal expansion coefficient. For glass-ceramic coatings technology to operate effectively, the thermal expansion coefficients of the coating and substrate metal must be near. If the thermal expansion coefficient of the glass-ceramic coating is less than that of metal, the

coating will contract rapidly upon cooling after firing. When the glass-ceramic coating-metal adhesion is very strong, as defined by the adhesion properties of glass-ceramic coatings, the metal surface stands out against coating shrinkage. In this instance, when the tensile strength of the glass-ceramic coatings is exceeded, stress-generating fissures remain in the structure. When the metal's coefficient of thermal expansion is less than the glass-ceramic coating's compressive strength, chipping flaws arise. In applications involving glass-ceramic coatings, the expansion coefficient should be smaller than that of metal since compressive strength is 15 to 20 times more harmful than tensile strength [66], [67]. The thermal expansion coefficients of various metals and glass-ceramic coatings are listed in Table 3.3.

Table 3.3 The coefficients of cubical thermal expansion that several glass-ceramic coatings and some metals exhibit [67].

Material	Cubical Thermal Expansion Coefficient ($3.\alpha \times 10^{-7}$)	Temperature Range (°C)
Iron	426	0 – 500
Low Carbon Steel	465	27 – 760
Cast Iron	378 – 390	20 – 500
Ground Coat for Steel	240 – 300	0 – 100
Cover Coat for Steel	280 – 360	0 – 100
Ground Coat for Cast Iron	250 - 300	0 – 100

3.4.1.2 Thermal Shock

The thermal shock protection of glass-ceramic coatings explains how the coatings respond to sudden temperature fluctuations. Winkelmann and Schott were computed matematically as a following:

$$K = \frac{P}{\alpha . E}\sqrt{\frac{\lambda}{c} . d} \qquad (7)$$

where P represents the tensile strength, α represents the coefficient of linear thermal expansion, E symbolizes the elasticity modulus, λ represents the thermal conductivity coefficient, c represents specific heat, and d represents the density.

Thermal shock protection depends not only on specific thermal qualities but also on a large number of other factors, with internal stresses having the most significant influence. When the thermal expansion coefficient of the glass-ceramic system is lower than that of the metal substrate, the system induces compressive stresses during rapid heating and tensile strains during rapid cooling. Although compressive pressures are lower than tensile pressures, glass-ceramic coatings exhibit greater resistance to thermal shock during rapid heating. The size of the stresses is particularly important since convex areas have greater tension than concave areas, making them less resistant to thermal shock. The thickness of the glass-ceramic coating and substrate metal also play a critical role in terms of thermal shock protection [67].

As previously mentioned, fast cooling reduces the thermal shock resilience of glass-ceramic coatings. However, the cooling environment is equally important. The thermal shock effect of cold air is less than that of cold water. To evaluate the resilience to thermal shock of glass-ceramic coatings, cold water experiments are conducted [68].

3.4.1.3 Thermal Conductivity

In commercial and academic contexts, the heat conductivity of glass-ceramic coatings is an essential characteristic. In culinary equipment, heat transmission via glass-ceramic coating is a crucial need. As a reflector or emitter, it is a desirable feature in military, construction, refrigerator, and oven applications. The inclusion of oxides version of elements with a high thermal conductivity (metallic powders) may increase the thermal conductivity of glass-ceramics.

The following formula is used to compute thermal conductivity, which is a value of the thermal conductivity coefficient:

$$\lambda = p_1 . \lambda_1 + p_2 . \lambda_2 + p_3 . \lambda_3 \ \ (watts/m.deg) \qquad (8)$$

where λ represents thermal conductivity, p symbolized percentage of oxide and λ_i symbolized factor for the oxide.

3.4.1.4 Fusibility and Fluidity

Important qualities associated with the molten state include fusibility and fluidity, which come to the fore while melting the glass-ceramic raw material and firing it following application. It is governed by the chemical composition, although its computation has rarely advanced above the experimental stage. The majority of calculation attempts were valid for a certain composition range. Thus, the following tests have become essential for each glass-ceramic coating composition: cone fusion test, fusion flow test, fusion block test, bead test, and interferometer test. The cone fusion test measures deformation intervals, fusion flow test measures temperature-related hardness and softness, fusion block test measures glass-ceramic coating composition fusion temperature, bead test measures fusibility, fluidity, and surface tension, and interferometer test measures expansion coefficient [66].

3.4.1.5 Viscosity

The viscosity of glass-ceramic coatings, similar to other vitreous materials, is a significant parameter which is strongly influenced by temperature, hence a minor change in temperature may result in a big change in viscosity. As illustrated in Figure 3.2, the glass transition temperature is the point in a material's evolution from a ductile to a brittle state. The material demonstrates a viscosity of 10^{12} N.sec/m^2 at this particular temperature. Furthermore, Ts denotes the temperature at which a substance transitions melting state. Moreover, the viscosity is 10 N.sec./m^2.

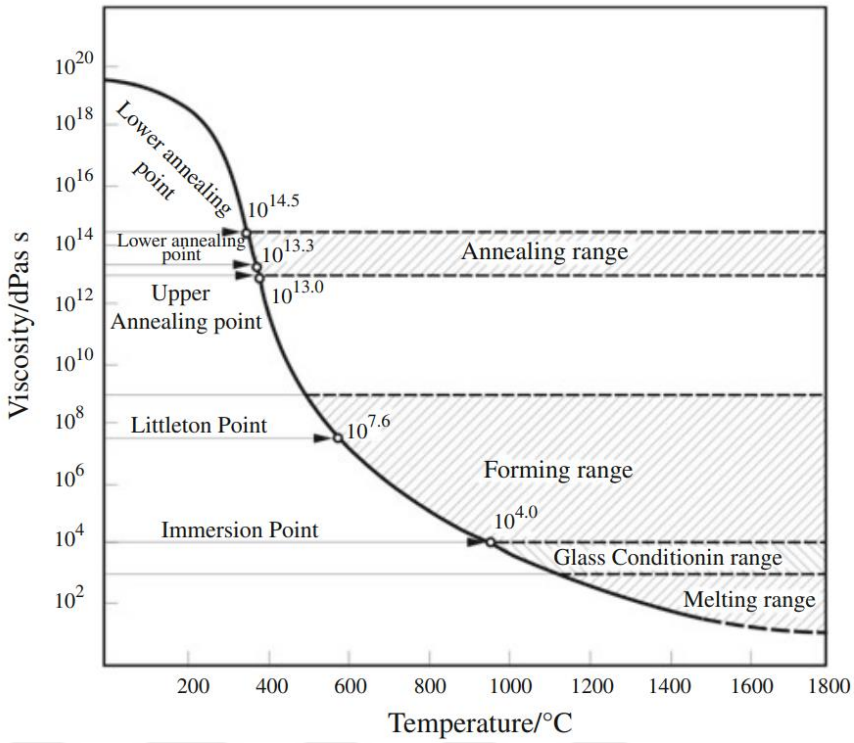


Figure 3.2 The association between temperature change and viscosity in a glass structure [50].

Using the chemical composition, viscosity may be calculated. With glass-ceramic system, the TG value is typically about 500 °C, while the TS temperature is about 1400 °C. Furthermore, when the viscosity increases, the operating temperature of glass-ceramic coatings increases, the gas emission lowers, and the surface smoothness increases. Conversely, low viscosities result in glass-ceramic coating flaws and unequal coating thickness. Throughout the firing process, the viscosity of glass-ceramic coatings ranges between 10^2 and 10^3 N.sec/m^2 [66].

In wet operations of the glass-ceramic coating method, the viscosity parameters of the created glass-ceramic coating slurry may be readily modified using substances such as boric acid, clay, and sodium nitrite.

3.4.2 Physical and Mechanical Properties

3.4.2.1 Density

In wet operations, the density (specific gravity) attribute is often utilized to regulate the particule's mobility. Glass-ceramic coatings ought be diluted according to density, which may be determined using a pycnometer. The formula for estimating the density of glass-ceramic coatings is:

$$S = (w - p)/[(w - p) - (w_2 - w_1)] \quad (9)$$

where S represents the specific gravity of the glass-ceramic coating, w represents the weight of the pycnometer and sample, w_1 represents the weight of the tapered pycnometer filled with water, w_2 represents the weight of the tapered pycnometer, sample, and water, and p represents the weight of the tapered pycnometer [67].

3.4.2.2 Specific Heat

The term "specific heat" refers to the amount of heat needed to increase a material's temperature by 1°C while maintaining a 1 kg mass at constant pressure and volume. The following equation may be used to determine the glass-ceramic coating's specific heat:

$$S = p_1.s_1 + p_2.s_2 + p_3.s_3 + \cdots \quad (10)$$

where S represents the specific heat of the glass-ceramic coating, p represents the proportion of the oxide, and s represents the oxide factor [67].

3.4.2.3 Hardness

In accordance with the Mohs scale, the hardness of glass-ceramic coatings ranges from 5 to 6 on a scale based on chemical structure. Rockwell, Brinell, and Knopp are not typically used for measuring the hardness of glass-ceramic coatings because they yield inadequate data. Mohs scale is also used to determine the scratch resistance of glass-ceramic coating [67].

3.4.2.4 Elasticity

In spite of the fact that elasticity is an essential material feature, it is not often exploited in the area of glass-ceramic coatings. Both mechanical and acoustic approaches may be employed to analyze it. The mechanical technique has the following mathematical formula:

$$E = 4PL^3/bd^3\Delta \quad (11)$$

where P denotes the load, L denotes the material's length, b denotes its breadth, d denotes its thickness, and Δ denotes its deflection [67].

3.4.2.5 Compressive Strength

The compressive strength of glass-ceramic coatings is an often-overlooked attribute with the potential to affect other properties. It has a value between 77 and 81 kg/mm^2 for traditional SiO_2-B_2O_3-Na_2O glass-ceramic coatings and may be computed using Winkelmann and Schott's methods [67].

3.4.2.6 Tensile Strength

While the tensile strength of glass-ceramic coatings is an essential feature, analyzing it may be tricky. Owing to their brittle fracture characteristics, materials coated with glass-ceramic are good for cracking. As a consequence, several examination strategies have been developed. It has an effect on the thermal characteristics of glass-ceramic coatings, namely their thermal expansion, while not being a desirable or directly analyzed attribute [67].

3.4.3 Chemical Properties

Glass-ceramic coatings are subjected to acid corrosion in several applications, notably in kitchenware. SiO_2 is one of the most influential oxides affecting acid resilience, as the acid resistance of the glass-ceramic coating is influenced by the progression of the formation of $[SiO_4]$ in the coatings. To withstand the corrosive impact of acid, $[SiO_4]$ tetrahedrons are employed to cover the vicinity of $[AlO_4]$-R^+ and $[BO_4$-$R^+]$ in the structure. Hence, as the SiO_2 concentration of glass-ceramic coatings increases, so does their acid resistance. In contrast, when the size of the R_2O group in the structure increases, the Si-R-O structure generated by ions such as Li^+, Na^+, and K^+ interrupts the continuity of the $[SiO_4]$ tetrahedrons, hence decreasing acid resistance [69], [70].

The hydrogen ions in the extract interact with the structure of the glass-ceramic coatings and lead the alkaline ions in the coatings to dissociate into ions, resulting in the ion transfer leaching of the coatings. This is a pH-dependent process that frequently takes place at pH 9 [70], [71].

The interaction between hydrogen ions and a silica matrix creates alkaline ions when two non-bridging oxygen atoms are present. This indicates that alkali metal ions linked by unbridged oxygen may readily replace hydrogen, leading to the creation of a wet surface layer.

The silicate network typically starts to dissolve at pH > 8 and accelerates as the pH increases. At such pH levels, the OHs react with the hydrated layer or glass structure. Si(OH) compounds are produced when hydroxyl groups react further with the initial product. The secondary product, SiO-, interacts with water and acts in the reaction SiO- + H_2O → Si-OH + OH. Glass-ceramic coatings deteriorate as a consequence of repeated interactions with hydroxyl groups [70], [71].

Glass-ceramic coatings are water-resistant and preserve their structural stability at room temperature. Additionally, hot water has no effect on the structure of the coating. In contrast, the coating structure deteriorates with extended exposure to extreme conditions such as pressure and heat at the site of usage [70], [71]. In tests conducted according to DIN EN ISO 4753-3, glass-ceramic coatings should not exceed 8 mg/m^2 after 21 + 21 days (a sum of 6 weeks) [72]. Water resistance is critical in applications involving thermosiphons, valves, and boilers.

3.5. Application Areas of Glass-Ceramic Coatings

Glass-ceramic coatings are used as a protective coating in a wide range of fields, including;

- water heaters,
- thermosiphons,
- boilers,
- fireplaces,
- pipelines,
- silos, and
- hot water services,

because they have advanced engineering properties, such as resisting high temperatures and chemical corrosion, in addition to mechanical properties and aesthetic appearance. In addition to these attributes, glass-ceramic coatings are essential for kitchenware and cookware due to their superior physical specifications, aesthetic qualities, and vast color palette [55], [57].

3.6. Coating Methods for Glass-Ceramic Coatings

Both wet and dry coating methods are available for glass-ceramics. The coating process is selected after taking into account the application area, cost, metal substrate qualities, and glass-ceramic features.

3.6.1 Coating Process By Wet Method

Mill additives are often necessary for applications of glass-ceramic coatings. The slurry of the glass-ceramic coating, which is used in the wet method, is produced by incorporating mill additions and water into the frit composition that has been added to the mill. The frit ratio is regarded as 100%, and subsequent additions of mill and water are made in accordance with this proportion. It is expected that the sum of the raw materials introduced into the mill will not reach 100%. The quality of water utilized for acquiring the glass-ceramic coating slurry is of significant importance in wet applications. The presence of different types of salts, namely sodium, calcium, and magnesium sulfates, that were dissolved in water, adversely impacts the quality of coatings. Whilst distilled water is deemed suitable for use in optimal circumstances, it is not a viable option for industrial purposes. The addition of mill additives, such as clay, serves the purpose of maintaining the suspension of frit particles within the coating slurry. Although the characteristics of clay materials exhibit regional variability, typically constituting a proportion of the recipe ranging from 4% to 8%. The function of the electrolyte materials in the recipe is to maintain a specific arrangement of the frit particles that are suspended by the buoyant constituents. Electrolytes, namely sodium nitrite ($NaNO_2$), boric acid (H_3BO_3), potassium carbonate (K_2CO_3), and sodium aluminate ($NaAlO_2$), are employed in regulating the fluidity, consistency, flow rate, and infiltration balance of the slurry utilized for glass-ceramic coating. The utilization of quartz within the mill results in an augmentation of both resistant to acids and firing temperature [73].

3.6.1.1 Spraying Method

Compressing air and then spraying either glass-ceramic slurry or glass-ceramic powder onto metal substrate is one method for applying glass-ceramic coating. The two most prevalent ways for spraying glass-ceramic coating are manual spraying and automated spraying by machine. Machine spraying enables for mass manufacturing [74].

Glass-ceramic spray coating may be applied to both indentation and flat surfaces. In the manufacturing organization, it is used to cover stove side panels, kitchenware equipment

such as pots and pans, kitchen trays, chassis, doors, body, grill, stove plate, and burner. Glass-ceramic slurry for spray glass-ceramic coating in the wet process should be ideal, that is, glass-ceramic suspension should be big enough to adhere to the metal surface yet tiny enough to flow through the spray nozzles, so as to provide a superior atomization effect [75].

A notable benefit of the spray approach is that the glass-ceramic powders that are spilled over may be reused without clinging to the component. Hence, environmental dust, oil, and grime should be kept out of the cabin where the application is made [76].

3.6.1.2 Dipping Method

Dipping is the most fundamental and easiest procedure for coating of glass-ceramics. It is suitable for one-color items. This is a standard procedure for coating both the inside and exterior surfaces of pots and pans. Tiny, spherical, and simple-shaped items are immersed in a glass-ceramic coating slurry and then extracted after ensuring that all surfaces are coated. Hence, the coating is performed by dipping technique. Using procedures such as turn, hook, or swing, the excess material remaining on the components extracted from the slurry is removed. To obtain a homogeneous glass-ceramic coating, the density of the batch in the immersion tank, the fineness of grinding, and the set value must be monitored and managed [77].

3.6.1.3 Electrophoresis Method

Using the electrophoresis technique, thin, even coatings can be put on parts with complicated shapes. With the help of an electric current in the glass-ceramic suspension, the frit particles stick to the surface to be coated, which is connected to the anode. In the electrophoresis method, the density of the glass-ceramic slurry, the size of the particles, and the amount of power used are the most important things that affect the quality of the coating [78].

3.6.1.4 Flow Coating

Flow coating is in the modern manufacturing process updated version of the dipping technique. In this process, the piece with the glass-ceramic coating is not put into the batch. The glass-ceramic coating works by putting into the piece at a specific point using a pump. This makes the coating stick to the surfaces. This method is cheaper and more effective than immersion method [77].

3.6.1.5 Thermal Spray Method

Powder frits or glass-ceramic powder are fed into the plasma jet, where they melt, and then they are spreyed on the surface of metal substance to be coated. Through the spray gun, the melted frit is sprayed on the surface at about 100–200 m/sec. The distance between the surface and the gun is around 100 to 150 mm. Frits come out of the gun at a temperature of about 1500 °C. When they adhere to the surface, their temperature drops to 270 °C because of the sudden direct cooling. The temperature then drops to 90 °C and then to 40 °C. It's an application that needs to be done carefully, so when it's done right, it gives the best results compared to other ways [79].

3.6.2 Electrostatic Powder Coating Method

With this technique, glass-ceramic coating material in dry powder form is electrostatically charged with voltage and then sprayed onto the material substrate. In this process, the voltage and current given to the charging electrode determine the quality of the coating. Adjusting the voltage configurations influences the powder's adhesion to the substrate [77].

4
LUMINESCENCE MATERIALS

4.1. Definition of Luminescence

The phenomenon of luminescence, also referred to as "cold light," is a mechanism by which excited atoms or molecules come back to their ground state by generating photons (electromagnetic radiation) without increasing their temperature [80], [81]. It is difficult for historians of luminescence to distinguish truth from deception. Since ancient times, tales have been told about luminous materials, but in most of them, light is created by reflection rather than light radiation. It is intriguing to hear about luminous humans, but it is obvious that humans cannot ever emit a shine like that of the firefly [2].

Several ancient Chinese papers from the Song period (960–1279 A.D.) denote the picture "cow in a barn" by Z. Xu [2]. It was believed that this painting's ability to stay visible even at night time was a result of magic. It is believed that the ink used to create this artwork was imported from Japan due to the extensive marine commerce between China and Japan at the period. It is feasible for the raw materials required for the production of sulfide compounds to freely arise as a consequence of volcanism. However, the earliest scientific descriptions of the night-visible object known as the Bologna stone are found in the 1600s publications 'De Illuminabili Lapide Bononiensi Epistola' and 'Litheosphorus Sive de Lapide Bononiensi [82], [83]. Although the Italian alchemist and shoemaker V Cascariolo processed $BaSO_4$ in 1602, which is believed to be the birth of contemporary luminous materials, the term "luminescence," which means "light" in Latin, was coined in 1888 by the German scientist E Wiedemann [84]. It is also defined as being able to produce light without heat if previously lighted by sunlight or fire [82]. Amazingly, almost 400 years later, in 2012, J. Holsa and M Bettinelli et al., using modern experimental tools, demonstrated that the emits from the Stone are not made by a mysterious force. Rather, they are caused by the transition of monovalent copper impurities in the reduced product of the barite mineral $3d^9\ 4s^1 \rightarrow 3d^{10}$ [82].

Because of its aesthetic appeal and possible utility in lighting, this afterglow phenomena has drawn the interest scientists since the 17^{th} century; yet, only scattered descriptions are accessible [3], [85]. In the years before the end of the 20^{th} century, research on the creation of phosphorus materials and their genuine physical significance was restricted. Zinc

sulfide (ZnS) has been utilized for green phosphorus radiation for over a century, first with copper (Cu^{+}) and then with cobalt (Co^{+}) [86]. Similar alkaline earth sulfides were investigated by doping with Bi^{3+}, Eu^{2+}, or Ce^{3+}, and the name "phosphorus" emanates from [phosphorus], which means "bearer of light" and is the Greek personification of Venus [3], [82], [87]

Utilizing on the $Sr_2Al_2O_4$: Eu^{2+} phosphor found by V. Abbruscato in 1971, T. Matsuzawa and his colleagues [8] invented the $Sr_2Al_2O_4$:Eu^{2+},Dy^{3+} phosphor in 1996. It has a high luminosity and a light lifetime of 10 to 20 h. The integration of Dy^{3+} ions has a significant impact on the phosphor's standard features. This phosphor is extremely bright and durable in the gloomy has a green emission band compatible with human photopic eyesight, a wide excitation band appropriate for charging with conventional fluorescent lamps, and a high absorption cross-section of the parity-allowed Eu^{2+}: $4f^7 \rightarrow 4f^6\ 5d^1$ transition. In addition, it is chemically and physically stable, barring its rather inadequate moisture steadiness. In addition, it has free of radioactive elements [88], [89].

Akiyama et al.[90] studied Eu, Dy-doped strontium aluminates in their work. The usage of rare earth elements in alkaline earth aluminates has garnered a growing amount of attention. Qui et al. kept going their research by modifying the composition of the sample (MAl_2O_4:Eu^{2+}, R^{3+} (M=Sr, Ba, Ca; R=Dy, Nd, La)). When the luminescent properties of the samples that had been created were analyzed, the factors responsible for the wavelength transition from a yellowish-green hue to bluish-green hue subsequently to blueish-purple were clarified by the differentiation of compositions from $SrAl_2O_4$:Eu^{2+}, Dy^{3+} to $BaAl_2O_4$:Eu^{2+}, Nd^{3+} and then $CaAl_2O_4$:Eu^{2+}, La^{3+} [90].

Diverse production techniques have been employed in the investigation of luminescence phenomena. By synthesizing $BaMgSiO_7$:Eu^{2+}, Mn^{2+} through solid-state reaction, Sho Abe et al. were able to generate a long-lasting red light-emitting phosphor in 2005 [91]. In comparison to single-doped phosphors, he discovered that double doping boosted the light brilliance by a factor of seven. In 2007, M. K. Jung and his colleagues used a solid-state reaction to make Y_2O_3:Eu, Sm red phosphorus. They noticed that when the synthesis temperature was up, the emission spectrum became bigger [92]. In contrast to the solid state reaction, Chai Yueshang et al. produced the long-lasting fluorescent material $Sr_3Al_2O_6$: Eu^{2+}, Dy^{3+} using the sol-gel technique in a reducing environment of activated carbon [93]. Uniformity in crystallographic and luminescent characteristics cannot be attained across all methods of synthesis. The synthesis process of the solid-state reaction

method necessitates elevated temperatures owing to the relatively large size of its particles. Elevated temperatures have been observed to induce heterogeneous distribution and promote larger crystal formation. However, it has been noted that such conditions have a favorable impact on the emission lifetime. The utilization of the sol-gel method has garnered considerable attention in the production of nanoparticles [94], [95]. The sol-gel technique employs complexing agents to encapsulate small nanocrystals, thereby limiting their growth at elevated temperatures. This results in an enhancement of emission capabilities [96], [97].

In terms of phosphorescence and stability, aluminate and silicate materials doped with Eu^{2+} and Dy^{3+} emerged as the better alternatives to sulfur-based compounds in the late 20^{th} century. In systems doped with Eu^{2+} and Dy^{3+}, they serve as Eu^{2+} activators and Dy^{3+} hole traps. Y. Lin et al. developed the well-known permanent luminous silicate, $Sr_2MgSi_2O_7$:Eu^{2+}, Dy^{3+}, in 2001. However, aluminates deteriorate in the presence of water. Therefore, their application regions are restricted, and they lag behind silicates [10], [98].

4.2. Type of Luminescence

4.2.1 Luminescence by Excitation Source

When Wiedemann (in 1888) acknowledged that luminescence was the antithesis of incandescence, he classified luminescences as six categories based on their excitation mechanism. Although current theories about the process by which light emission have evolved and several new forms of luminescence have been identified, they always fall into one of Wiedemann's six classifications [99].

Photoluminescence is a luminescent phenomenon that arises from the excitation of materials by various light sources. Thermoluminescence is a technique whereby materials emit light subsequent to being subjected to heat. Electroluminescence is a form of luminescence resulting from the emission of light by an electric discharge. This electrical discharge may occur in diluted gas in a vacuum tube, in air, while rubbing silk or fur, or when stripping a tape roll. Galvanoluminescence is a luminescent phenomena caused by the chemical interactions of chemiluminescent compounds formed during electrolysis, typically by the creation of "active oxygen." Light accompanies the passage of powerful sound waves through a liquid due to electrical discharges in the remaining gas of holes created by the waves that produce sound. Triboluminescence or piezoluminescence is the

emission of light when rubbing or crushing organic or inorganic crystals of different types. Crystalloluminescence is the light that occasionally emerges when solutions crystallize. Chemiluminescence is the light produced by a chemical reaction that occurs in a gas, vapor, or solution. Bioluminescence is the emission of light by living plants and animals through chemiluminescence [99].

4.2.2 Luminescence By Lifetime

It is feasible to categorize luminescence according to the excitation sources and the decay time (τ_c). If the decay period τ_c is less than 10-8 seconds, the emission is referred to as fluorescence; otherwise, it is referred to as phosphorescence. Phosphorescence is additionally divided into short-lived (τ_c 10^{-4} s) and long-lived ($\tau_c > 10^{-4}$ s) varieties. Very short-lived (τ_c 10^{-3} s), short-lived (τ_c = s), long-lived (c = minutes), very long-lived (c = hours), and super long-lived (c > 10 hours) emissions are often categorized depending on their emission durations [100].

4.3. Types of Phosphorus

4.3.1 Aluminates Based Phosphorus

Since 1996, after Matsuzawa et al. published their study on persistent luminescence research utilizing $Sr_2Al_2O_7:Eu^{2+}$, Dy^{3+}, hundreds of papers have been written on the issue. To date, alkaline earth aluminates (MAl_2O_4, M=Ca, Sr, Ba) have been the subject of the most research. It has been researched how to synthesis $MAl_2O_4:Eu^{2+}$ utilizing efficient, low-cost, and simple processes. The most frequent approach is a solid-state reaction which takes place between 1300-1400 °C. Additionally, the firing, "Pechini," microwave LHPG, and sol-gel techniques have been effective. [101].

4.3.2 Silicates Based Phosphorus

The well-known silicate is $Sr_2MgSi_2O_7:Eu^{2+}$, Dy^{3+}. In recent years, aluminate phosphors including rare earth elements have garnered interest because to their great brightness, long luminescence, and outstanding photostability. However, upon contact to water, these phosphors have pigmentation issues. Lin et al. created $Sr_2MgSi_2O_7:Eu^{2+}$, Dy^{3+} phosphor by solid-state reaction in a reducing environment, and the crystal structure was unaffected by variations in Eu and Dy molar ratios according to the formula. The $M_2MgSi_2O_7$ family is additionally referred to as akermanites or alkaline earth. Although solid-state reaction at 1200°C-1400°C is the most typical technique for their manufacture, sol-gel,

precipitation, and combustion may also be employed effectively. Dy^{3+} and Tm^{3+}, when utilized as additional activators in the $Sr_2MgSi_2O_7:Eu^{2+}$ structure, have been shown to create phosphors that are brighter and have a longer persistence than those without additional activators [101], [102].

4.3.3 Other Compounds

In addition to aluminates and silicates, LED studies has contributed to the discovery of compounds with a somewhat persistent luminescence. Due to the hygroscopic nature of sulfur groups, their stability is weaker to that of aluminates and silicates. In contrast to their oxides, which emit in the yellow, orange, or red area, their visible region emission is moved to the red region. Phosphates are another class of luminescent compounds. One of the alkaline earth nitrido-silicates, $M_2Si_5N_8:Eu^{2+}$ (M=Ca, Sr, or Ba), has been extensively used in white LED research. They are very moisture- and temperature-resistant [101].

4.4. Mechanism of Long-Lasting Luminescence

4.4.1 Trap Hole Mechanism

In persistent phosphors, two types of activation points are commonly present: emission units and trap units. Emission centers may consist of lanthanide ions (5d→4f or 4f→4f shifts), transition metal ions (d→d shifts), or main group/post-transition metal ions (p s shifts), etc. Trap centers may exist as lattice defects, impurities, or deliberately added aliovalent or isovalent co-dopants, etc. In certain situations, emission centers might also perform as trap centers. Both the emission/trap centers are situated within the bandgap (forbidden band), and the trap centers are basically a few electron volts (eV), or more specifically less than 1 eV, underneath the lowest level of the conduction band (CB) in the case of electron traps or just over the peak of the valence band (VB) in the case of hole traps. The mechanism can be split shortly into four basic procedures:

i) Charge carriers (electrons and/or holes) are freed to irradiation at specified wavelengths when a persistent phosphor is stimulated by external stimulation;

ii) Alternative to being radiatively loosening stimulated electrons or produced holes may be trapped non-radiatively by electron or hole traps via CB or VB, respectively, or by the quantum tunneling operation via the forbidden band, which is known as the trapping

process. The traps typically do not produce electromagnetic radiation, nevertheless they hold excitation energy for an extended period of time, which is why this mechanism is sometimes known as a "optical battery";

iii) Following stopping of excitation, the collected charge carriers may be discharged basically by excitation energyiii) Following cessation of excitation, trapped charge carriers may be freed primarily by stimulation energy, an operation known as detrapping;

(iv) In the end, the emitted charge carriers return to the emission center via an operation termed recombination, where they undergo the electron-hole recombination that causes delayed luminescence.

Therefore, the features of the emission center basically define the wavelength bandwidth of interest, while the properties of the trap center, such as trap depth, trap density, and concentration, specify the intensity and duration of PersL at certain temperatures [84], [103], [104].

4.4.2 Mechanism of Persistant Luminescence

Persistent luminescence's features have prompted investigation into its fundamental mechanics. It is commonly accepted that charge carriers are captured by trap centers in the forbidden band after stimulation. Long-lasting energy levels exist in the forbidden band gap. The charge carriers are progressively released from these states and are able to generate light when they come into contact with the activators. To obtain insight into trap depths, basic models based on thermoluminescence curves have been examined, and many potential processes, spanning from simple models to more sophisticated systems, have been presented.

4.4.2.1 Model of Matsuzawa

Matsuzawa et al.[105] described the basis of $SrAl_2O_4:Eu^{2+},Dy^{3+}$ exceptional long persistent phosphors (figure 4.1). In their theory, it was supposed that holes were the central charge carriers. The notion that the fundamental charge carriers in SrAl2O4:Eu2+ are holes in the valence band was supported by Abbruscato et al., who drew upon prior research that observed a faint afterglow in the material. Subsequently, Matsuzawa and colleagues performed photoconductivity experiments in order to substantiate the hole model. Additionally, it was observed that upon photon excitation, a Eu^{2+} ion could experience a process where a hole is liberated to the valence band (VB), resulting in the formation of a Eu^{+} ion. Subsequently, the vacancy was captured by a trivalent rare earth

ion, such as Dy^{3+}, leading to the creation of Dy^{4+}. In the final analysis, the confined aperture was compelled to undergo release back into the valence band as a result of thermal energy. Subsequently, the ion underwent a conversion back into a Eu^{+} ion, facilitating its reversion to the Eu^{2+} ground state via the emission of photons [105], [106].

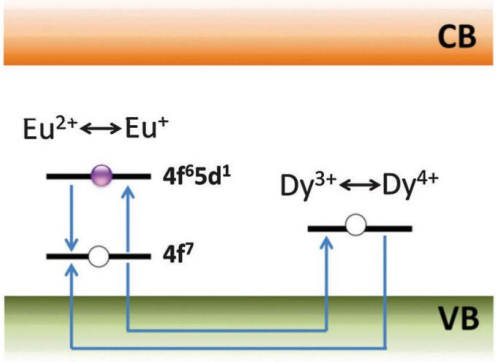


Figure 4.1 The depiction of the hole model proposed by Matsuzawa et al. through the utilization of $SrAl_2O_4:Eu^{2+},Dy^{3+}$ [107].

4.4.2.2 Model of Aitasalo

According to Aitasalo's assertion in 2003, electrons were observed experiencing excitation from the valence bands to trap levels. Based on Aitasalo's hypothesis, it is proposed that the energy level associated with traps formed by oxygen vacancies is situated higher than the energy level of the conduction band. This positioning enables the thermal transition to the conduction band. To clarify, it is postulated that the energy resulting from the interaction between electrons and traps is efficiently transferred to the luminescent center, specifically the Eu ion, via the energy transfer mechanism. Moreover, this model has offered elucidation on the impact of rare earth elements, which function as supplementary dopants during the process of doping. Nevertheless, the existence of Eu^{+} and Dy^{4+} ions within aluminate or silicate structures has been dismissed due to the chemical instability that would arise from the reduction of Eu^{2+} ions to Eu^{+} and the oxidation of Dy^{3+} ions to Dy^{4+} ions. It has been posited by researchers that the incorporation of trivalent rare earth elements into the system results in the occupation of unoccupied sites by divalent alkaline earth regions. There is an assumption that this occupation contributes to the occurrence of defects in the lattice structure of the system. Consequently, the structure has experienced the occurrence of spontaneous defect formation in order to uphold charge equilibrium. [108], [109].

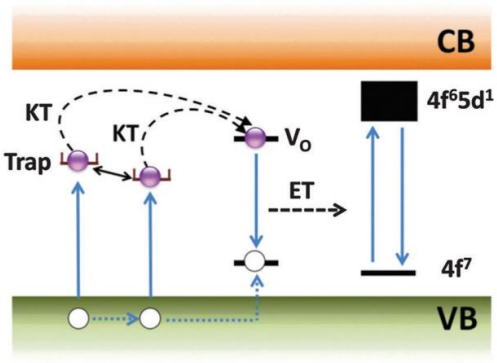


Figure 4.2 The depiction of the electron model proposed by Aitasalo et al. through the utilization of $CaAl_2O_4:Eu^{2+},Dy^{3+}$.

4.4.2.3 Model of Dorenbos

Dorenbos and colleagues acknowledged the acceptance of the Aitasalo approach. However, they proceeded to highlight the presence of flawed reasoning underlying the postulated carrier on the ground state of Eu^{2+} subsequent to excitation. These researchers pointed out that the model was based on flawed reasoning (figure 4.3). Unlike the scattered Bloch states of the valence and conduction band, the energy levels of lanthanides were restricted. In 2005, they refined the electron model and proposed an alternative model. One notable characteristic of this model involves the stimulation of electrons through the valence band instead of europium. The close proximity between the 5d energy level of the divalent europium ion and the conduction band facilitates the efficient release of these electrons into the conduction band. During the course of this phenomenon, the released ions are subsequently captured by trivalent rare earth ions. Nevertheless, the updated the model fails to consider the existence of LPP achieved through the incorporation of Eu^{2+} ions into $SrAl_2O_4$ phosphors [110], [111].

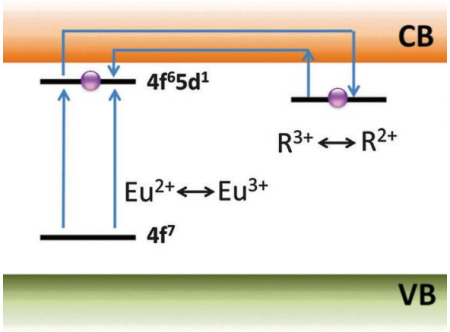


Figure 4.3 The long-lasting luminescence mechanism proposed by Dorenbos et al.

4.4.2.4 Model of Clabau

On currently with Dorenbos, Clabau et al. conducted a review of the mechanisms underlying persistent luminescence and determined necessity for revision. The Matsuzawa model was not endorsed by them for identical reasons to those of Dorenbos. The participation of Eu^{2+} in the trapping process was emphasized as a necessity. The present model bears resemblance to the Dorenbos model, albeit with notable differentiating characteristics, notably the absence of electron migration to the conduction band. The phenomenon of electron transfer between traps and luminescence centers is facilitated by direct transfer, which necessitates the proximity of europium ions and lattice defects. A further contrast to the Dorenbos mechanism pertains to the distinct nature of the traps. Upon analyzing the emission spectra of $Sr_2MgSi_2O_7:Eu^{2+}$ specimens with and without auxiliary activators, it was observed that the peak positions and magnitudes exhibited dissimilarities, while the contours remained unaltered. This observation implies that the auxiliary activator does not alter the chemical structure, thereby indicating that the lattice defects correspond to oxygen vacancies. The rationale behind the utilization of lanthanides as auxiliary activators is attributed to their capacity to sustain an equilibrium of oxygen vacancies. The stabilization of rare earth elements can be sustained by utilizing their ionization potential. This is due to the fact that a low ionization potential leads to an increase in trap depth, which in turn enables auxiliary activators to exert a strong influence on oxygen vacancies. Figure 4.4 illustrates the graph representing the trap depth of rare earth elements.

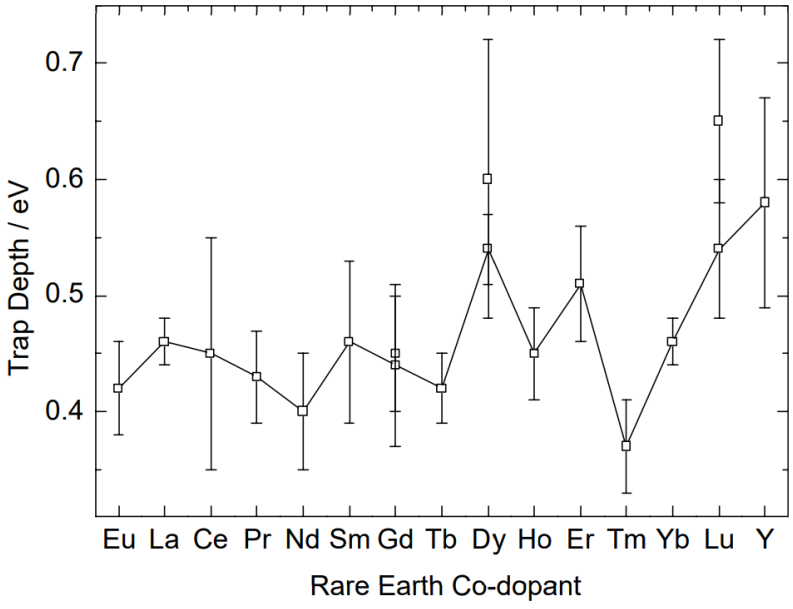


Figure 4.4 Trap depths belonging to rare earth element [108]

4.5. The Mechanism of Energy Transfer Method

The luminescence operation is intricate as the excitation and emission activities witnessed in a luminescent material are not restricted to a solitary center or atom. In order to facilitate the elucidation of the luminescence mechanism, various models have been employed, among which the Jablonski diagram (figure 4.5), commonly referred to as the "Energy Band Model," is included. Fluorescence is a phenomenon whereby an electron in the singlet ground state (S_0) gets stimulated by incident radiation to the higher singlet excited state (S_1). The stimulated electron then undergoes radiative relaxation to the ground state by releasing a photon within a brief timeframe (ns order). Phosphorescence involves the population of the triplet excited state (T_1) subsequent to the absorption of an incident photon. This process occurs through intersystem crossing (ISC), which is a spin-forbidden mechanism that enables the electron from the S_1 state to populate the T_1 state. The emission resulting from the radiative transition of the electron from the T_1 state to the S0 state exhibits a delayed onset that persists for a considerable duration subsequent to photon absorption [87]. Phosphorescence is typically not detected at room temperature due to the loss of the T_1 state into the S_0 state through non-radiative processes such as oxygen quenching ($T_1 + 3O_2 \rightarrow S_0 + 1O_2$), triplet-triplet destruction ($T_1 + T_1 \rightarrow S_0 + S_1$), and/or non-radiative relaxation ($T_1 \rightarrow S + \text{heat}$) [112]

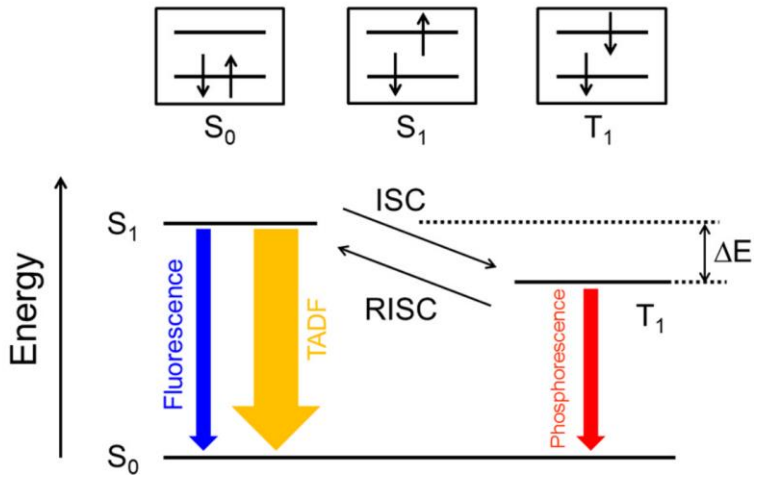


Figure 4.5 The diagram presented is a simplified form of the Jablonsky diagram [86].

4.6. Activator Atoms

Emitters are the sources of the emission wavebands; they are nuclei that are able releasing radiation after being stimulated. When activator atoms get doped into a crystal, they create radiation and defect points, leading to observable variations. As a result of the transitions

($1n^{14}$) between the partly completed $4f^n$ electron shells, electrons exist in a multitude of energy levels and emit radiation. With their $5s^2 5p^6$ electron shells completely filled, rare earth elements possess a special shielding effect. As luminous centers, a vast array of activation ions is utilized [113].

The Eu^{2+} ion is well-known as a noticeable special luminescence hub. The emission color exhibited by Eu^{2+} ions is varies depend on the crystal field effect, which is a manifestation of the electrostatic interactions between neighboring ions in the their situated system. Phosphors such as $CaAl_2O_4:Eu^{2+},Nd^{3+}$ [105] and $Sr_3MgSi_2O_8:Eu^{2+},Dy^{3+}$ [114] are well-known as having powerful blue luminescence, whereas $Ba_2MgSi_2O_7:Eu^{2+},Tm^{3+}$ [115] and $SrAl_2O_4:Eu^{2+},Dy^{3+}$ [105] are recognized for their intense green luminescence. A robust crystal field is necessary to decrease the the the weakest emitting state of an electron's arrangement $4f^6\ 5d^1$, resulting in emissions that range from yellow to red. Illustrative instances of such luminescent materials comprise $Ca_2BO_3Cl:Eu^{2+},Dy^{3+}$ [115] and $Sr_3Al_2O_5Cl_2:Eu^{2+},Tm^{3+}$ [116]. The luminescent persistent phenomenon (LPP) in the majority of Eu^{2+}-doped oxides can solely be stimulated by ultraviolet radiation. Conversely, Eu^{2+}-doped sulfides and nitrides demonstrate a red LPP when subjected to ultraviolet-visible illumination [107].

The investigation of long persistence phosphors doped with Eu^{3+} has been conducted due to their effectiveness like red-emitting phosphors. This is attributed to the copious transitions that occur between the excited $5D^0$ level and the $7\ F_J$ (J is 0, 1, 2, 3, 4) levels of $4f^6$ configuration in the orange-red light range. The majority of scholarly investigations pertaining to long persistence phosphors doped with Eu^{3+} center around oxysulfides doped with Eu^{3+} [107].

The lanthanide group features an essential afterglow activator known as Ce^{3+}. This activator possesses a $4f^1$ setting and has the ability of generating a wide emission band. This is due to the powerful crystal field connection of its 5d-4f transition energy [117]. The salient features of Lanthanide Phosphor Particles (LPPs) activated by Cerium (Ce^{3+}) are outlined as follows: (i) The host material exhibits a predominant focus on aluminate. (ii) The afterglow emission spectrum is situated within the blue light wavelength range [107].

The rare earth ion, Sm^{3+}, is well-known to produce a highly bright reddish-orange luminescence. This phenomenon is attributed to the characteristic transitions that occur

between the arrangement of electrons of Sm^{3+} in its basic state and its excited state. The luminescent property of Sm^{3+} as a significant red-emitting center has been observed in diverse material structures such as oxides, oxysulfides, and fluorides. The present study is concerned with the methodical examination of the afterglow characteristics exhibited by Sm^{3+} in stannate matrices. The substance emitted a vivid orange-red luminescence even upon brief exposure to ultraviolet radiation and demonstrated a discernible phosphorescence lasting over an hour in low-light conditions [107].

The utilization of the Pr^{3+} ion is observed in the generation of red light, which is attributed to the transitions occurring between the energy levels of $^1D_2 \rightarrow ^3H_4$, $^3P_0 \rightarrow ^3H_6$, and $^3P_0 \rightarrow ^3F_2$. The Pr3+ ions have been found in perovskite-type oxides characterized by the chemical formula ABO3 (such as $CaTiO_3$ [118], $NaNbO_3$ [119], and $SrZrO_3$ [120]). Subsequently, these ions were observed to produce red afterglow in numerous long-term phosphors.

Long-lasting phosphors doped with Tb^{3+} exhibit a high degree of efficiency in generating green long persistence, which can be attributed to the 4f inter-transition $^5D_4$ to ^7F_J (where J represents 6, 5, 4, or 3) of Tb^{3+}. The green long-lasting phosphors were generated through the radiative relaxation of the excited Tb^{3+} ion, with transitions solely occurring from the $^5D_4$ to ^7F_J states. The phenomenon of cross-relaxation between two neighbouring Tb^{3+} ions results in the attenuation of $^5D_3 \rightarrow ^7F_J$ transitions and the amplification of $^5D_4$ - ^7F_J transitions, thereby inducing a persistent green afterglow in the phosphors [121].

Dy^{3+}-doped luminescent substances are commonly chosen as a potential source of white-light due to the suitable transitions of $^4F_{9/2} \rightarrow ^6H_{15/2}$ and $^4F_{9/2} \rightarrow ^6H_{15/2}$ in Dy^{3+}. In general, the production of enduring white phosphors involves the amalgamation of extant blue, green, and red phosphors. Nevertheless, the task of producing a long-lasting phosphor that maintains a consistent white color over time is a challenging endeavor. The rationale behind this is that dissimilar phosphors typically exhibit dissimilar rates of decay. The incorporation of Dy^{3+} presents a viable prospect for attaining a luminescent afterglow emission in the visible spectrum. The emission lines of Dy^{3+} can be classified into two primary groups based on their wavelengths. These groups are observed in the blue (470-500 nm) and yellow (570-600 nm) regions of the electromagnetic spectrum, and correspond to the $^4F_{9/2} \rightarrow ^6H_{15/2}$ and $^4F_{9/2} \rightarrow ^6H_{15/2}$ transitions, respectively [107].

Long persistent phosphors that utilize Tm^{3+}, Yb^{2+}, and Yb^{3+} as the luminescent center are infrequently reported due to the potential challenge of identifying a suitable host that can produce the desired phosphorescence. The blue long-lasting phosphor in Tm^{3+}-doped $Zn_2P_2O_7$ long-lasting phosphors was investigated by Su et. Al. [122], [123]. The emitted spectrum of blue afterglow was found to be associated with the distinctive transitions of Tm^{3+}:$^1D_2 \rightarrow {}^3H_6$, $^1D_2 \rightarrow {}^3H_4$, and $^1G_4 \rightarrow {}^3H_6$. The investigation observed the presence of green long-lasting phosphor in $Sr_4Al_{14}O_{25}$: Yb^{2+},Dy^{3+} [95] and $SrAl_xO_{(1+1.5x)}$:Yb^{2+} (x = 3, 4, 5) [124] phosphors, whereas the SrS:Yb^{2+} [125] phosphors exhibited a red color. The emission observed after a certain event should be attributed to the transition from the $4f^{13}$ $5d^1$ to the $4f^{14}$ state of Ytterbium ions.

4.7. Some of Application Areas

A fluorescent lamp employs electrical energy to stimulate the mercury vapor and produce the light source. As the electrons released from the electrodes within the lamp stimulate the mercury in the fluorescent tube, it subsequently returns to its basic state, resulting in the emission of UV radiation. The phosphorescent material on the inner surface of the fluorescent lamp facilitates the conversion of UV light into visible light [126]. The internal structure of the fluorescent tubes is depicted in Figure 4.6.

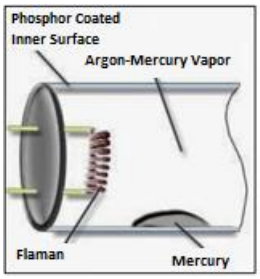


Figure 4.6 The internal structure of a fluorescent tube [126]

LEDs, which is an abbreviation for Light Emitting Diodes, are electronic components that emit light and are based on semiconductor science. The emission of photons, resulting from the motion of electrons towards the vacancies in the p/n junction, is facilitated by the application of the appropriate voltage in the correct direction. This process involves the conversion of energy, and is influenced by chemical factors. Light Emitting Diodes (LEDs) emit electromagnetic radiation within a limited spectrum in the visible region. The production of white LED lighting is achieved through the utilization of fluorescent and phosphorescent materials in conjunction [127].

The cathode ray tube (figure 4.7) is an electronic device utilized for image production and integrated with circuit networks. It finds application in various instruments, including television receivers, radar screens, and oscilloscopes. The cathode ray tube is comprised of a pair of glass tubes that have been emptied of their contents. The interior surface of the glass tube is coated with a substance that exhibits phosphorescence. Located at the opposite extremity of the tube is an electron gun. The excitation of atoms in a phosphorescent material on a screen is caused by the impact of electrons, resulting in the emission of light [128].

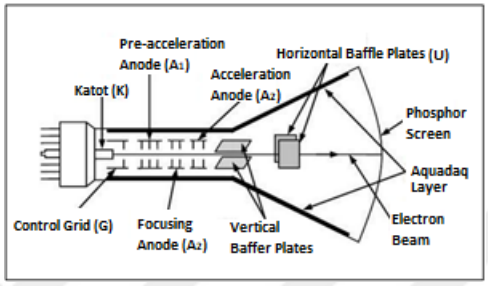


Figure 4.7 The cathode ray tube [129].

5
EXPERIMENTAL PROCEDURE

5.1. Materials

The raw materials for the Pr^{+3}/Dy^{+3} co-doped and Er^{+3}/Dy^{+3} co-doped $SrAl_2Si_2O_8$ systems, the ground layer, intermediate layer, top layer glass-ceramic system, and mill additive materials such as quartz (SiO_2), clay, sodium nitrite($NaNO_2$), acid boric (H_3BO_3) were provided by Akcoat Advanced Chemical Coating Materials, located in Sakarya, Turkey. Additionally, all necessary instrumentation for this research was supplied by the same company.

5.2. Synthesis of Pr^{+3}/Dy^{+3} co-doped and Er^{+3}/Dy^{+3} co-doped $SrAl_2Si_2O_8$

The silicate-based glass-ceramic systems, which incorporates Pr^{+3}/Dy^{+3} ions and Er^{+3}/Dy^{+3} ions, was prepared through the traditional melt-quench technique, utilizing the hypothetical formulation presented in Table 5.1. The synthesis procedures were carried out for each system in accordance with the illustration presented in Figure 5.1.

Table 5.1 The theoretical composition of oxides in the specimens.

Oxides \ Systems	**Pr^{+3}/Dy^{+3} co-doped $SrAl_2Si_2O_8$**	**Er^{+3}/Dy^{+3} co-doped $SrAl_2Si_2O_8$**
SiO_2	45 %wt	45 %wt
SrO	30 %wt	30 %wt
Al_2O_3	15 %wt	15 %wt
Li_2O	4 %wt	4 %wt
B_2O_3	4 %wt	4 %wt
Pr_6O_{11}	1 %wt	-
Er_2O_3	-	1 %wt
Dy_2O_3	1 %wt	1 %wt

The fundamental constituents were quantified in batches of 100 g (including additional ions) and thoroughly mixed to produce a uniformly distributed batch as per the previously stated composition formula. Subsequently, the admixtures were transferred to crucibles made of alumina-silicate and subjected to a temperature of 1550°C for a duration of 1 hour, utilizing an electric furnace. Subsequently, the Pr^{+3}/Dy^{+3} co-doped and Er^{+3}/Dy^{+3} co-doped $SrAl_2Si_2O_8$ systems were synthesized into a frit utilizing the melt-quenching technique. The granular frit compositions were subjected to filtration and subsequently dried for a duration of 24 hours at a temperature of 100°C.

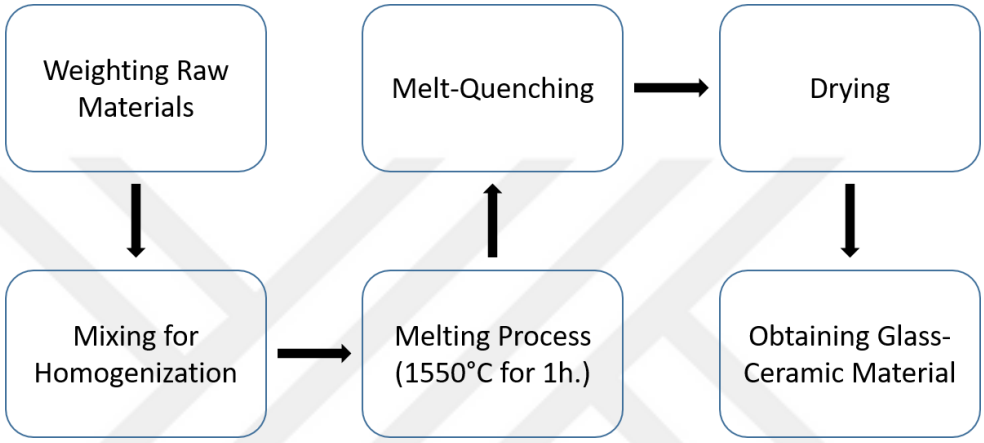


Figure 5.1 Representation of the steps involved in the synthesis process of the Pr^{+3}/Dy^{+3} co-doped and Er^{+3}/Dy^{+3} co-doped $SrAl_2Si_2O_8$ systems.

5.3. Frit Preparation

The frit design was formulated utilizing the Seger approach to achieve the desired properties, resulting in the acquisition of the recipe. The raw materials were carefully measured according to the prescribed recipe and then loaded into a crucible made of alumina-silica. The melting process was conducted at a temperature of 1300±50°C for a duration of 1 hour. The melted substance is poured into a water, thereby initiating a rapid cooling process, resulting in the formation of a solid material known as frit. The obtained granular frit underwent filtration and was subjected to a temperature of 100°C for a duration of 1 day, following which its water was removed.

5.4. Sample Preparation

Having a 300-gr limit, the alumina-zirconia ball mill was used for all grinding processes. The 300-gr capacity mill was filled with all of the ground, intermediate, and top coat glass-ceramic coatings, whose formulae are shown in Table 5.2, and it operated for 17

min. In addition, the acquired Pr^{+3}/Dy^{+3} co-doped and Er^{+3}/Dy^{+3} co-doped $SrAl_2Si_2O_8$ was ground in a ball mill with a 300-gr capacity and passed through a 200-mesh (74μm) sieve.

Table 5.2 The recipes of the ground, intermediate and top coats.

Ground Coat		Intermediate Coat		Top Coat	
SiO_2-B_2O_3-Na_2O-CaO-Based Frit	100%	SiO_2-B_2O_3-Na_2O-TiO_2-Based Frit	100%	SiO_2-B_2O_3-Na_2O-ZnO-Based Frit	100%
Quartz	10%	Clay	5%	Clay	5%
Clay	6%	Sodium Aluminate	0.3%	Sodium Aluminate	0.3%
Sodium Nitrite	0.2%	Potasium Carbonate	0.2%	Potasium Carbonate	0.2%
Acid Boric	0.2%				

While preparing samples using the 3-coat-3-firing coating method, each coat was applied according to the Figure 5.2 flowchart. The Pr^{+3}/Dy^{+3} co-doped and Er^{+3}/Dy^{+3} co-doped $SrAl_2Si_2O_8$ as a mill additive was used in varied quantities in the top (transparent) coating mix, and the samples were given the names shown in Table 5.3. The coating recipe was ground, then sieved through a 60-mesh sieve before being mixed with water up to 40% (120–150 mL) of the amunt of frit to produce a coating slurry. The coating slurry was prepared for application by being homogeneously distributed throughout the water for two minutes using a mixer.

Table 5.3 Denotations of the samples.

Sample Code	**Addition**
STD	None
5Pr	5 wt.% Pr^{+3}/Dy^{+3}-codoped $SrAl_2Si_2O_8$
10Pr	10 wt.% Pr^{+3}/Dy^{+3}-codoped $SrAl_2Si_2O_8$
20Pr	20 wt.% Pr^{+3}/Dy^{+3}-codoped $SrAl_2Si_2O_8$
40Pr	40 wt.% Pr^{+3}/Dy^{+3}-codoped $SrAl_2Si_2O_8$
5Er	5 wt.% Er^{+3}/Dy^{+3}-codoped $SrAl_2Si_2O_8$
10Er	10 wt.% Er^{+3}/Dy^{+3}-codoped $SrAl_2Si_2O_8$
20Er	20 wt.% Er^{+3}/Dy^{+3}-codoped $SrAl_2Si_2O_8$
40Er	40 wt.% Er^{+3}/Dy^{+3}-codoped $SrAl_2Si_2O_8$

5.5. Coating Procedures

Preceding the application of the coating, the steel surface with dimension of 10 cm x 10 cm in accordance with the EN 10209 standard, underwent surface cleaning procedures. The elemental composition of the metal substrate is given in Table 5.4. Following the cleaning procedure, subsequent steps of hot rinsing, cold rinsing, and drying were executed. The coating procedures were conducted through manual application of the wet spray technique, followed by laboratory-scale crystallization procedures. The sample of ground coating that was coated onto the metallic surface through the wet spray technique underwent preheating at a temperature of 110°C until complete evaporation of water occurred. Following the drying stage, the material experienced a thermal treatment at a temperature of 820°C for a duration of 4 min, with the aim of occurrence of a glass network structure and controlling the process of crystallization. Subsequently, the intermediate coat specimen was applied onto the ground coat via spraying technique. Following the process of being subjected to evaporating water in a furnace, the object in

question underwent a subsequent firing procedure at a temperature of 820°C. Subsequently, a luminescent glass-ceramic systems additive was incorporated into a transparent cover coat glass-ceramic coating, which was then applied onto the aforementioned coated layers via the wet spray technique. Following dehydration through oven treatment, the sample was subjected to a firing process at a temperature of 820°C for a duration of 4 min. The cooling procedure was conducted at ambient temperature. The samples were prepared in accordance with the specified procedures.

Table 5.4 Elemental composition of metal substrate

Elements of Steel Composition	Elemental Persentages of Steel
Fe	99,5
C	0,0071
Si	0,0093
Mn	0,196
P	0,0118
S	0,0058
Cr	0,02
Mo	<0,003
Ni	0,008
Al	0,05
Co	<0,002
Cu	0,02
Nb	0,006
Ti	0,115
W	0,008

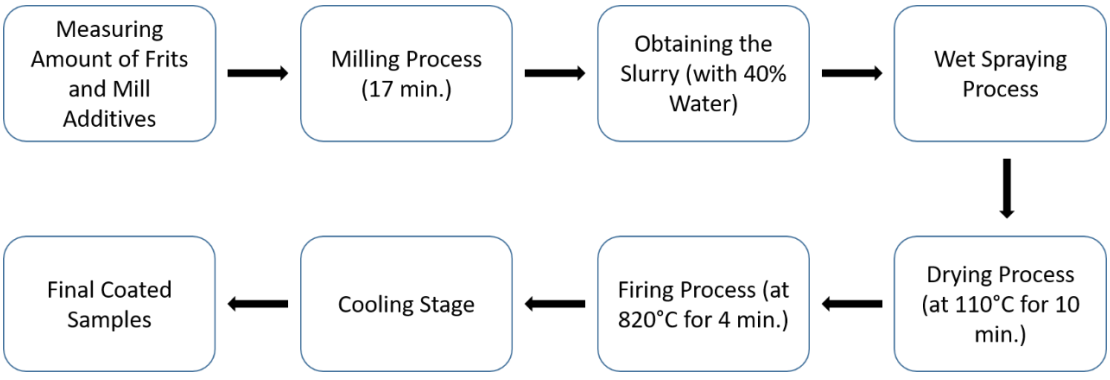


Figure 5.2 Representation of the steps involved in the coating process.

6
CHARACTERIZATION PROCEDURE

6.1. Chemical analysis

The chemical formula of the created frits was determined through the utilization of X-ray fluorescence (XRF) analysis, using the Bruker AXS S8 Tiger XRF (USA) instrument. The objective of this analysis was to verify the chemical composition and ratios of the frit, and to ensure precise interpretation of the findings, the oxide percentages of the frit were also assessed.

6.2. Phase Analysis

Phase analysis was carried out to ascertain the crystal structures that occurred at the crystallization temperatures that were identified during the pre-firing and DTA analyses. The Pr^{+3}/Dy^{+3} co-doped and Er^{+3}/Dy^{+3} co-doped $SrAl_2Si_2O_8$ system's crystal structure and phase formations were identified through employment of an X-Ray Diffractometer (XRD) (Bruker XRD D8 Advance, USA). The X-ray diffraction (XRD) patterns were obtained by compacting Pr^{+3}/Dy^{+3} co-doped and Er^{+3}/Dy^{+3} co-doped $SrAl_2Si_2O_8$ powders and utilizing Cu K radiation at x-ray generator parameters of 40 kV and 25 mA. The scanning range was set to 2θ: 10°–70° with a step size of 0.02° for data acquisition. The study employed the Raman RXN1, MR Probe device from Kaiser Optical System, which employs an Invictus Diode Laser with a wavelength of 785 nm, to investigate the correlation between the glass network structure and glass characteristics using Raman Spectroscopy.

6.3. Microstructural analysis

The present study employed scanning electron microscopy (SEM) technology in conjunction with energy dispersive spectrometry (EDS) analysis to investigate the cross-sectional area of the Pr^{+3}/Dy^{+3} co-doped and Er^{+3}/Dy^{+3} co-doped $SrAl_2Si_2O_8$ embedded glass-ceramic coating (Zeiss Supra 50VP, Germany). The Scanning Electron Microscopy (SEM) analysis was conducted using an acceleration voltage of 20 kV and a working distance of 10 mm.

6.4. Thermal Analysis

The utilization of a thermal microscope enables precise evaluation of the thermal characteristics exhibited by glass-ceramics. The samples were subjected to a heating rate of 10 °C/min using a hot stage microscopy (TA Insturment, Misura HSM 687, USA) device until their respective melting temperatures were attained. Subsequently, the sintering, softening, hemispherical, spherical, and melting temperatures were ascertained. The present study employs the Differential Thermal Analysis (DTA) technique using the Netzsch STA 449F1A-0207-M equipment to differentiate temperature fluctuations that result from exothermic and endothermic reactions, encompassing phase transitions, deterioration, and the creation or transformation of crystals. The experiment involved subjecting around 15 mg of powder, which was placed in an alumina crucible, to a temperature of 1200°C in an air atmosphere. The temperature was increased at a rate of 10°C per minute. Subsequently, an analysis was conducted.

6.5. Optical Analysis

An analysis was conducted on the emission peaks and chromatographic specification of the Pr^{+3}/Dy^{+3} co-doped and Er^{+3}/Dy^{+3} co-doped $SrAl_2Si_2O_8$ embedded glass-ceramic coated samples using the Edinburgh Instruments Spectrofluorometer FS5 (UK).

6.6. Chemical Corrosion Resistance Analysis

A cold test was carried out in compliance with the ISO 28706-1 standard to evaluate the chemical corrosion resistance of the glass-ceramic coatings with regard to their capacity to endure citric acid. A solution is prepared by combining 10 grams of citric acid monohydrate ($C_6H_8O_7.H_2O$) with 100 ml of distilled water (H_2O). A volume of 4 milliliters of solution is applied onto the surfaces coated with glass-ceramic material, at an ambient temperature, and subsequently allowed to rest for a duration of 15 minutes while being covered [130].

6.7. Surface Profilometer

The surface profilometer is a metrological device utilized for the purpose of topographical investigation of the topmost layer of a sample. The measurement method in question is multipoint in nature and takes into account the primary form of material as well as its sub-micron textural variations, which are commonly described in terms of dimensional

fractality and surface roughness. The analysis of surface profilometer was conducted utilizing the Zeiss Smartzoom 5 (Germany) devices and ConfoMAP ST 8.0 software.

6.8. Gloss Determination

The gloss of the material was assessed utilizing the TQC Sheen Polygloss glossmeter device at a 60° angle, at five distinct locations. The reported values represent the arithmetic average of a set of five measurements [131].

6.9. Thickness measurement

Following the application of the coating and subsequent firing process, an analysis was conducted to determine the distribution of coating thickness uniformity. The ISO 2178:2016 standard was employed for this purpose, utilizing a DeFelsko Positest DFT Combo model coating thickness gauge.

7
RESULT AND DISCUSSION

7.1. Characterization of Glass-Ceramic Coating

The application of glass-ceramic (enamel) coatings on metal substrates can be done in a number of ways, including 1-coat-1-firing, 2-coat-2-firing, and 3-coat-3-firing. The basic goal of the ground coat that is put to the metal substrate is to guarantee that the coating and metal surface adhere to one another. One of the most crucial oxides needed for metal and coating adhesion is CoO, and it is included in the ground coat composition based on SiO_2-B_2O_3-Na_2O-CaO-Al_2O_3. The coating will cling to the metal substrate if a ground coat is used. To make the most of photons striking the coated surface, an intermediate coat based on SiO_2-B_2O_3-Na_2O-TiO_2 was used, which has high quantities of TiO_2 to provide a white tone. To enable effective luminescence of the Pr^{+3}/Dy^{+3} co-doped and Er^{+3}/Dy^{+3} co-doped $SrAl_2Si_2O_8$, a transparent glass-ceramic coating based on SiO_2-B_2O_3-Na_2O-ZnO, which possesses remarkable transparency for top coat, was selected. The chosen coating layers have been formulated similarly to promote adhesion between them. The coating compositions are founded on SiO_2-B_2O_3-Na_2O, and the table 7.1 demonstrates the XRF analysis outcomes.

Table 7.1 The oxide composition of traditional coatings.

Oxide Group		**Amount of Ground Coat %**	**Amount of Intermediate Coat %**	**Amount of Top Coat %**
RO_2	SiO_2 TiO_2 ZrO_2	50.72	62.57	54.49
R_2O_3	Fe_2O_3 Cr_2O_3 Sb_2O_3 B_2O_3 Al_2O_3	22.04	17.82	12.89

Table 7.1 The oxide composition of traditional coatings (Continue).

R_2O	Na_2O K_2O Li_2O	16.73	15.39	15.36
RO	CaO MgO BaO CoO CuO MnO	7.96	1.06	14.23
Others	P_2O_5 MoO_3 F_2	2.55	3.16	3.03

A heating microscopy analysis was conducted to investigate the thermal characteristics of glass-ceramic coating materials during the firing process. Figure 7.1 displays the thermal behavior graph, while Table 7.2 presents the specific temperature values derived from the thermal microscope analysis. The crucial factor in the firing procedure of glass-ceramic coating is the point at which the melting temperature is reached, resulting in the complete fluidization of the glass-ceramic coating. This phenomenon facilitates the improvement of the chemical bonding between the coating and the metallic substrate. Hence, glass-ceramic coatings with a ground coat that possesses a lower melting point in comparison to other coatings have been favored. Furthermore, it is desirable for the intermediate coating composition to possess the utmost melting temperature so as to establish a thermal barrier between the ground coat and top coat, thereby impeding their amalgamation in the molten state. The determination of the firing temperature is predicated upon the melting temperature of the top coat.

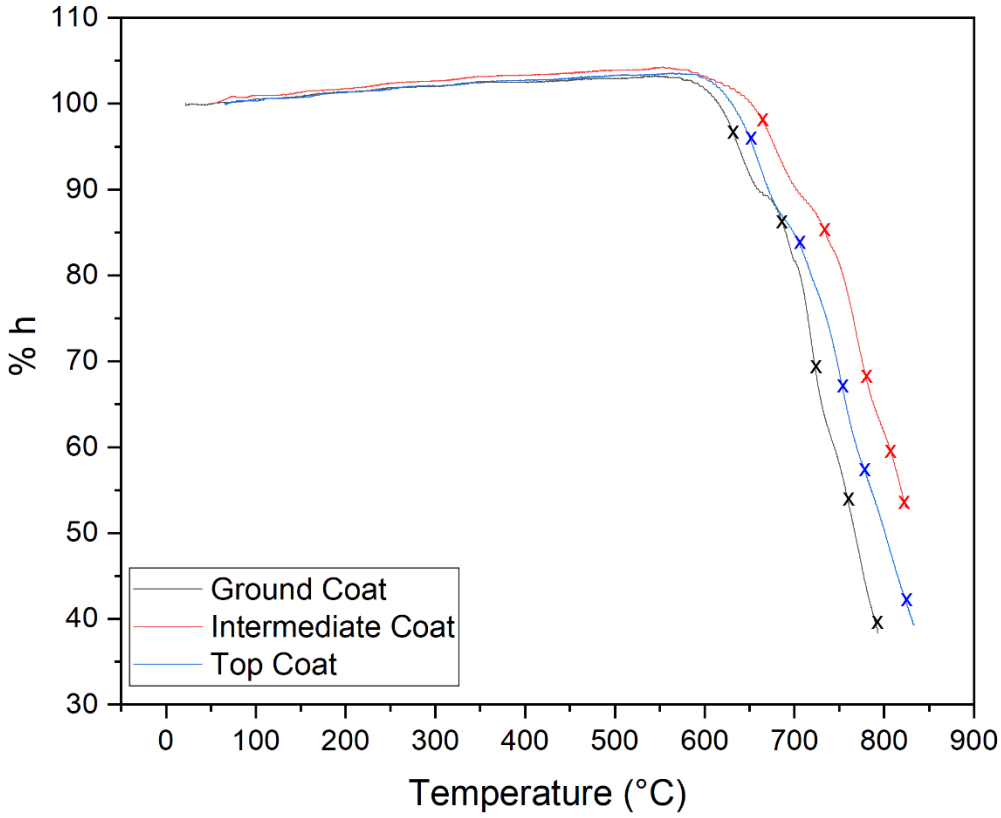
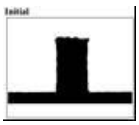
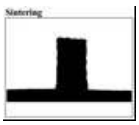
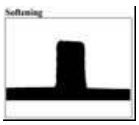
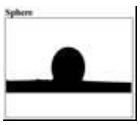
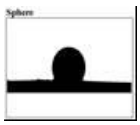
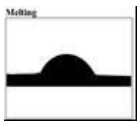


Figure 7.1 Specific temperature points and behaviors of traditional coating samples in the analysis of the thermal microscope.

Table 7.2 Specific temperature points and behaviors of traditional coating samples in the analysis of the thermal microscope.

	Temperature (°C)					
	Initial	Sintering	Softening	Sphere	Half-Sphere	Melting
						
Ground Coat	20°C	633°C	682°C	724°C	760°C	791°C
Intermediate Coat	20°C	663°C	735°C	775°C	812°C	845°C
Top Coat	20°C	649°C	704°C	754°C	780°C	822°C

Cross-sectional images captured with scanning electron microscopy (SEM) and elemental mapping images collected by energy-dispersive X-ray spectroscopy (EDS) of a standard glass-ceramic coating prepared for addition of various amounts of Pr^{+3}/Dy^{+3} co-doped and Er^{+3}/Dy^{+3} co-doped $SrAl_2Si_2O_8$ are depicted in figure 7.2a and figure 7.2b. The microstructural analysis images of the standard sample indicate that the specimens (figure 7.2c) were subjected to analysis using a carbon-based holder (figure 7.2h), and that a calcium-based ground coat (figure 7.2e), a titanium-based intermediate coat (figure 7.2f), and a zinc-based transparent glass ceramic coating (figure 7.2g) were applied to the metal substrate. (figure 7.2d).

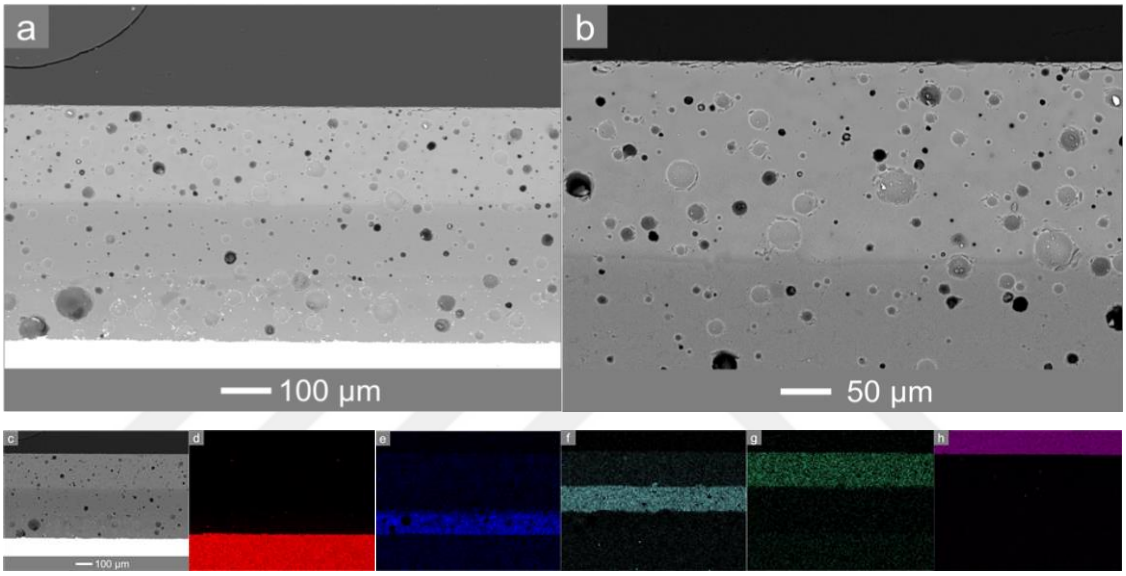


Figure 7.2 SEM images of standart coat at a) 100µm and b) 50µm and mapping images of c) standart, d) Fe, e) Ca, f) Ti, g) Zn and h) C elements using EDS analysis.

The scanning electron microscopy (SEM) technique was employed to visualize the adhesion mechanism between the ground coat and the surface of metal substrate, as well as the bonding mechanisms between the coating layers. The details of this are illustrated in figure 7.3. Figure 7.3a depicts a cross-sectional image of an unaltered glass-ceramic coating at a magnification of 4 um (Figure 7.3d). The dendritic structures that have formed between the metal substrate and the primer coating are visible, which is attributed to the presence of adhesion agents in the primer layer. Furthermore, Figure 7.3c and Figure 7.3b illustrate the bonding mechanism between the primer layer and the middle layer, and between the middle layer and the top layer, correspondingly.

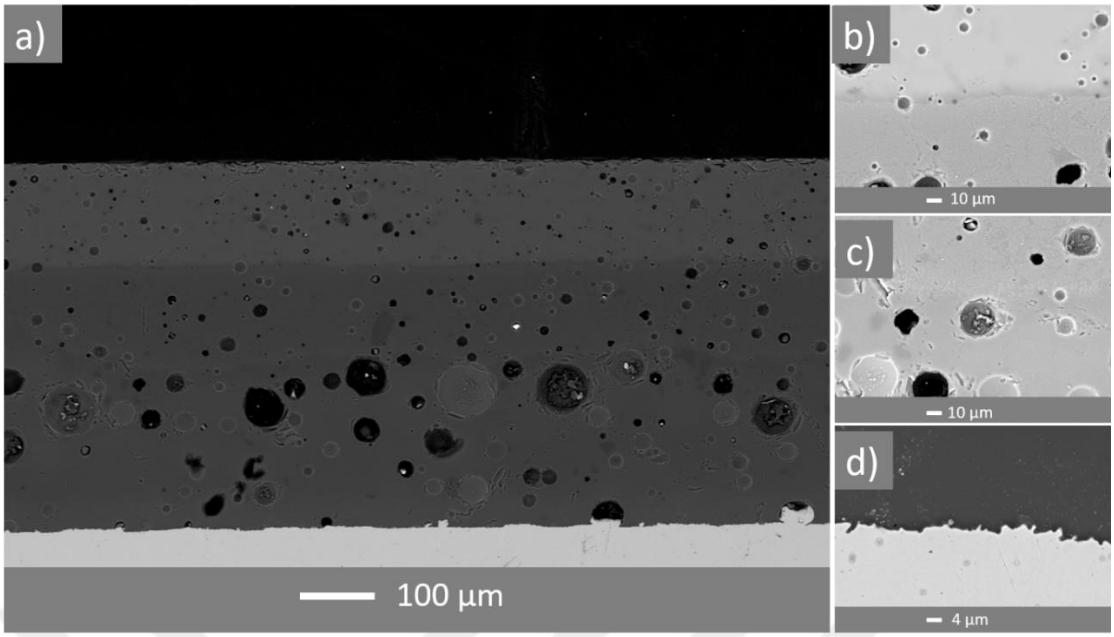


Figure 7.3 SEM images of the (a) standard coating show (d) the dentritic structures formed between the metal substrate (downside) and the ground coating (upside), as well as (c) the adhesion between the ground coat (downside) and intermediate coat (upside) and (b) between the intermediate coat(downside) and top coat (upside).

7.2. Characterization of $SrAl_2Si_2O_8$

Silicon dioxide (SiO_2) has been recognized as an extremely effective glass former since ancient times [132]. It is anticipated that the integration of SiO_2 into the glass framework will occur via $[SiO_{4/2}]0$ tetrahedral configurations, and whole oxygen atoms in SiO_4 are mutually shared. The introduction of glass modifiers such as SrO results in the formation of [Si-O-] terminations through the disruption of Si-O-Si bonds that constitute the fundamental network structure of the glass. The depolymerization of the structure results in the formation of meta-, pyro-, and ortho-silicates, namely $[SiO_{4/2}]^0$, $[SiO_{3/2}O]^-$, $[SiO_{2/2}O_2]^{2-}$, $[SiO_{1/2}O_3]^{3-}$, and $[SiO_4]^{4-}$, as demonstrated in the subsequent equations [133].

$$2[SiO_{4/2}]^0 + SrO = 2[SiO_{3/2}O]^- + Sr^{2+} \quad (12)$$

$$2[SiO_{2/2}O2]^{2-} + SrO = 2[SiO_{1/2}O_3]^{3-} + Sr^{2+} \quad (13)$$

While the increase in the amount of Al_2O_3 present in the glass matrix, the gradual increase in octahedral occupancy rate of aluminum ions is observed. Once the concentration of Al_2O_3 surpasses a specific threshold, the tetrahedral occupancy rate becomes the prevailing factor. It is believed that Al^{3+} ions possessing octahedral coordination have the ability to weaken the glass network by interfering with the silicate chains, much like the conventional glass modifiers. It is anticipated that Al_2O_3 will function as both a glass former and a glass modifier [134], [135]. The inclusion of B_2O_3 in the medium serves as an additional glass former that aids in the formation of the material's frame structure, alongside the fundamental glass former, SiO_2. Furthermore, it exerts a favorable impact on the process of glass melting through the reduction of melt viscosity and synthesis temperature [136].

C. Zhang [137] and their research team conducted a thorough investigation and analysis of the triple phase diagram of $SrO\text{-}Al_2O_3\text{-}SiO_2$. The present study encloses the procurement of binary and triple-phase diagrams to ascertain the existence of stable, semi-stable, single, and multiple phases within the $SrO\text{-}Al_2O_3\text{-}SiO_2$ system. Through the interpretation of the acquired triple phase diagram, the requisite composition and temperature for the attainment of the $SrAl_2Si_2O_8$ structure were discerned. The results of the XRF analysis are presented in Table 7.3.

Table 7.3 The XRF analysis result of $SrAl_2Si_2O_8$ system.

Oxides	**Amount (wt%)**
SiO_2	45.52
SrO	31.21
Al_2O_3	14.91
Li_2O	4.12
B_2O_3	4.24

The presence of glass formers, namely B_2O_3 and SiO_2, exerts a significant influence on the formation of glass. As the ratio of SrO within the glass matrix increases, there is a decrease in the quantity of connections present within the network structure of the glass.

The findings indicate that SrO functions as a network modifier, inducing structural reversal by disrupting the network bonds within the SiO tetrahedral framework. Within the disrupted network, Sr^{2+} cations are situated in interstitial positions and are encompassed by non-bridging oxygen [138]. The $SrAl_2Si_2O_8$ compound exhibits a monoclinic phase and possesses an irregular hexahedron shape. The compound's structure involves the combination of Sr^{2+} ions with eight oxygen atoms, while Al^{3+} and Si^{4+} ions combine with four oxygen atoms to form AlO_4 and SiO_4 tetrahedrons. The tetrahedrons are interconnected at their vertices, resulting in the formation of a network consisting of eight members [139].

The bonds between the components of the luminescent glass-ceramic system were investigated using Raman spectroscopy. Studying [140]–[145] minerals from the feldspar and danburite groups helped us understand the analysis's findings, which are shown in Figure 7.4. Peaks between 1200 cm^{-1} to 900 cm^{-1} wavelength range are caused by the symmetric/antisymmetric stretching vibrations produced by the TO_4 tetrahedra (T = Si and Al). The bending deformation of the TO_4 tetrahedra is what causes the peaks in the 800 cm-1 to 600 cm-1 wavelength region. Stretching, bending, and breathing are all related with vibrations generated by four-membered Si(Al)-O-Si(Al) rings, which are represented by peaks in the 600 cm^{-1} to 400 cm^{-1} wavelength range. Peaks below 400 cm^{-1} are caused by the interaction of the SiO_4 and AlO_4 tetrahedra's rotation, translation, and deformation, as well as the external bending motion of an enormous cation (such as Ba and Sr) [146].

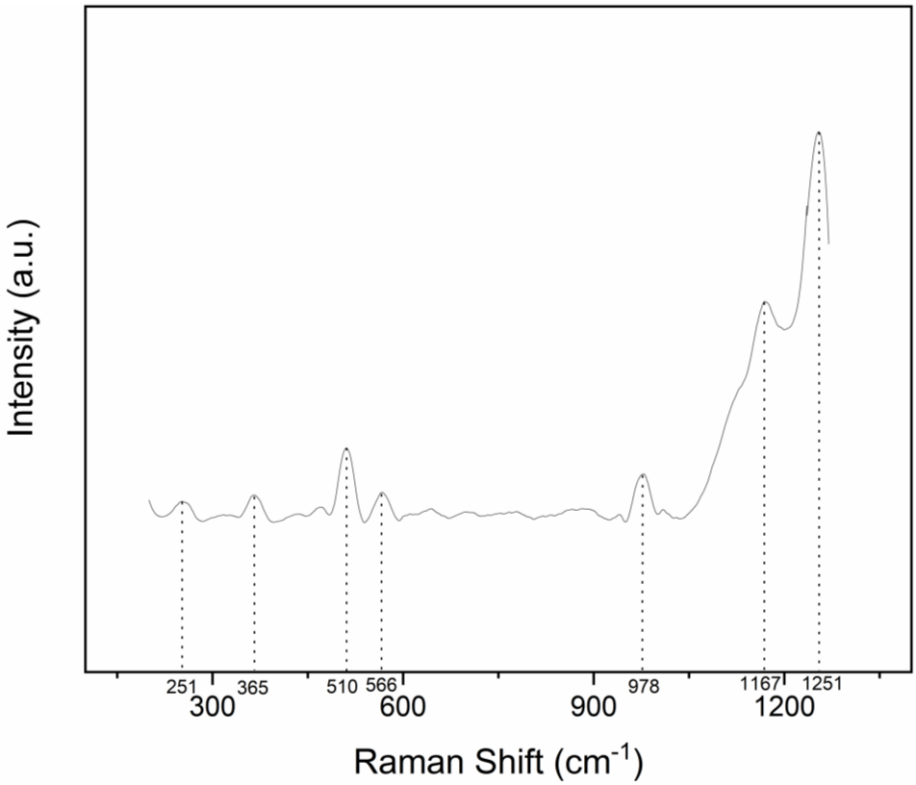


Figure 7.4 The Raman spectrum analysis of the $SrAl_2Si_2O_8$ glass-ceramic system.

The Raman spectroscopy performed on the specimen reveals the existence of distinctive peaks of the aluminosilicate glass system [147]. The detected peaks located at 279 cm^{-1}, 334 cm^{-1}, and 394 cm^{-1} are thought to arise from the vibration of Sr^{2+} ions and the associated vibration of Sr–O and TO_4 in a crystal structure that exhibits long-range order. The spectral peak detected at a wavelength of 510 cm^{-1} corresponds to the bending oscillations of bridged oxygen atoms present in the Si-O configuration, as well as the displacement of bridging oxygen atoms that establish T-O-T bonds. A novel peak generation has been detected at a frequency of 566 cm^{-1}, exhibiting an augmented trend as the concentration of silica diminishes and displaying a shift proclivity towards to lower frequency. In other words, the prominent peaks observed at 510 cm^{-1} and 566 cm^{-1} signify the symmetric stretching and breathing vibrations of oxygen atoms situated in three-membered and four-membered rings of TO_4 (T = Al or Si) tetrahedrons. The Raman analysis detected the stretching motion of Si-O bonds present in SiO_4 tetrahedra at wavelengths between 850 cm^{-1} and 1050 cm^{-1} [146], [147]. The results derived from experiments conducted on samples with a high silica ratio suggest that the Si-O stretching phenomenon has a majority in the SiO_4 tetrahedra cluster, which comprises a considerable number of non-bridging oxygen atoms. The symmetric stretching belonging to (Si, Al)-O tetrahedral groups is depicted in wavelengths of 1167 cm^{-1} and 1251 cm^{-1} [148], [149].

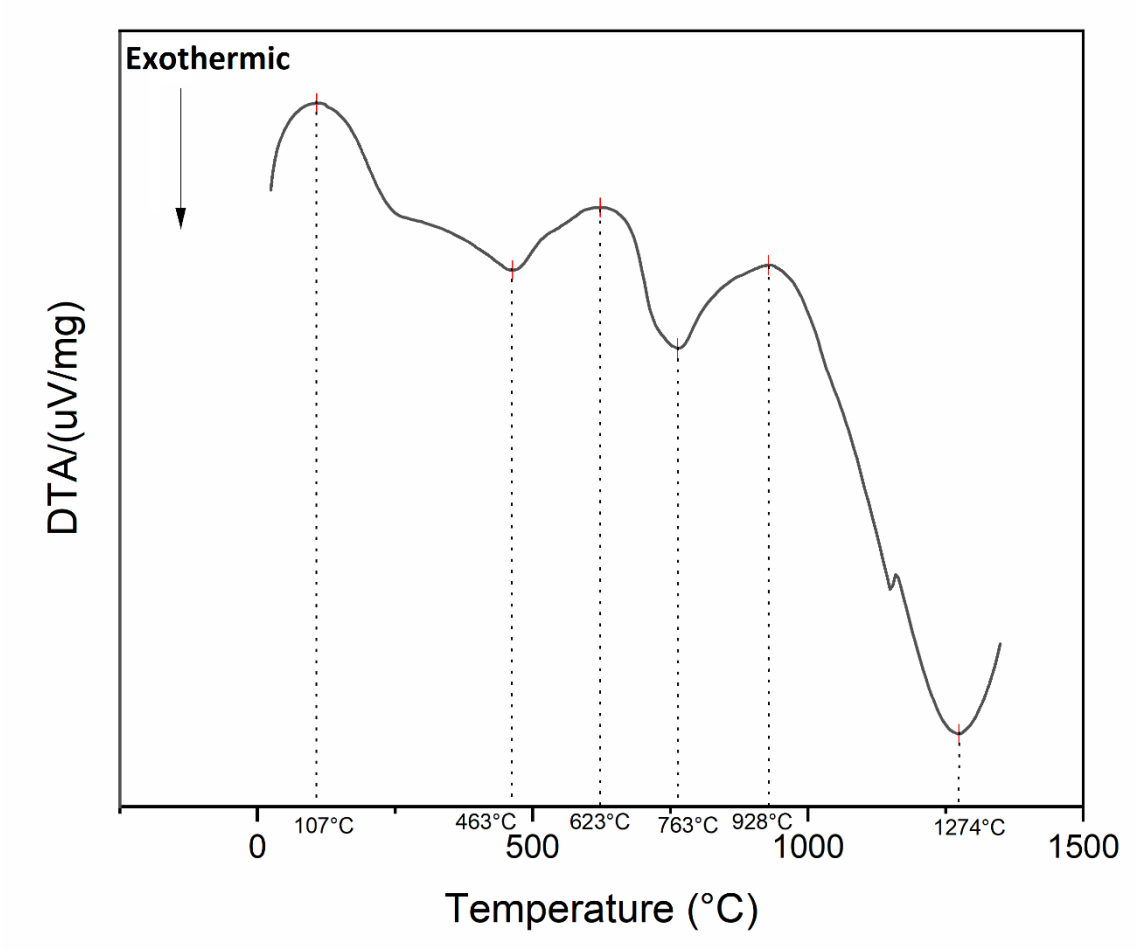


Figure 7.5 The differential thermal analysis (DTA) of the $SrAl_2Si_2O_8$ glass-ceramic system.

The luminescent glass-ceramic system underwent a differential thermal analysis (DTA), resulting in the obtaining of a graph depicted in Figure 7.5. The graph demonstrates the identification of six crucial temperatures, including the temperature at which the relative moisture was eliminated, the glass transition temperature, two crystallization temperatures, the crystal transformation temperature, and the melting temperature. The first important temperature determined in the DTA graph was 107°C, which aligns with the temperature at which the moisture content was removed. Upon raising the temperature, the glass transition temperature was found to occur at a value of 463°C. The graph reveals two significant crystallization temperatures, the first being 623°C. This temperature refers to the point at which the initial crystal formation occurred at the most rapid rate. Furthermore, it is hypothesized that the completion of the initial crystal formation occurred at a temperature of 763°C, subsequently initiating the transformation into the second crystal. The crystal that was identified second exhibited the maximum

rate of formation at a temperature of 928°C. Behind the crystallization process, the glass-ceramic system demonstrated a melting characteristic at a temperature of 1274°C.

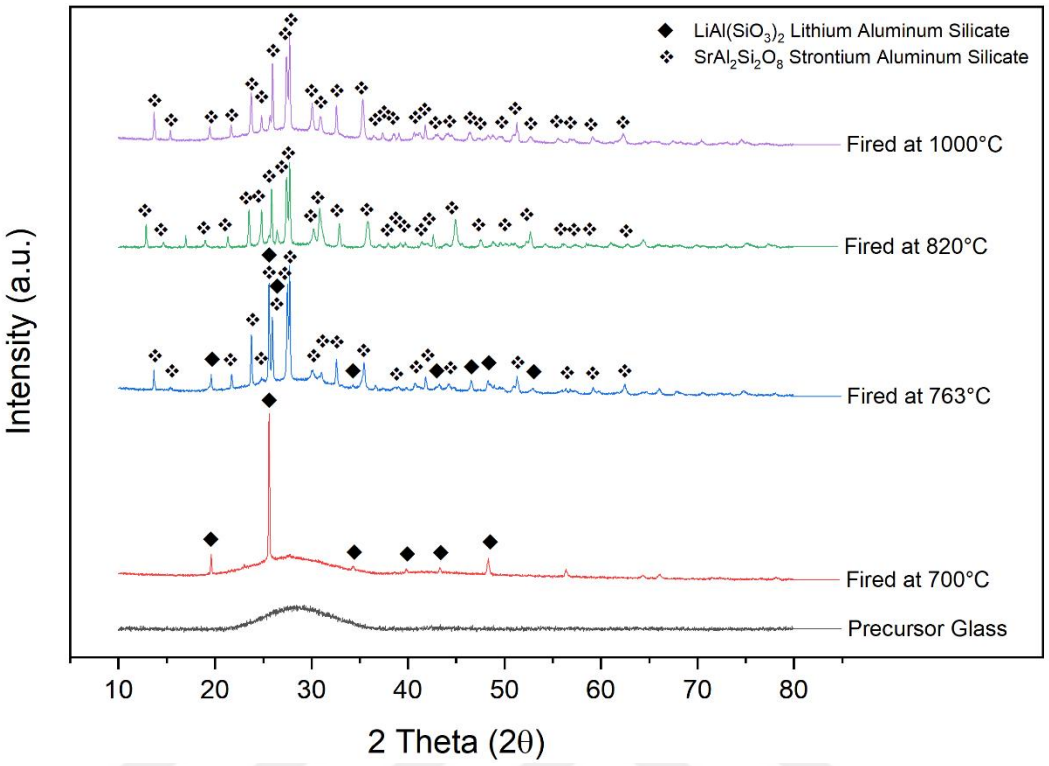


Figure 7.6 X-ray diffraction (XRD) analysis graphs of the precursor glass structure of $SrAl_2Si_2O_8$ and the after-crystallization process conducted at varying temperatures of 700°C, 763°C, 820°C, and 1000°C.

The Pr^{+3}/Dy^{+3} co-doped and Er^{+3}/Dy^{+3} co-doped $SrAl_2Si_2O_8$ system, which was produced through a fast-cooling method (quenching), performed X-ray diffraction (XRD) analysis to determine its phase composition. Without applying any heat treatment, the Pr^{+3}/Dy^{+3} co-doped and Er^{+3}/Dy^{+3} co-doped $SrAl_2Si_2O_8$ system was initially conducted XRD examination. Subsequently, the crystal formation and transformations of the Pr^{+3}/Dy^{+3} co-doped and Er^{+3}/Dy^{+3} co-doped $SrAl_2Si_2O_8$ system depending on temperature were investigated. This investigation was achieved by recrystallizing the Pr^{+3}/Dy^{+3} co-doped and Er^{+3}/Dy^{+3} co-doped $SrAl_2Si_2O_8$ system at crystallization and crystal transformation temperatures that were previously determined through DTA analysis. The crystals that were produced were subjected to X-ray diffraction (XRD) analysis, and the resulting data is presented in Figure 7.6. The Precursor glass, which is produced through rapid cooling and without any heat treatment, was found to be in a completely amorphous state. The initial crystal formation was determined through a repetition of the crystallization process of the Pr^{+3}/Dy^{+3} co-doped and Er^{+3}/Dy^{+3} co-doped $SrAl_2Si_2O_8$ system at a temperature of

700°C, which resulted in the detection of the $LiAl(SiO_3)_2$ (PDF 00-031-0706) crystal formation. In order to witness the second crystal formation that was detected through the DTA analysis, the Pr^{+3}/Dy^{+3} co-doped and Er^{+3}/Dy^{+3} co-doped $SrAl_2Si_2O_8$ system underwent recrystallization at a temperature of 1000°C, resulting in the emergence of $SrAl_2Si_2O_8$ (PDF 00-010-0015) crystal. Furthermore, the coexistence of both crystals was observed at the crystal transformation temperature, denoted as 763°C. Additionally, it was observed that the Pr^{+3}/Dy^{+3} co-doped and Er^{+3}/Dy^{+3} co-doped $SrAl_2Si_2O_8$ system underwent recrystallization at a coating firing temperature of 820°C, resulting in the formation of $SrAl_2Si_2O_8$ crystal.

It is that the $LiAl(SiO_3)_2$ crystal, which was created at 623°C and determined by XRD analysis, was caused by the effect of cationic field strength of Li_2O, which was used as a crystallizing agent to the $SrO\text{-}Al_2O_3\text{-}SiO_2$ glass structure. Furthermore, the substitution of lithium with strontium at elevated temperatures and the conversion of the $LiAl(SiO_3)_2$ crystalline structure to $SrAl_2Si_2O_8$ crystal provide colloborating evidence for this hypothesis.

The glass transition temperature (Tg) of known glass systems is contingent upon the ionic radius and, consequently, the field strength of cations that do not take part in the creation of the glass network but function as charge-balancing ions [150]. Romano et al. [151] report on the observation of a trend in the behavior of viscosity in $XAlSi_3O_8$ (where X represents Li, Na, K, $Ca_{0.5}$, $Mg_{0.5}$) melt. It has been reported that the T-O bonds (where T represents Si or Al) present in aluminosilicate structures exhibit the highest strength. The introduction of a network modifier cation into the aluminosilicate structure results in the perturbation of the bonds through a process of interplay among silicon, aluminum, and the additional cation (X) to establish bonds with oxygen atoms in the structure. This phenomenon induces the disruption of said bonds. Consequently, an augmentation in the field intensity of the glass modifier cations leads to a rise in the disruption in the glass network and a surge in the likelihood of the supplementary cations establishing bonds with oxygen atoms [152], [153]. It is widely believed that the decreased glass transition temperature observed in aluminosilicate glasses is attributed to the active involvement of charge-balancing cations, which exhibit high mobility. There exists a correlation between the field strength of the cation and the diffusion coefficient, with the order of cations being Li > Na > K > Mg > Zn > Ca > Sr > Ba. The observed correlation indicates that atoms possessing greater field strength exhibit a comparatively higher rate of diffusion in

comparison to atoms with lower field strength [151]. Hence, it can be observed that Li^+ ions exhibiting higher diffusion rates in the vicinity of the glass transition temperature have a propensity to generate the metastable phase $LiAl(SiO_3)_2$ crystal.

The diffusion coefficient of alkali aluminosilicates in the molten conditionis lower than that of alkaline-earth aluminosilicates. In the case of molten alkali aluminosilicates, as the magnitude of the field strength increases, the amount of activation energy necessary for the process of self-diffusion to take place decreases. Moreover, the pre-exponential factor exhibits a corresponding increase. This is due to a decrease in cation size and a decrease in mobility of the glass-forming cations. Furthermore, it should be mentioned that an augmentation in the intensity of the field results in a reduction in the coordination number of alkali and alkaline-earth cations. This decrease provides more movement opportunities to cations with low coordination number [150]. Thus, the low-field-strength network modifier Sr^{2+} ions form a stable phase by binding to the aluminosilicate structure, while Li^+ ions dissolve in the glass network structure. Moreover, The thermal integrity of molten aluminosilicate structures has been improved by the presence of cationic charge balancers with low field strength.

7.3. Characterization of Coating Samples (with added $SrAl_2Si_2O_8:Pr^{3+},Dy^{3+}$)

The application of glass-ceramic coatings to the metal substrate was carried out in accordance with the procedures presented in Section 7.1, whereby the coatings were applied as ground, intermediate, and top coats. The metal substrate is coated with a ground coat that exhibits a thickness of approximately 150±20 μm after firing. The thickness of the intermediate coat after firing is 130±20 μm, as applied on the ground coat. Subsequently, in terms of sample preparation, a transparent coating was administered with an estimated thickness of roughly 150±20 μm. To impart luminescent characteristics, different ratios of $SrAl_2Si_2O_8:Pr^{3+},Dy^{3+}$ were involved in transparent glass-ceramic coating recipe. Samples with the designation 5Pr, 10Pr, 20Pr, and 40Pr were created by incorporating various weight percentages (5%, 10%, 20%, and 40%wt, respectively) of $SrAl_2Si_2O_8:Pr^{3+},Dy^{3+}$ into the coatings. Figure 7.7 depicts the SEM picture of these manufactured samples. In the SEM images of the glass-ceramic coating, it was found that the quantity of $SrAl_2Si_2O_8:Pr^{3+},Dy^{3+}$ per unit area rose when the amount of $SrAl_2Si_2O_8:Pr^{3+},Dy^{3+}$ (shown in red) in the coating formula increased.

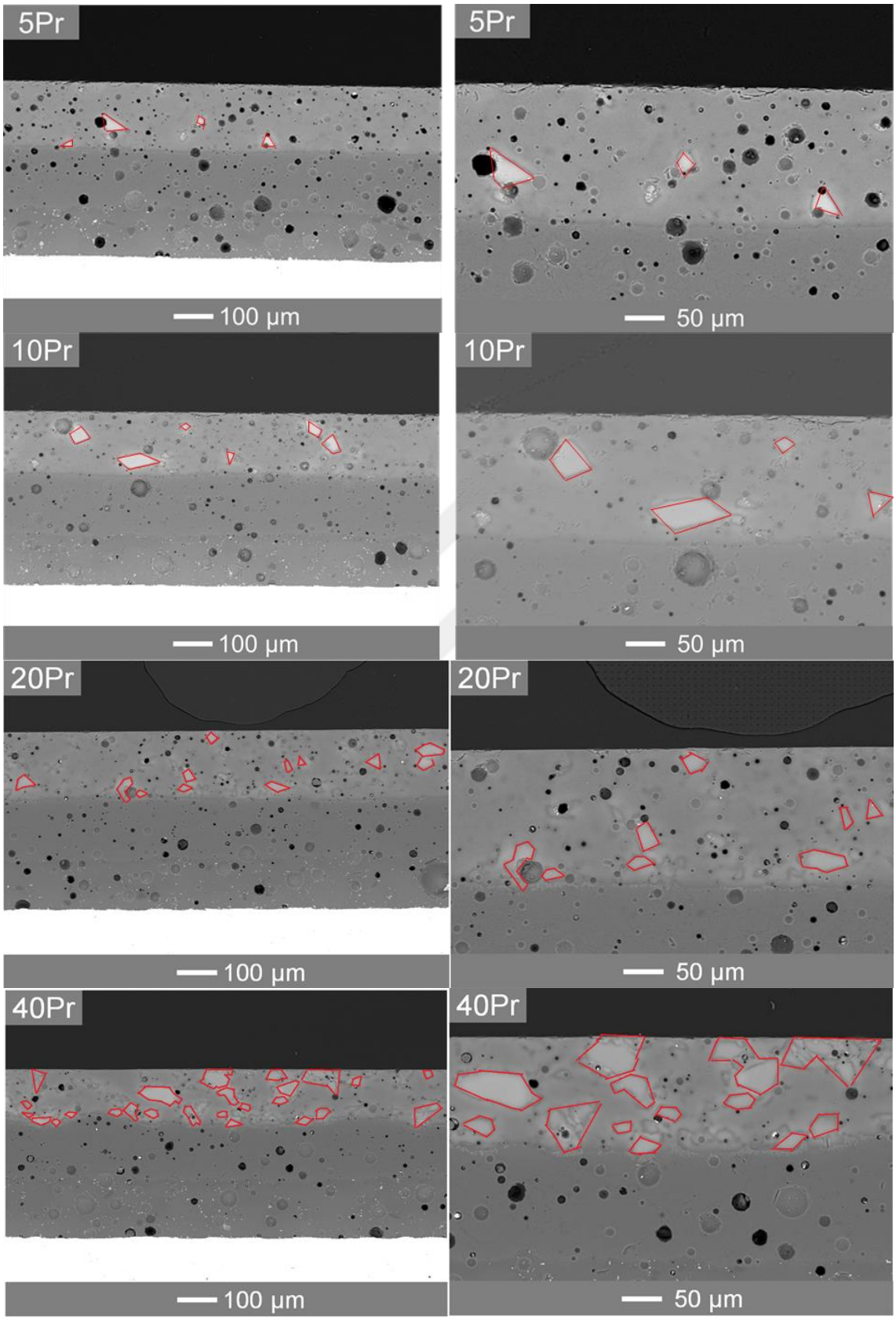


Figure 7.7 Scanning electron microscopy (SEM) images were obtained for glass-ceramic coatings containing different ratios of $SrAl_2Si_2O_8:Pr^{3+},Dy^{3+}$, with measurements taken at 100 µm and 50 µm.

The acid resistance of the samples is listed in Table 7.4 after being tested using cold citric acid on the sample surfaces in accordance with the ISO 28706-1 standard. The property of acid resistance holds significant importance and is highly coveted in glass-ceramic coatings. It is anticipated that these coatings will exhibit resistance to a range of chemical agents, including waste gases and abrasive cleaning substances, to which they will be particularly exposed in outdoor environments. Consequently, it is desirable for said coatings to exhibit elevated acid resistance. The acid resistance of the prepared sample exhibited an initial deficiency, however, an increase in the quantity of $SrAl_2Si_2O_8:Pr^{3+},Dy^{3+}$ additive resulted in an improvement of the acid resistance. The samples were subjected to visual inspection in compliance with the ISO 28706-1 standard. In the event that wear marks are detected during the visual examination, the specimens undergo a rubbed-dry procedure. The presence of acid marks on the rubbed sample is indicative of a failed acid resistance test.

Table 7.4 The result of the cold citric acid test applied to samples that is standard, 5Pr, 10Pr, 20Pr and 40Pr

Sample Code	**Level**	**Comment**
Standard sample	A	Passed
5Pr	A	Passed
10Pr	A	Passed
20Pr	A+	Passed
40Pr	A+	Passed

The visual appeal of glass-ceramic coating materials intended for outdoor applications is of paramount importance. Consequently, it is imperative to ensure a lustrous surface in the region that has been coated. In addition to the aesthetic investigation of the manufactured samples, the macro impacts of the incorporated $SrAl_2Si_2O_8:Pr^{3+},Dy^{3+}$ particles were studied in terms of gloss and surface roughness. Table 7.5 presents the gloss measurements obtained from each sample at an angle of 60°. The reference sample that (doesn't include any $SrAl_2Si_2O_8:Pr^{3+},Dy^{3+}$) particles has a glassy surface and a high

gloss value. The addition of $SrAl_2Si_2O_8:Pr^{3+},Dy^{3+}$ particles to the coating system at 5 wt% and 10 wt% did not resulted in a notable reduction in gloss value. However, SEM analysis revealed that the particles were present in low abundance on the coating surface, thereby accounting for the similarity in gloss values between the two concentrations. Compared to the other specimens, the introduction of $SrAl_2Si_2O_8:Pr^{3+},Dy^{3+}$ at 20% and 40% weight proportions in the coating formulation resulted in massive alterations in the gloss measurements. The gloss value is significantly impacted by the surface location of $SrAl_2Si_2O_8:Pr^{3+},Dy^{3+}$ particles, as evidenced by the SEM analysis. As can be understood from the result of the gloss analysis shown in Table 7.5, the addition of $SrAl_2Si_2O_8:Pr^{3+},Dy^{3+}$ to transparent glass-ceramic coatings leads to a reduction in gloss value.

Table 7.5 Gloss analysis at 60° for standard glass-ceramic coating and glass-ceramic coating doped with $SrAl_2Si_2O_8:Pr^{3+},Dy^{3+}$.

STD	**5PR**	**10PR**	**20PR**	**40PR**
96.5 GU	92.8 GU	94.2 GU	87.1 GU	56.6 GU
92.5 GU	91.3 GU	90.3 GU	83.22 GU	48.0 GU
95.2 GU	92.2 GU	90.0 GU	86.6 GU	49.9 GU

The three-dimensional surface topography maps belonging to samples were acquired through the utilization of Zeiss Smartzoom 5 devices and ConfoMAP ST 8.0 software, as depicted in Figure 7.8. Upon examination of the surface map of the standard sample (STD) not having $SrAl_2Si_2O_8:Pr^{3+},Dy^{3+}$ additives, it was noted that the green and yellow regions were uniformly dispersed. Furthermore, the number of holes and peak points was relatively limited, implying a uniform surface topography. Upon examination of the three-dimensional surface topography map of the 5Pr sample, which had been augmented with 5 wt% $SrAl_2Si_2O_8:Pr^{3+},Dy^{3+}$ in a transparent glass-ceramic system, a uniform distribution of peak points was observed. Furthermore, as evidenced by the color palette, the disparity between the maximum and minimum values is relatively minimal. Upon examination of the three-dimensional surface topography map of the 10Pr sample, which contains a 10 wt% $SrAl_2Si_2O_8:Pr^{3+},Dy^{3+}$ in a transparent glass-ceramic system, it was

noted that certain regions exhibited pit points while others displayed peak points. Upon examination of the three-dimensional surface topography map of the 20Pr sample, which had been augmented with 20 wt% $SrAl_2Si_2O_8:Pr^{3+},Dy^{3+}$ in a transparent glass-ceramic system, a uniform distribution of peak points was observed. Nevertheless, it was noted that the disparity in altitude between the summit points and the low points was greater in contrast to the aforementioned other three specimens. Upon examination of the three-dimensional surface topography map of the 40Pr sample, which contained 40 wt% $SrAl_2Si_2O_8:Pr^{3+},Dy^{3+}$ in a transparent glass-ceramic system, it was observed that this particular sample exhibited the greatest disparity in elevation between its peak and pit points. The observed increase in the ratio of $SrAl_2Si_2O_8:Pr^{3+}$, Dy^{3+} particles during SEM analysis within the glass-ceramic coating was found to be directly proportional to the increase in the number of particles on the surface. This phenomenon can be attributed to the tendency of the coating to form dense peaks and pits, as evidenced by the three-dimensional topography map.

Table 7.6 The roughness values (Ra) for the standard glass ceramic coating and the glass ceramic coating doped with $SrAl_2Si_2O_8:Pr^{3+}$, Dy^{3+}, computed using the ConfoMAP software on 3D surface topography.

STD	5PR	10PR	20PR	40PR
3.66 Ra	4.82 Ra	4.92 Ra	7.52 Ra	17.50 Ra

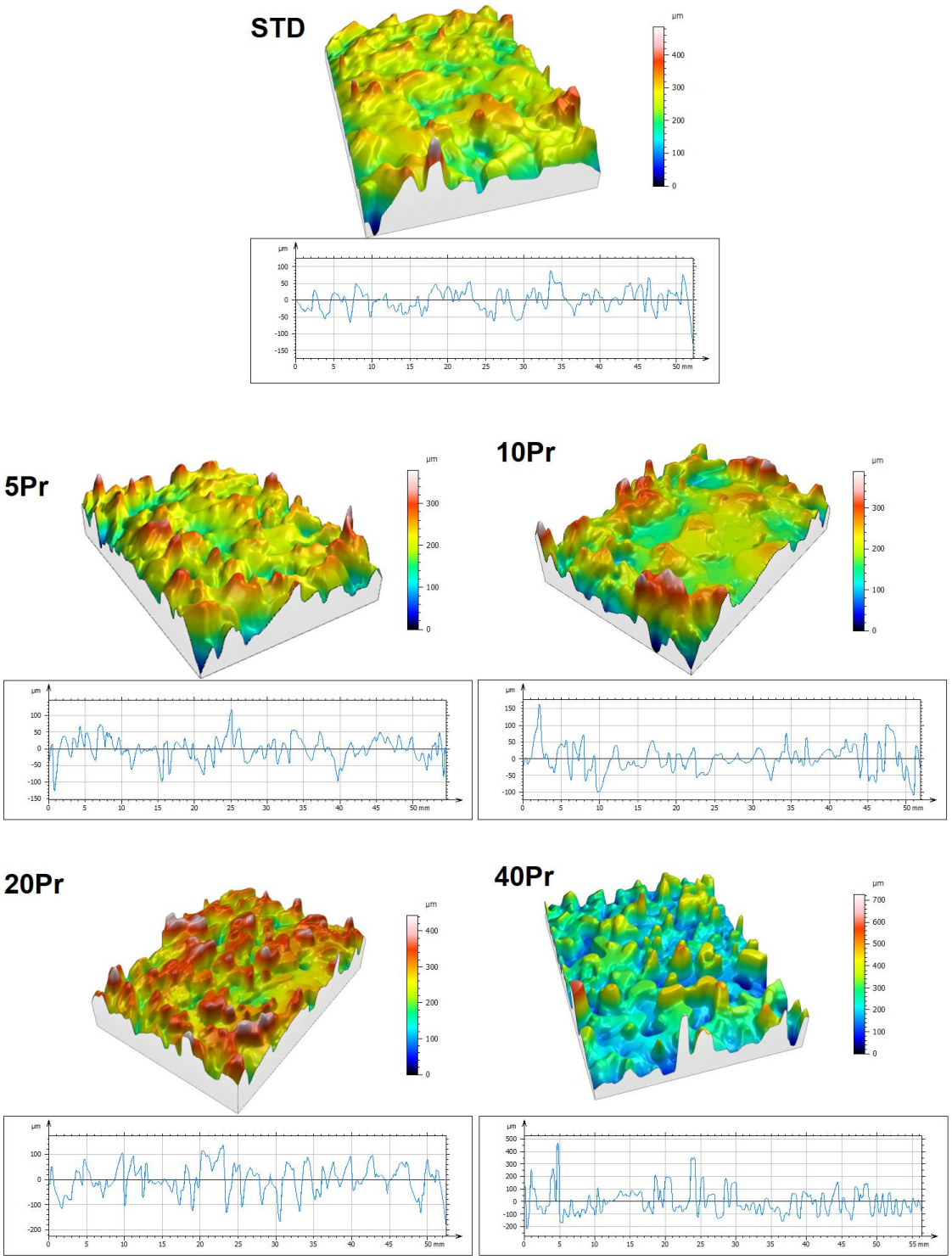


Figure 7.8 3D topography maps for standard glass ceramic coating and glass ceramic coating doped with $SrAl_2Si_2O_8:Pr^{3+}$, Dy^{3+}.

The roughness values (table 7.6) were computed in compliance with the ISO 4287 standard using the ConfoMAP ST 8.0 software, based on the 3D topography maps acquired. The glassy surface of the standard sample results in the lowest roughness value. The introduction of $SrAl_2Si_2O_8:Pr^{3+}$, Dy^{3+} particles into the coating results in the formation of micro-roughnesses within the glassy structure. The 3D topography map reveals that the augmentation of $SrAl_2Si_2O_8:Pr^{3+}$, Dy^{3+} particles on the sample surface leads to a rise in the number of peaks and valleys generated, along with the amplification of the disparity in elevation between them. This phenomenon accounts for the escalation in roughness values. The presence of micro-roughnesses induces light scattering during the process of surface roughness measurement and visual inspection. This phenomenon leads to a reduction in the gloss value of the coating, thereby imparting a matte appearance to the samples.

$SrAl_2Si_2O_8:Pr^{3+}$, Dy^{3+} was added to the transparent glass-ceramic coating recipe in various proportions (5%wt, 10%wt, 20%wt, and 40%wt) as a mill additive for the purpose of giving a luminescent property to transparent glass-ceramic coating and to find the highest emission value. The specimens were subjected to spectrofluorometric analysis following the requisite procedures. The samples' (undoped glass-ceramic coating, 5Pr, 10Pr, 10Pr and 40Pr) emission values were analyzed, and the resulting graph is presented in Figure 7.9. The spectrofluorometer analysis of the undoped transparent glass-ceramic coating did not reveal any distinct peak. However, minor alterations were detected at 575 nm upon the introduction of $SrAl_2Si_2O_8:Pr^{3+}$, Dy^{3+} into the coating system at 5%wt and 10%wt concentrations. Upon increasing the proportions of $SrAl_2Si_2O_8:Pr^{3+}$, Dy^{3+} in the coating system to 20%wt and 40%wt, a gradual increase in the peaks at 485 nm and 575 nm was observed. The observed increase in emission peaks is believed to be a result of the amplified number of emitting particles per unit area, which is directly proportional to the quantity of $SrAl_2Si_2O_8:Pr^{3+}$, Dy^{3+} present in the transparent glass-ceramic coating, as seen in the SEM analysis depicted in Figure 7.7. Additionally, when the quantity of $SrAl_2Si_2O_8:Pr^{3+}$, Dy^{3+} particles on the coated surface grows, so does the amount of $SrAl_2Si_2O_8:Pr^{3+}$, Dy^{3+} particles per unit area. Consequently, an increase in the levels of emissions has been obtained.

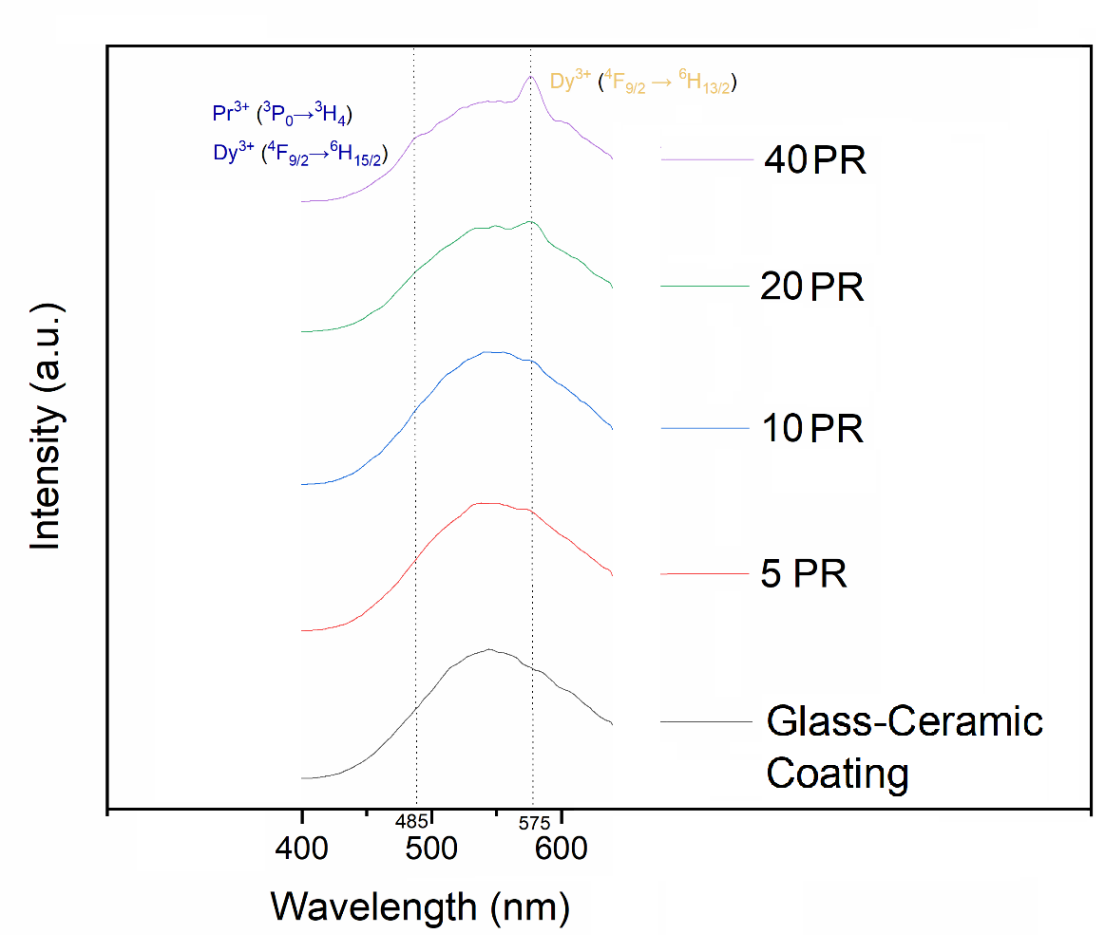


Figure 7.9 Emission graph of various proportions of $SrAl_2Si_2O_8:Pr^{3+}$, Dy^{3+} particles doped and undoped transparent glass-ceramic coating.

Figure 7.9 displays emission peaks for Pr^{3+} and Dy^{3+} ions in the visible area at various wavelengths. For both ions, the strongest peaks can be seen at 485 nm for Pr^{3+} and 575 nm for Dy^{3+} [154]. The photons released by electrons of Pr^{3+} ions via transiting from $^3P_0$ energy level to $^3H_4$ energy level are what cause to occur the peak at 480 nm wavelength, which is the characteristic emission peak of Pr^{3+} ions. The coloring of these released photons is blue. The electron of Dy^{3+} ions stimulated to the $^4F_{9/2}$ energy level by the exciter emits energy as a photon as it transitions to the $^6H_{15/2}$ energy level, creating one of the distinctive peaks of Dy^{3+} ions at 485 nm wavelength. A second distinctive emission peak connected to Dy^{3+} ions may be seen at 574 nm in wavelength. In this case, electrons stimulated to the ^{4}F9/2 energy level transfer to the $^6H_{13/2}$ energy level and release their energy as a photon. Yellowness characterizes this photon's emission in the visible spectrum [154], [155]. The dysprosium-related $^4F_{9/2} \rightarrow {}^6H_{15/2}$ transition is mostly magnetically permitted and is unaffected by the intensity of the crystal field strength the

dysprosium ion. At a wavelength of 575 nm, dysprosium also exhibits another emission peak [156], [157]. The transition from $^4F_{9/2}$ to $^6H_{13/2}$ is classified as a forced electric dipole transition and is situated in regions of low symmetry that lack an inversion centering [158]. Additionally, the $^3P_0 \rightarrow {}^3H_4$ transition that Pr^{3+} ions undergo at 485 nm is an electric dipole transition that is comparable to the actions of Dy^{3+} ions [159].

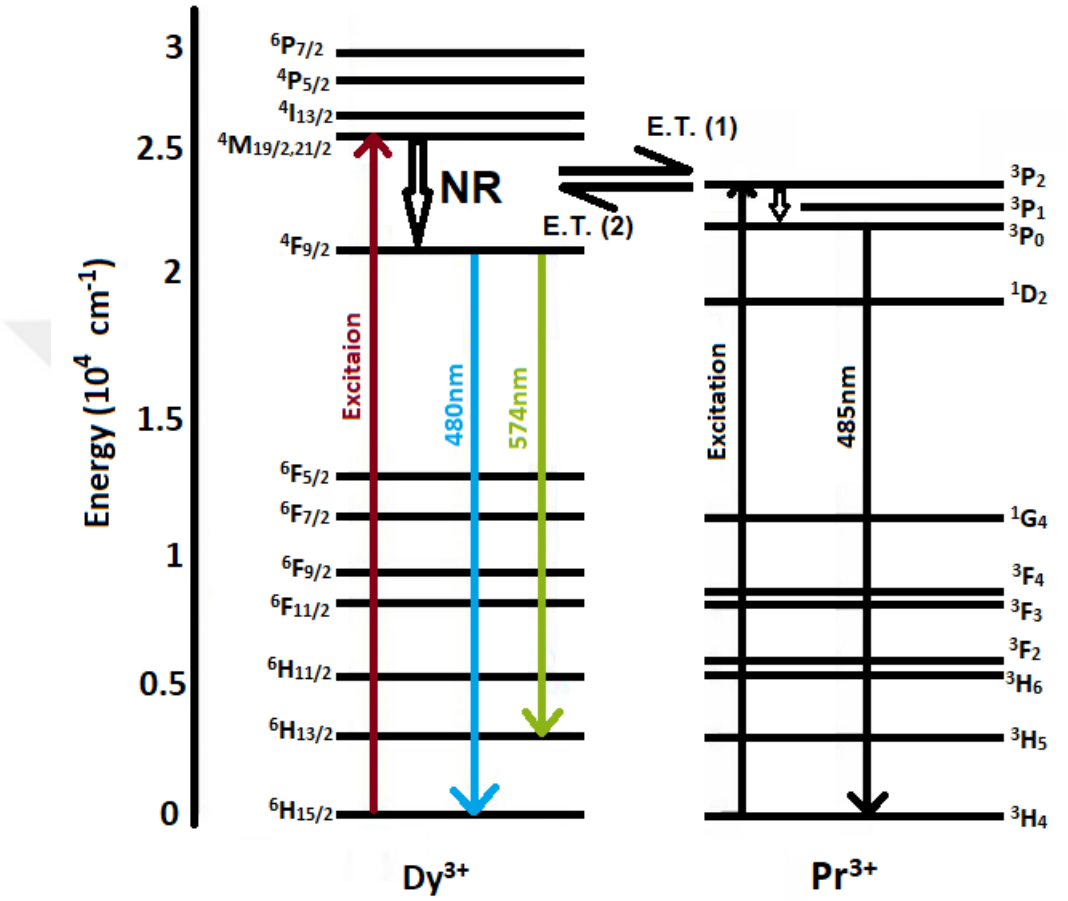


Figure 7.10 Illustration of the energy band diagrams that show the energies of Pr^{3+} and Dy^{3+}.

Figure 7.10 depicts both the activators and their energy band transitions. This diagram shows the energy band transitions that excited activator ions go through, along with the radiative or non-radiative emissions that come as a consequence. Additionally, the typical emission wavelengths of the activator ions as well as the energy transfer that takes place between them are displayed. The ground state energy level of the Dy^{3+} ion ($^6H_{15/2}$) is stimulated to higher energy levels. A non-radiative (NR) decay of the excited Dy^{3+} ion fills the $^4F_{7/2}$ energy level. According to formula 14, it is proposed that the Dy^{3+} ion transfers non-radiative energy to the Pr^{3+} ion. Finally, the Dy^{3+} emission that has been recorded is produced by the residual energy at the $^4F_{9/2}$ energy level [160].

$$Dy^{3+}[^4F_{9/2}] + Pr^{3+}[^3H_4] \rightarrow Dy^{3+}[^6H_{15/2}] + Pr^{3+}[^3P_{1,0}] \quad (14)$$

The Pr^{3+} ion experiences energy transfer in a similar manner. The energy level of the Pr^{3+} ion is stimulated from $^3H_4$, which is its ground state energy level, to $^3P_2$. The Pr^{3+} ion then proceeds through non-radiative decay, releasing energy to the $3P_1$ and $3P_0$ levels. The energy transfer from Pr^{3+} to Dy^{3+} takes place by a relaxed non-radiative emission because the energy levels are close together ($^3P_1$ for Pr^{3+} and $^4F_{9/2}$ for Dy^{3+}), as seen in formula 15. The Dy^{3+} ion is excited during these energy exchanges and emits light at 575 nm and 485 nm wavelengths [161].

$$Pr^{3+}[^3P_0] + Dy^{3+}[^6H_{15/2}] \rightarrow Pr^{3+}[^3H_4] + Dy^{3+}[^4F_{9/2}] \quad (15)$$

"Color science" is the study of how colors are assessed and measured. The most popular way for describing the three fundamental color values—known as the color-matching functions $\bar{x}(\lambda)$, $\bar{y}(\lambda)$, and $\bar{z}(\lambda)$ —that compose a color is the CIE color system [162], [163]. To create spectral hues, artificial colors—also referred to as tristimulus values—can be added. The values of these tristimulus are denoted by X, Y, and Z. The following formula may be used to represent the amount of simulation needed to identify the color of the spectral power density (P(λ)) produced from the analysis:

$$X = \int_{\lambda} \bar{x}(\lambda) P(\lambda) d\lambda \quad (16)$$

$$Y = \int_{\lambda} \bar{y}(\lambda) P(\lambda) d\lambda \quad (17)$$

$$Z = \int_{\lambda} \bar{z}(\lambda) P(\lambda) d\lambda \quad (18)$$

Knowing the amounts of at least two reference stimuli is essential in order to define colors using straightforward mathematical calculations. This is thus because x, y, and z must always equal "1" when added together [164]. Chromaticity coordinates are represented by the letters x, y, and z, which stand for the ratio of the total of the three tristimulus values (X, Y, and Z) of light :

$$x = \frac{X}{X + Y + Z} \quad (19)$$

$$y = \frac{Y}{X + Y + Z} \quad (20)$$

$$z = \frac{Z}{X + Y + Z} \quad (21)$$

In most cases, a color's x and y coordinates are utilized to define it [156]. The CIE 1931 chromaticity diagram shows the multi-chromatic wavelengths inside the diagram's region and the single-color coordinates outside the diagram's perimeter. Table 7.7 presents the chromaticity coordinates that have been calculated from the tristimulus values of the STD, 5Pr, 10Pr, 20Pr, and 40Pr samples.

Table 7.7 CIE 1931 chromaticity coordinates of $SrAl_2Si_2O_8:Pr^{3+}$, Dy^{3+} particles doped and Undoped transparent glass-ceramic coatings.

Samples\Axis	**X**	**Y**
STD	0.245	0.336
5Pr	0.246	0.334
10Pr	0.246	0.333
20Pr	0.256	0.353
40Pr	0.256	0.347

The data was acquired by using emission spectrofluorometric analysis. The CIE 1931 diagram depicted in Figure 7.11 was demonstrate all samples were situated in the blue-green region. The location of the standard sample was recognized at the midpoint of the blue and green zones on the CIE 1931 diagram. In contrast, the 5Pr and 10Pr samples were observed to exhibit a shift toward the blue-white zone. Additionally, it was observed that the samples with 20Pr and 40Pr shifted toward the regions of green and yellow. The

observed phenomenon is attributed to a rise in the quantity of $SrAl_2Si_2O_8:Pr^{3+}$, Dy^{3+} particles as evidenced by the SEM analysis depicted in Figure 7.7. The increase in the amount of $SrAl_2Si_2O_8:Pr^{3+}$, Dy^{3+} particles within the coating has been observed to yield a boost in the $^4F_{9/2} \rightarrow {}^6H_{15/2}$, $^4F_{9/2} \rightarrow {}^6H_{13/2}$, and $^3P_0 \rightarrow {}^3H_4$ energy transitions, as evidenced by the spectrofluorometer analysis depicted in Figure 7.9. The study conducted by V. Narest and N. Lee [165] demonstrated the inclusion of Dy^{3+} ions at a concentration of 1% mol in the fluoro-borosilicate glass system led to emission in the green-yellow region on the CIE color diagram. Conversely, the introduction of Pr^{3+} ions caused a shift in this emission towards the yellow region. The increase in the amount of $SrAl_2Si_2O_8:Pr^{3+}$, Dy^{3+} particles in the coating results in a rise in the emission intensity of both Dy^{3+} and Pr^{3+} ions. This explains the shift observed in Figure 7.11.

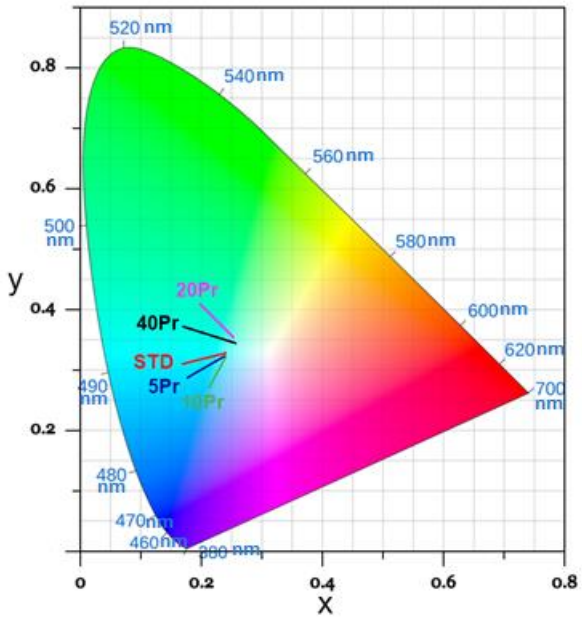


Figure 7.11 CIE 1931 chromatography diagram of glass-ceramic coatings with various proportions of $SrAl_2Si_2O_8:Pr^{3+}$, Dy^{3+}.

7.4. Characterization of Coating Samples (with added $SrAl_2Si_2O_8:Er^{3+},Dy^{3+}$)

This section involved the preparation of glass-ceramic coating samples with the objective of obtaining luminescent properties through the incorporation of $SrAl_2Si_2O_8:Er^{3+}$, Dy^{3+} additives. The coating procedures cited in section 7.1 were followed for the preparation of said samples. The metal substrate was coated with a ground coating, an intermediate coating, and a top coat that included additives of $SrAl_2Si_2O_8:Er^{3+}$, Dy^{3+}. To get it ready for the application of the following coat, each coat was fired. After being fired, the metal substrate was coated with a ground glass-ceramic coating that had a thickness of approximately 140 microns. After undergoing firing, the intermediate coating of glass-ceramic applied onto the primer coat exhibited a thickness of 160 microns. The transparent glass-ceramic coating's recipe was formulated through the incorporation of $SrAl_2Si_2O_8:Er^{3+}$, Dy^{3+} particles into the mixture. The top coat formulation was applied onto the previously prepared intermediate coating and exhibited an average thickness of 120 microns post-firing. Different amounts of $SrAl_2Si_2O_8:Er^{3+}$, Dy^{3+} particles have been incorporated into the transparent glass-ceramic coating at 5%wt, 10%wt, 20%wt, and 40%wt. The samples that were prepared have been designated as 5Er, 10Er, 20Er, and 40Er, respectively. All of the tests applied in section 7.2 were conducted on the samples that had been previously prepared. The specimens that were made ready for examination underwent analysis via SEM, as depicted in Figure 7.12. The SEM analysis displays that the transparent glass-ceramic coating contains $SrAl_2Si_2O_8:Er^{3+}$, Dy^{3+} particles, which are identified by the white areas marked with red in the images. The augmentation of the $SrAl_2Si_2O_8:Er^{3+}$, Dy^{3+} particle ratio in the formulation of the transparent glass-ceramic coating led to a corresponding rise in the quantity of $SrAl_2Si_2O_8:Er^{3+}$, Dy^{3+} particles per unit area. Moreover, an escalation in the quantity of $SrAl_2Si_2O_8:Er^{3+}$, Dy^{3+} particles attaining the coating surface was noted with the aforementioned rise in ratio.

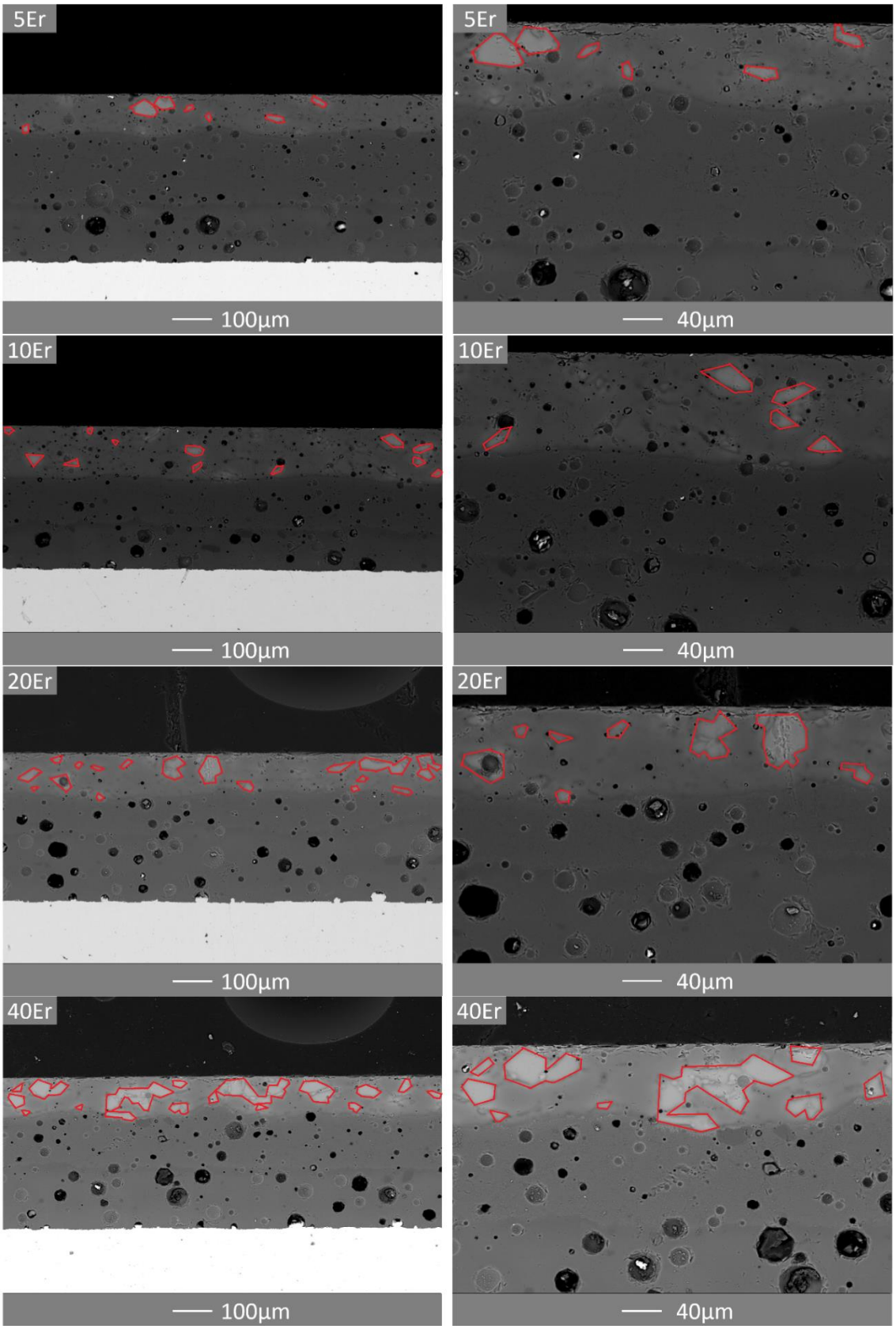


Figure 7.12 Scanning electron microscopy (SEM) images were obtained for glass-ceramic coatings containing different ratios of $SrAl_2Si_2O_8:Er^{3+}$, Dy^{3+}, with measurements taken at 100 µm and 40 µm.

The resistance of the prepared glass-ceramic coatings to weak acids was evaluated using experiments that followed the ISO 28706-1 standard. In accordance with the ISO 28706-1 standard, the glass-ceramic coating surface was subjected to a solution of cold citric acid, and the outcomes have been reported in Table 7.8.

Table 7.8 The result of the cold citric acid test applied to samples that is standard, 5Er, 10Er, 20Er, 40Er.

Sample Code	**Level**	**Comment**
Standard sample	A	Passed
5Er	A	Passed
10Er	A	Passed
20Er	A+	Passed
40Er	A+	Passed

The significance of resistance to weak acids is paramount in the context of glass-ceramic coating applications. It is anticipated that coatings that are subjected to outdoor conditions will exhibit resistance to exhaust gases, abrasive cleaning agents, and diverse pollutants. Consequently, it is anticipated that the coatings employed will exhibit acid resistance. The samples were subjected to visual examination as per the ISO 28706-1 standard. In the event that wear marks are observed on the surface of the coating during the visual examination, the specimens undergo a rubbed-dry treatment. The observation of acid marks on the tested sample is indicative of the unsuccessful outcome of the acid resistance examination. The acceptability of the acid resistance of the standard sample that was prepared has been determined. The introduction of $SrAl_2Si_2O_8:Er^{3+}$, Dy^{3+} particles into the system resulted in an enhancement of acid resistance, as evidenced by the observed improvement.

The aesthetic quality of materials developed for all visible surfaces, including outdoor, holds significant meaning. Consequently, the presence of a glossy surface is a crucial

factor in regions where the application of a coating is intended. The study conducted an analysis of the macro effects of $SrAl_2Si_2O_8:Er^{3+}$, Dy^{3+} particles on the coating surface with regards to gloss and surface roughness, in addition to examining the aesthetic properties of the obtained samples. Table 7.9 presents the gloss measurements obtained at an angle of 60° for the analyzed samples.

Table 7.9 Gloss analysis at 60° for standard glass-ceramic coating and glass-ceramic coating doped with $SrAl_2Si_2O_8:Er^{3+}$, Dy^{3+}.

STD	5Er	10Er	20Er	40Er
92.6 GU	91.6 GU	91.8 GU	89.0 GU	66.1 GU
97.4 GU	93.1 GU	91.3 GU	89.7 GU	57.0 GU
95.3 GU	93.6 GU	91.6 GU	87.4 GU	70.3 GU

The gloss value of the standard sample, devoid of $SrAl_2Si_2O_8:Er^{3+}$,Dy^{3+} particles, is attributed to its homogeneous vitrified surface. The incorporation of $SrAl_2Si_2O_8:Er^{3+}$, Dy^{3+} particles into the coating formulation at 5%wt and 10%wt did not result in a huge alteration of the gloss measurements of the specimens. The limited presence of $SrAl_2Si_2O_8:Er^{3+}$, Dy^{3+} particles on the surface of the coating, as evidenced by SEM examination, accounts for the minor alteration in the gloss measurements. A notable difference in the glossiness measurements of the coatings was detected upon the inclusion of $SrAl_2Si_2O_8:Er^{3+}$, Dy^{3+} particles at 20% and 40% weight proportions in the coating formulation, as opposed to the aforementioned other samples. The SEM analysis reveals that the presence of $SrAl_2Si_2O_8:Er^{3+}$, Dy^{3+} particles on the surface has a notable impact on the glossiness value. The results presented in Table 16 indicate that an increase in the ratio of $SrAl_2Si_2O_8:Er^{3+}$, Dy^{3+} particles in the coating is associated with a reduction in glossiness value.

Figure 7.13 displays the three-dimensional topography maps of the specimens. The acquisition of three-dimensional maps was utilized by the Zeiss Smartzoom 5 optical microscope. Maps were subsequently subjected to detailed analysis through the utilization of ConfoMAP ST 8.0 software. Upon examination of the three-dimensional

surface map of the standard sample (STD) lacking $SrAl_2Si_2O_8:Er^{3+}$, Dy^{3+} particles, it was observed that the mean elevations depicted in the yellow and green hues were uniformly dispersed. Furthermore, the limited display of red/white high points and blue low points suggests a uniform surface. In the transparent glass-ceramic formulation, 5%wt $SrAl_2Si_2O_8:Er^{3+}$, Dy^{3+} was added to create the 5Er sample. When the three-dimensional surface topography of the 5Er sample was analyzed, a slight increase in the red and white peak points—which signify the highest points—was seen in comparison to the standard sample. The addition of 10% $SrAl_2Si_2O_8:Er^{3+}$, Dy^{3+} particles to the transparent glass-ceramic coating recipe resulted in an observable increase in the number of white and red peak points, as evidenced by the three-dimensional surface topography of the 10Er sample. An increase in the number of blue deep points and red and white peak points were observed in the three-dimensional surface topography of the 20Pr sample when the weight percentage of $SrAl_2Si_2O_8:Er^{3+}$, Dy^{3+} particles added was increased to 20%. The addition of 40% $SrAl_2Si_2O_8:Er^{3+}$, Dy^{3+} particles to the transparent glass-ceramic coating resulted in the highest level of increase in the number of red and white peak points, as evidenced by the three-dimensional surface map. The SEM analysis conducted on the cross-section of transparent glass-ceramic coating suggests a correlation between the observed increases in $SrAl_2Si_2O_8:Er^{3+}$, Dy^{3+} particles and the corresponding increase in peaks and depth on the surface.

Table 7.10 The roughness values for the standard glass ceramic coating and the glass ceramic coating doped with $SrAl_2Si_2O_8:Er^{3+}$, Dy^{3+} , computed using the ConfoMAP software on 3D surface topography.

STD	**5PR**	**10PR**	**20PR**	**40PR**
3.66 Ra	3.72 Ra	6.24 Ra	8.46 Ra	11.91 Ra

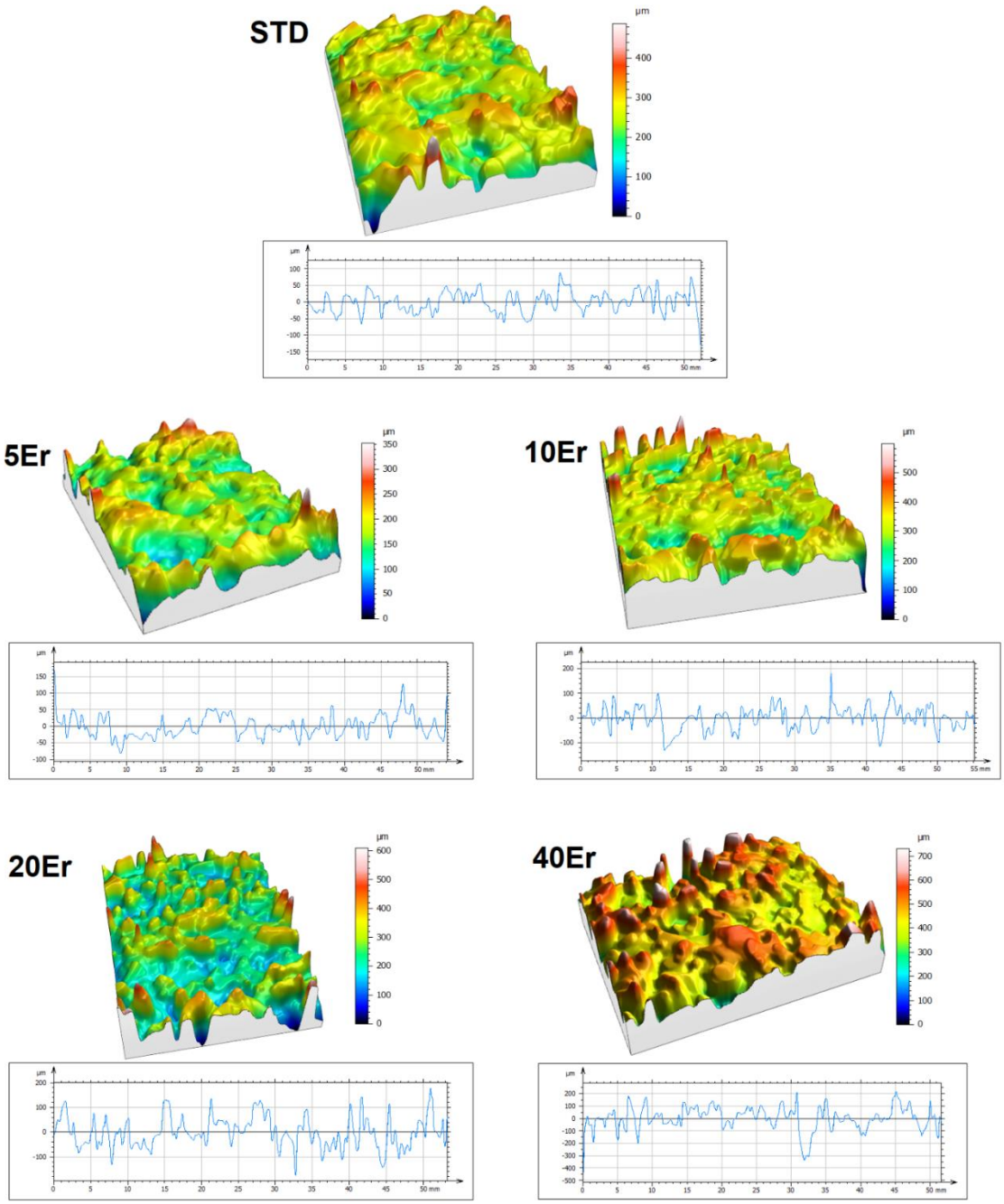


Figure 7.13 3D topography maps for standard glass ceramic coating and glass ceramic coating doped with $SrAl_2Si_2O_8:Er^{3+}$, Dy^{3+}.

The topographical maps in three dimensions were subjected to a detailed analysis utilizing the ConfoMAP software. The ConfoMAP software computed surface roughness in compliance with the ISO 4287 guidelines. The standard sample yielded the minimum surface roughness value as per the calculation. The inclusion of $SrAl_2Si_2O_8:Er^{3+}$, Dy^{3+} particles in the coating formulation results in the development of micro-roughness on the surface. The empirical evidence derived from the three-dimensional surface topography map indicates a positive correlation between the quantity of $SrAl_2Si_2O_8:Er^{3+}$, Dy^{3+} particles present on the sample surface and the number of peaks and valleys observed on said surface. Furthermore, it is evident from the elevation scale depicted alongside the 3D maps that the disparity in altitude between the peak and valley locations escalates upon the introduction of $SrAl_2Si_2O_8:Er^{3+}$, Dy^{3+} particles into the system. The rise in the quantity of peaks and valleys on the surface of the sample, along with the corresponding increase in the disparity of their heights, elucidates the escalation in the roughness measurements presented in Table 7.10. The presence of micro-roughnesses on the surface of the samples results in non-uniform scattering of incident light. The occurrence of this phenomenon results in a reduction in the coating's gloss values.

The incorporation of $SrAl_2Si_2O_8:Er^{3+}$, Dy^{3+} particles in different ratios was carried out in a transparent glass-ceramic coating formulation to confer luminescent characteristics to the glass-ceramic coating. In order to determine the most effective emission value, particles of $SrAl_2Si_2O_8:Er^{3+}$, Dy^{3+} were incorporated into a transparent glass-ceramic coating at varying weight percentages of 5%, 10%, 20%, and 40%. The samples were subjected to spectrofluorometric analysis in accordance with the requisite protocols. Figure 7.14 depicts the emission graph resulting from the spectrofluorometer analysis conducted on various samples, namely the bare glass-ceramic coating, 5Er, 10Er, 20Er, and 40Er.

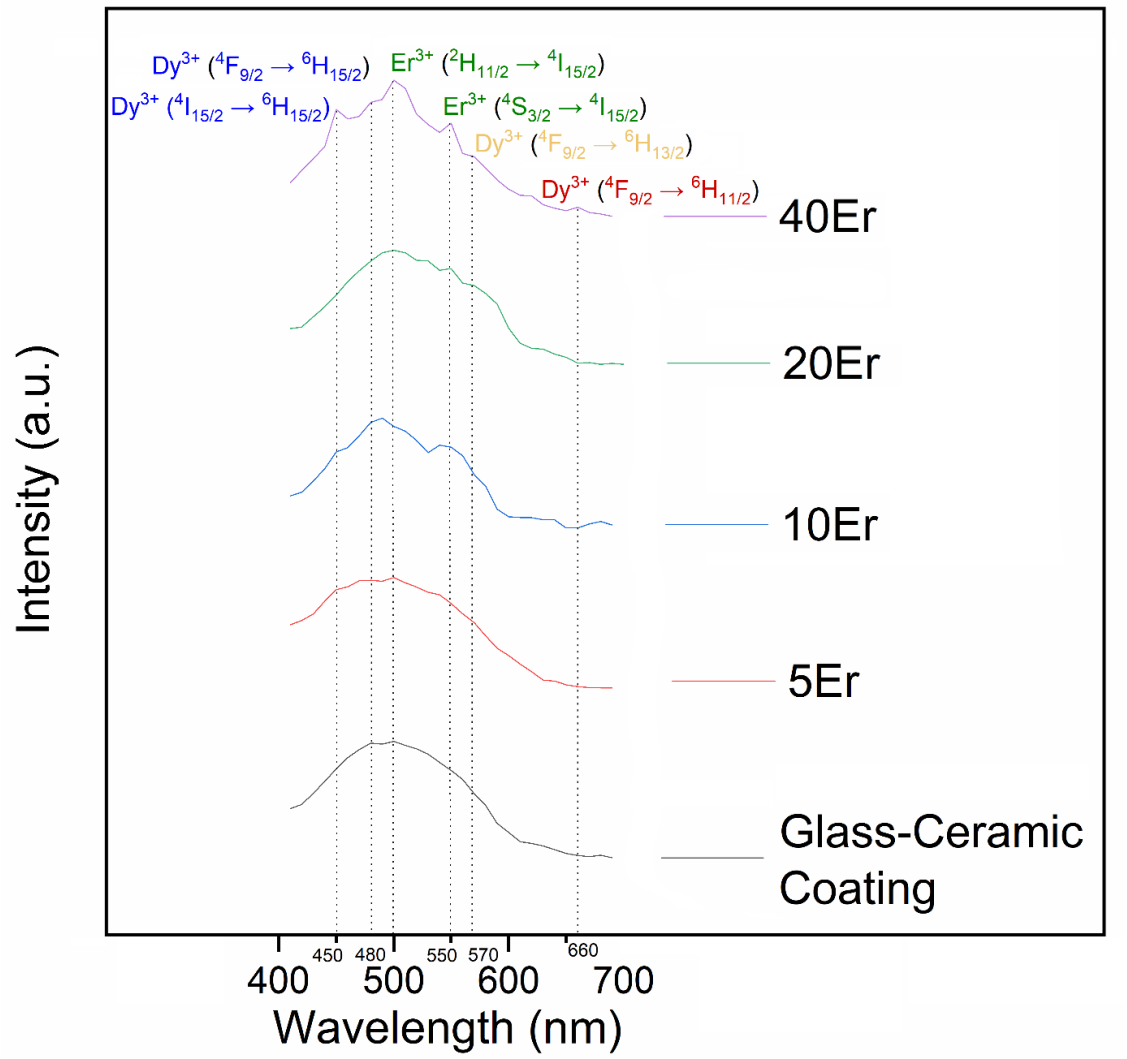


Figure 7.14 Emission graph of various proportions of $SrAl_2Si_2O_8:Er^{3+}$, Dy^{3+} particles doped and undoped transparent glass-ceramic coating.

The analysis of the bare transparent glass-ceramic coating (STD) and 5Pr samples did not yield any significant peak. Upon addition of 10%wt $SrAl_2Si_2O_8:Er^{3+}$, Dy^{3+} particles to the coating system, minor peaks were detected at wavelengths of 450nm and 550nm. Upon increasing the quantity of $SrAl_2Si_2O_8:Er^{3+}$, Dy^{3+} particles incorporated into the coating to 20%wt, the emergence of minor shoulders at wavelengths of 500nm, 550nm, and 570nm was observed. Upon increasing the concentration of $SrAl_2Si_2O_8:Er^{3+}$, Dy^{3+} in the coating to 40%wt, emissions were detected at wavelengths of 450 nm, 480 nm, 500 nm, 550nm, 570 nm, and 660 nm. The Dy^{3+} ions have the high-intensity characteristic peak observed at a wavelength of 450 nm, as well as the characteristic peaks in the form of shoulders observed at wavelengths of 480 nm, 570 m, and 660 nm[166]–[169]. Furthermore, the

peak of high intensity at a wavelength of 500 nm and the peaks that are observed in the form of minor shoulders at wavelengths of 550 nm belong to Erbium ions. The observed augmentation in the emission peaks is hypothesized to be attributable to a rise in the quantity of particles per unit area. This quantity is directly proportional to the quantity of $SrAl_2Si_2O_8:Er^{3+}$, Dy^{3+} present in the transparent glass-ceramic coating, as evidenced by SEM analysis. Moreover, the augmentation in the quantity of $SrAl_2Si_2O_8:Er^{3+}$, Dy^{3+} present in the coating has resulted in a rise in the number of $SrAl_2Si_2O_8:Er^{3+}$, Dy^{3+} particles on the surface, as evidenced by the three-dimensional topographical examination. Thus, it is hypothesized that the coating-induced losses have diminished, resulting in a rise in the emission levels.

Figure 7.14 displays the emission peak locations for Er^{3+} and Dy^{3+} ions at different visible wavelengths. Two major peaks at 450 nm and 500 nm wavelengths may be detected while analyzing the graph. Dy^{3+} and Er^{3+} ions are responsible for the distinctive peaks at 450 and 500 nm, respectively. At the main peak of 500 nm wavelength for Er^{3+} ions, green color photons are produced by electrons of Er^{3+} ions shifting from the $^2H_{11/2}$ energy level to the $^4I_{15/2}$ energy level. The peak shown at 550 nm wavelength in the emission graph is also caused by photons released by electrons associated with Er^{3+} ions moving from the $^4S_{3/2}$ energy level to the $^4I_{15/2}$ energy level. Green photons produce this peak at a wavelength of 550 nm [166], [167]. At 450 nm, photons released as a result of electrons shifting from the $^4I_{15/2}$ energy level to the $^6H_{15/2}$ energy level form the distinctive peak produced by Dy^{3+} ions. The photons with a wavelength of 450 nm that produce this peak are blue. A blue photon is generated as a consequence of electrons moving from the $^4F_{9/2}$ energy level to the $^6H_{15/2}$ energy level, creating the emission peak produced by Dy^{3+} ions at 480 nm. Additionally, yellow-colored photons released as a result of electrons changing from the $^4F_{9/2}$ energy level to the $^6H_{13/2}$ energy level contribute to the emission peak for Dy^{3+} ions at 570 nm in wavelength. Last but not least, red-colored photons emitted by electrons transferring between the $^4F_{9/2}$ energy level and the $^6H_{11/2}$ energy level are what generate the emission peak for Dy^{3+} ions at 660 nm in wavelength [168], [169].

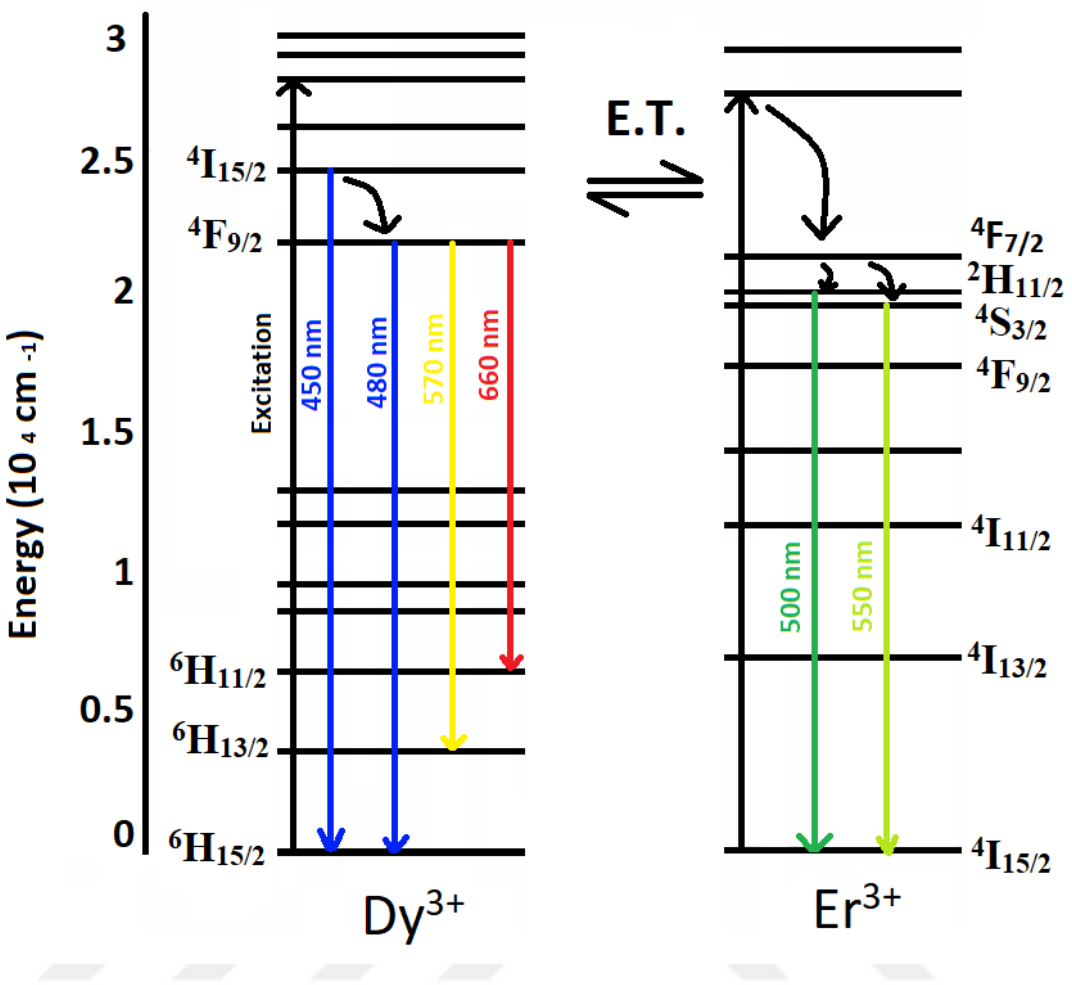


Figure 7.15 Illustration of the energy band diagrams that show the energies of Er^{3+} and Dy^{3+}.

The explanation of the emission bands observed in the visible region is elucidated by reference to the energy level diagram depicted in Figure 7.15. At first, the Er^{3+} ion undergoes non-radiative relaxation to attain the $^4F_{7/2}$ energy state. Following the relaxation process, the $^4F_{7/2}$ energy band undergoes rapid and non-radiative relaxation to the adjacent $^2H_{11/2}$ and $^4S_{3/2}$ energy bands, owing to their close energy difference. The aforementioned procedure results in the generation of emissions with wavelengths of 500 nm ($^2H_{11/2} \rightarrow {}^4I_{15/2}$) and 550 nm ($^4S_{3/2} \rightarrow {}^4I_{15/2}$), which are green in color. Simultaneously, the Dy^{3+} ion undergoes excitation to a higher energy state relative to the Er^{3+} ion. Following the aforementioned stimulation, the Dy^{3+} ion undergoes nonradiative relaxation, resulting in its transition to the $^4I_{15/2}$ and $^4F_{9/2}$ excited states. Emissions are observed at specific wavelengths, namely 450 nm ($^4I_{15/2} \rightarrow {}^6H_{15/2}$) and 480 nm ($^4F_{9/2} \rightarrow {}^6H_{15/2}$) for the color blue, 570 nm ($^4F_{9/2} \rightarrow {}^6H_{13/2}$) for the color yellow, and 660 nm ($^4F_{9/2}$ - $^6H_{11/2}$) for the color red. The minimal energy difference between the energy band

transitions of Er^{3+} ($^4F_{7/2}$) $\rightarrow$$^4I_{15/2}$ and Dy^{3+} ($^4F_{9/2}$ $\rightarrow$$^6H_{15/2}$) facilitates the transfer of energy between Er^{3+} and Dy^{3+} ions, resulting in a facile process. Upon excitation of the Er^{3+} ion to the $^4F_{7/2}$ energy band, energy is transferred to the adjacent Dy^{3+} ion, causing it to transition to the $^4F_{9/2}$ level. It is thought that this particular process enhances the magnitude of the emissions produced by the Dy^{3+} ion [170].

The CIE color system employs a triplet of basic color values to generate a color, as elucidated in section 7.3. The values of the main colors are established through the utilization of color-matching functions, namely $\bar{x}(\lambda)$, $\bar{y}(\lambda)$, and $\bar{z}(\lambda)$. The generation of spectral colors necessitates the use of Tristimulus values, which are represented by X, Y, and Z. The determination of expressed values is accomplished through the utilization of the subsequent formulas, wherein (P(λ)) denotes the spectral power density.

$$X = \int_{\lambda} \bar{x}(\lambda) P(\lambda) d\lambda \quad (22)$$

$$Y = \int_{\lambda} \bar{y}(\lambda) P(\lambda) d\lambda \quad (23)$$

$$Z = \int_{\lambda} \bar{z}(\lambda) P(\lambda) d\lambda \quad (24)$$

In order to provide a mathematical description of colors, it is necessary to have knowledge of at least two reference values. The reason for this is that the total of x, y, and z is required to be equivalent to the numerical value of "1". The tristimulus values of light, namely x, y, and z, serve as the representation for color coordinates.

$$x = \frac{X}{X + Y + Z} \quad (25)$$

$$y = \frac{Y}{X + Y + Z} \quad (26)$$

$$z = \frac{Z}{X + Y + Z} \quad (27)$$

Color is commonly described using x and y coordinates in CIE 1931 color system. The chromaticity coordinates derived from the tristimulus values of the samples (STD, 5Er, 10Er, 20Er, and 40Er) are presented in Table 7.11.

Table 7.11 CIE 1931 chromaticity coordinates of $SrAl_2Si_2O_8:Er^{3+}$, Dy^{3+} particles doped and undoped transparent glass-ceramic coatings.

Samples\Axis	X	Y
STD	0.245	0.336
5Er	0.249	0.350
10Er	0.246	0.344
20Er	0.241	0.327
40Er	0.240	0.322

The data obtained were produced utilizing an emission spectrofluorometer. Figure 7.16 illustrates the CIE 1931 diagram, which reveals that all specimens are situated within the range of the blue and green regions. According to the CIE 1931 diagram, the STD sample is situated at the middle between the blue and green regions. The samples of 5Er and 10Er exhibit a shift towards the green region in comparison to the STD sample, as per observation. In contrast, the samples including 20%wt and 40%wt $SrAl_2Si_2O_8:Er^{3+}$, Dy^{3+} exhibit a blue/purple shift in comparison to the standard sample. The observed shift of the 20Er and 40Er samples towards the blue/purple region is attributed to the blue emission of $SrAl_2Si_2O_8:Er^{3+}$, Dy^{3+} particles present in the samples, as evidenced by SEM analysis.

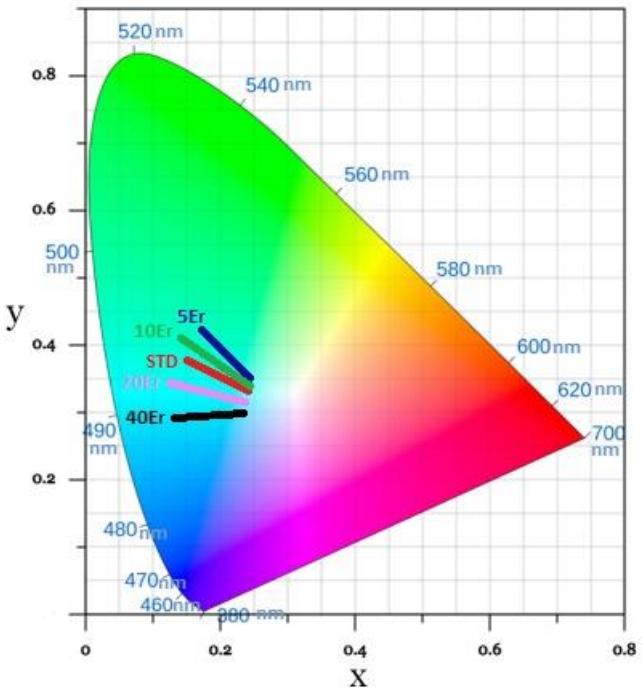


Figure 7.16 CIE 1931 chromatography diagram of glass-ceramic coatings with various proportions of $SrAl_2Si_2O_8:Er^{3+}$, Dy^{3+}.

7.5. Comparison of The Photoluminescent Characteristics of $SrAl_2Si_2O_8:Pr^{3+}$, Dy^{3+} and $SrAl_2Si_2O_8:Er^{3+}$, Dy^{3+} Doped Coatings

In studies carried out, the luminescent characteristics of Pr^{3+}/Dy^{3+} and Er^{3+}/Dy^{3+} co-doped specimens within a glass-ceramic system were investigated. The specimens were incorporated in predetermined proportions into a transparent glass-ceramic coating with identical composition. The findings of this study indicate that there was no statistically significant disparity observed between the standard sample and the samples that were doped with 5%wt and 10%wt in the transparent coating. This was observed in both studies that involved $SrAl_2Si_2O_8:Pr^{3+}$, Dy^{3+} and $SrAl_2Si_2O_8:Er^{3+}$, Dy^{3+}. The addition of particles at a ratio of 20%wt to the transparent coating resulted in the emergence of distinct characteristic peaks at a wavelength of 575 nm for $SrAl_2Si_2O_8:Pr^{3+}$, Dy^{3+}, and at wavelengths of 500 nm and 550 nm for $SrAl_2Si_2O_8:Er^{3+}$, Dy^{3+}. Additionally, it was noted that the introduction of said particles at a proportion of 40%wt to the transparent glass-ceramic coating resulted in the attainment of the maximum emission levels for both trials. The $SrAl_2Si_2O_8:Pr^{3+}$, Dy^{3+} and $SrAl_2Si_2O_8:Er^{3+}$, Dy^{3+} particles, added in equal

proportions to the transparent glass-ceramic coating, exhibited similar behaviors and provided the strongest emission values at the highest doping ratios.

It has been shown that more emission peaks develop in the $SrAl_2Si_2O_8$ system when Er^{3+} ions are introduced with Dy^{3+} instead of Pr^{3+} ions. For these samples, both Er^{3+} ions have shown more number of emission compared to Pr^{3+} ions, and also Dy^{3+} ions emit more emission in the $SrAl_2Si_2O_8$:Er^{3+}, Dy^{3+} doped coating than in the $SrAl_2Si_2O_8$:Pr^{3+}, Dy^{3+} doped coating. This is thought to be because there is a higher energy transfer from Er^{3+} to Dy^{3+} than from Pr^{3+} to Dy^{3+}. The $SrAl_2Si_2O_8$:Er^{3+}, Dy^{3+} doped coating exhibits emissions at 450 nm and 660 nm wavelengths that are not seen in the $SrAl_2Si_2O_8$:Pr^{3+}, Dy^{3+} doped coating as a consequence of this energy transfer.

The CIE chromaticity diagram depicts the standard sample situated at the center of the blue-green region. The coating sample doped with $SrAl_2Si_2O_8$: Pr^{3+}, Dy^{3+} exhibits a prominent emission peak at 575 nm, leading to a noticeable shift towards the green-yellow region in the CIE chromaticity diagram. This shift becomes more pronounced with an increase in the concentration of $SrAl_2Si_2O_8$: Pr^{3+}, Dy^{3+} particles in the coating. The $SrAl_2Si_2O_8$: Er^{3+}, Dy^{3+} doped coating samples exhibit notable emissions at three distinct peaks, characterized by strong intensities and located at wavelengths of 450 nm, 500 nm, and 550 nm. The CIE chromaticity diagram exhibits a noticeable shift towards the blue-purple region as the quantity of $SrAl_2Si_2O_8$: Er^{3+}, Dy^{3+} particles incorporated into the coating increases, owing to the prevalence of emission peaks in the blue spectrum and the impact of peaks in the yellow-red spectrum.

CONCLUSIONS

In order to deliver glass-ceramic coatings luminous qualities, this work has produced the following key findings: i) $SrAl_2Si_2O_8:Pr^{3+}$, Dy^{3+} and $SrAl_2Si_2O_8:Er^{3+}$, Dy^{3+} glass-ceramic systems obtained by using various rare earth elements (erbium, praseodymium and dysprosium) give luminescence feature to glass-ceramic coatings by revealing emission in glass-ceramic coating. ii) The weak acid resistance feature of the glass-ceramic coating systems is improved by the strong chemical resistance of these $SrAl_2Si_2O_8:Pr^{3+}$, Dy^{3+} and $SrAl_2Si_2O_8:Er^{3+}$, Dy^{3+} particles. iii) The smooth surface of the coating has been disrupted by the $SrAl_2Si_2O_8:Pr^{3+}$, Dy^{3+} and $SrAl_2Si_2O_8:Er^{3+}$, Dy^{3+} particles, which preserve their form without degrading within the glass-ceramic coating. A matte coating surface has been achieved as a consequence.

After coating the metal substrate with a ground and intermediate coat of transparent glass-ceramic coating, luminescent glass-ceramic coatings were created by adding $SrAl_2Si_2O_8:Pr^{3+}$, Dy^{3+} and $SrAl_2Si_2O_8:Er^{3+}$, Dy^{3+} particles in ratios of 5%wt, 10%wt, 20%wt, and 40%wt to the transparent glass-ceramic coating recipe. The acquired samples were subjected to spectrofluorometer examination to determine emission levels and CIE 1931 color coordinates.

The Pr^{3+}:$^3P_0{}^3 \rightarrow H_4$, Dy^{3+}:$^4F_{9/2} \rightarrow {}^6H_{15/2}$, and Dy^{3+}:$^4F_{9/2} \rightarrow {}^6H_{15/2}$ energy band transitions at 485 nm and 575 nm caused the $SrAl_2Si_2O_8:Pr^{3+}$,Dy^{3+} doped transparent glass-ceramic coatings to generate blue and yellow emissions, respectively. As the amount of $SrAl_2Si_2O_8:Pr^{3+}$,Dy^{3+} particles added to the un-doped coating recipe increased, a shift towards the green-yellow region was observed on the CIE 1931 color diagram, which is located in the middle of the green and blue regions. Transparent glass-ceramic coatings doped with $SrAl_2Si_2O_8:Er^{3+}$, Dy^{3+} have been observed to emissions in the blue, yellow, and red regions. These emissions are attributed to energy band transitions occurring at wavelengths of 450 nm, 480 nm, 500 nm, 550 nm, 570 nm, and 660 nm, respectively. This energy band transitions are Dy^{3+}:$^4I15/2 \rightarrow {}^6H15/2$, Dy^{3+}:$^4F9/2 \rightarrow {}^6H15/2$, Er^{3+}:$^2H_{11/2} \rightarrow {}^4I_{15/2}$, Er^{3+}:$^4S_{3/2} \rightarrow {}^4I_{15/2}$, Dy^{3+}:$^4F_{9/2} \rightarrow {}^6H_{13/2}$, and Dy^{3+}:$^4F_{9/2} \rightarrow {}^6H_{11/2}$. Incorporation of $SrAl_2Si_2O_8:Er^{3+}$, Dy^{3+} particles into the coating formulation has resulted in a discernible deviation towards the blue-violet spectrum relative to the unaltered coating, as evidenced by the CIE 1931 color chart.

The findings of the spectrophotometer analysis indicate that there is a positive correlation between the quantity of $SrAl_2Si_2O_8:Pr^{3+}$, Dy^{3+} and $SrAl_2Si_2O_8:Er^{3+}$, Dy^{3+}particles added to the transparent glass-ceramic coating and the observed increase in emission intensities. The observed phenomenon can be attributed to the rise in particle density per unit area as revealed by the SEM analysis, which is directly proportional to the quantity of $SrAl_2Si_2O_8:Pr^{3+}$, Dy^{3+} and $SrAl_2Si_2O_8:Er^{3+}$, Dy^{3+} particles incorporated into the coating formulation. The observed shifts in the CIE 1931 color diagram can be attributed to the heightened emission intensities.

The $SrAl_2Si_2O_8$ glass-ceramic system has been known to exhibit resistance to weak acids. The ISO 28706-1 standard has reported that the incorporation of $SrAl_2Si_2O_8$ into the glass-ceramic coating has resulted in an enhancement of the coating's ability to withstand cold citric acid, with an increase in the doping ratio.

The scanning electron microscopy analysis reveals that the addition of $SrAl_2Si_2O_8:Pr^{3+}$, Dy^{3+} and $SrAl_2Si_2O_8:Er^{3+}$, Dy^{3+} particles to the coating formulation results in an augmented particle density per unit area, thereby inducing macro-roughness on the surface of the coating. The diminution in luminosity values ascertained from the sample surfaces can be accounted for by the macro-surface roughness evident in the three-dimensional surface topography maps.

As a consequence, this study has established that glass-ceramic coatings possess the capability of self-illumination after being excited and have conferred luminescent characteristics to glass-ceramic coatings.

REFERENCES

[1] L. Ozawa, *Cathodoluminescence and photoluminescence: theories and practical applications*, vol. 2. CRC Press, 2018.

[2] E. N. Harvey, *A history of luminescence from the earliest times until 1900*. Philadelphia: American Philosophical Society, 1957.

[3] S. Shionoya, W. M. Yen, and H. Yamamoto, Eds., *Phosphor Handbook*. CRC Press, 2018.

[4] M. F. Emen, "Silikat ve Aluminat Bazlı Yeni Işıldarların Hazırlanması ve Karakterizasyonu." Doktora Tezi, Mersin Üniversitesi Fen Bilimleri Enstitüsü, 2009.

[5] P. Lenard, F. Schmidt, R. Tomaschek, and A. Becker, *Phosphoreszenz und fluoreszenz...*, vol. 23. Akademische verlagsgesellschaft mbh, 1948.

[6] H. G. Jenkins, A. H. McKeag, and P. W. Ranby, "Alkaline Earth Halophosphates and Related Phosphors," *J. Electrochem. Soc.*, vol. 96, no. 1, p. 1, 1949, doi: 10.1149/1.2776766.

[7] W. M. Yen, S. S. (Deceased), and H. Yamamoto, "Phosphor Handbook (Second Edition)," *CRC Press*, 2007. https://www.gettextbooks.jp/isbn/9780849335648/ (accessed Oct. 17, 2020).

[8] T. Matsuzawa, Y. Aoki, N. Takeuchi, and Y. Murayama, "A New Long Phosphorescent Phosphor with High Brightness, $SrAl_2O_4$: Eu^{2+}, Dy^{3+}," *J. Electrochem. Soc.*, vol. 143, no. 8, pp. 2670–2673, Aug. 1996, doi: 10.1149/1.1837067.

[9] R. Chen and D. J. Lockwood, "Developments in Luminescence and Display Materials Over the Last 100 Years as Reflected in Electrochemical Society Publications," *J. Electrochem. Soc.*, vol. 149, no. 9, p. S69, 2002, doi: 10.1149/1.1502258.

[10] Y. Lin, Z. Tang, Z. Zhang, X. Wang, and J. Zhang, "Preparation of a new long afterglow blue-emitting $Sr_2MgSi_2O_7$-based photoluminescent phosphor," *J. Mater. Sci. Lett.*, vol. 20, no. 16, pp. 1505–1506, Aug. 2001, doi: 10.1023/A:1017930630889.

[11] B. Yuan *et al.*, "Tunable color and energy transfer in single-phase white-emitting $Ca_{20}Al_{26}Mg_3Si_3O_{68}$:$Ce^{3+}$,$Dy^{3+}$ phosphors for UV white light-emitting diodes," *J. Solid State Chem.*, vol. 232, pp. 169–177, Dec. 2015, doi: 10.1016/j.jssc.2015.09.015.

[12] K. Lemański, W. Walerczyk, and P. J. Dereń, "Luminescent properties of europium ions in $CaAl_2SiO_6$," *J. Alloys Compd.*, vol. 672, pp. 595–599, Jul. 2016, doi: 10.1016/j.jallcom.2016.02.208.

[13] W. Lv *et al.*, "Crystal Structure and Luminescence Properties of $Ca_8Mg_3Al_2S_7O_{28}$:Eu^{2+} for WLEDs," *Adv. Opt. Mater.*, vol. 2, no. 2, pp. 183–188, Feb. 2014, doi: 10.1002/adom.201300448.

[14] Z. Wang, Y. Wang, P. Zhang, X. Fan, and G. Qian, "Tunable afterglow color in Eu^{2+} and Dy^{3+} co-activated alkaline earth feldspar solid solutions phosphors," *J.*

Lumin., vol. 124, no. 1, pp. 140–142, May 2007, doi: 10.1016/j.jlumin.2006.02.015.

[15] M. Kumar, R. P. Vijayalakshmi, and Y. C. Ratnakaram, "Investigation of structural and optical properties of Pr^{3+} doped and Pr^{3+}/Dy^{3+} co-doped multicomponent bismuth phosphate glasses for visible light applications," *J. Mol. Struct.*, vol. 1265, p. 133333, Oct. 2022, doi: 10.1016/j.molstruc.2022.133333.

[16] Feng Zhang, Zhisong Xiao, Lu Yan, Fang Zhu, and Anping Huang, "Photoluminescence and energy transfer studies of Er^{3+} and Dy^{3+} co-doped tellurite glasses," in *2010 3rd International Nanoelectronics Conference (INEC)*, Jan. 2010, pp. 1467–1468, doi: 10.1109/INEC.2010.5424792.

[17] X. Zhang *et al.*, "Preparation and photoluminescence of SrAl 2 O 4 :Eu^{2+}, Dy^{3+} enamel coatings," Sep. 2002, p. 437, doi: 10.1117/12.483111.

[18] S. Rossi, A. Quaranta, L. Tavella, F. Deflorian, and A. M. Compagnoni, "Innovative Luminescent Vitreous Enameled Coatings," in *Intelligent Coatings for Corrosion Control*, Elsevier Inc., 2015, pp. 251–282.

[19] S. D. Stookey, "History of the Development of Pyroceram," *Res. Manage.*, vol. 1, no. 3, pp. 155–163, Sep. 1958, doi: 10.1080/00345334.1958.11755484.

[20] W. Höland and G. Beall, *Glass-Ceramic Technology*. Wiley, 2019.

[21] F. A. HUMMEL, "Thermal Expansion Properties of Some Synthetic Lithia Minerals," *J. Am. Ceram. Soc.*, vol. 34, no. 8, pp. 235–239, Aug. 1951, doi: 10.1111/j.1151-2916.1951.tb11646.x.

[22] S. D. Stookey, "Catalyzed Crystallization of Glass in Theory and Practice," *Ind. Eng. Chem.*, vol. 51, no. 7, pp. 805–808, Jul. 1959, doi: 10.1021/ie50595a022.

[23] S. Rossi, F. Deflorian, L. Fontanari, A. Cambruzzi, and P. L. Bonora, "Electrochemical measurements to evaluate the damage due to abrasion on organic protective system," *Prog. Org. Coatings*, vol. 52, no. 4, pp. 288–297, Apr. 2005, doi: 10.1016/j.porgcoat.2004.09.005.

[24] V. GÜNAY and Ş. YILMAZ, "Glass Ceramics: Science and Technology (Cam Seramikler: Bilim ve Teknolojisi)," *Met. Derg.*, vol. 23, no. 121, [Online]. Available: https://www.metalurji.org.tr/dergi/dergi121/d121_1217.html.

[25] P. W. McMillan, *Glass-Ceramics*, Second Edi. London: Academic Press, 1979.

[26] T. J. HEADLEY and R. E. LOEHMAN, "Crystallization of a Glass-Ceramic by Epitaxial Growth," *J. Am. Ceram. Soc.*, vol. 67, no. 9, pp. 620–625, Sep. 1984, doi: 10.1111/j.1151-2916.1984.tb19606.x.

[27] J. Shi and X. Feng, "Laser-induced nonlinear crystalline waveguide on glass fiber format and diode-pumped second harmonic generation," *Opt. Fiber Technol.*, vol. 41, pp. 118–124, Mar. 2018, doi: 10.1016/j.yofte.2018.01.015.

[28] J. Deubener *et al.*, "Updated definition of glass-ceramics," *J. Non. Cryst. Solids*, vol. 501, pp. 3–10, Dec. 2018, doi: 10.1016/j.jnoncrysol.2018.01.033.

[29] S. Fujita and S. Tanabe, "Fabrication, microstructure and optical properties of Er^{3+}:YAG glass–ceramics," *Opt. Mater. (Amst).*, vol. 32, no. 9, pp. 886–890, Jul. 2010, doi: 10.1016/j.optmat.2010.01.014.

[30] M. Kamnoy, U. Intatha, A. Munpakdee, S. Eitssayeam, and T. Tunkasiri,

"Mechanical Properties and Microstructure of Li_2O-SiO_2-P_2O_5-Al_2O_3-K_2O-CaO Glass-Ceramics," *Key Eng. Mater.*, vol. 766, pp. 164–169, Apr. 2018, doi: 10.4028/www.scientific.net/KEM.766.164.

[31] G. A. Khater, E. M. Safwat, J. Kang, Y. Yue, and A. G. A. Khater, "Some types of glass-ceramic materials and their applications," *Int. J. Res.*, vol. 7, no. 4, pp. 1–16, 2020.

[32] M. A. González, A. Gorokhovsky, J. I. Escalante, P. Ponce, and M. A. Escobedo, "Crystallization and Properties of Glass-Ceramics of the K_2O-BaO-B_2O_3-Al_2O_3-TiO_2 System," *Mater. Sci. Forum*, vol. 755, pp. 125–132, Apr. 2013, doi: 10.4028/www.scientific.net/MSF.755.125.

[33] G. Partridge, "An overview of glass ceramics. I: Development and principal bulk applications," *Glas. Technol.*, vol. 35, no. 3, pp. 116–127, 1994.

[34] C. Lee, I.-S. Kim, and B. Lee, "Slow crack growth in a cordierite-based glass–ceramic missile radome due to stress corrosion," *Eng. Fail. Anal.*, vol. 93, pp. 76–86, Nov. 2018, doi: 10.1016/j.engfailanal.2018.04.007.

[35] G. H. Beall, "Design and Properties of Glass-Ceramics," *Annu. Rev. Mater. Sci.*, vol. 22, no. 1, pp. 91–119, Aug. 1992, doi: 10.1146/annurev.ms.22.080192.000515.

[36] G. H. Beall, "Dr. S. Donald (Don) Stookey (1915–2014): Pioneering Researcher and Adventurer," *Front. Mater.*, vol. 3, Aug. 2016, doi: 10.3389/fmats.2016.00037.

[37] H. S. Maiti, "Transparent and machinable glass-ceramics," *Handb. Adv. Ceram. Compos. Defense, Secur. Aerosp. Energy Appl.*, pp. 461–493, 2020.

[38] W. OSTERTAG, G. R. FISCHER, and J. P. WILLIAMS, "Thermal Expansion of Synthetic β-Spodumene and β-Spodumene-Silica Solid Solutions," *J. Am. Ceram. Soc.*, vol. 51, no. 11, pp. 651–654, Nov. 1968, doi: 10.1111/j.1151-2916.1968.tb12638.x.

[39] L. Kang, T. Liu, Z. Su, and Y. Kong, "Research on glass ceramics with negative coefficient of thermal expansion used as fiber Bragg grating substrate," May 2004, p. 638, doi: 10.1117/12.520427.

[40] E. El-Meliegy and R. van Noort, *Glasses and Glass Ceramics for Medical Applications*. New York, NY: Springer New York, 2012.

[41] A. Herczog, "Application of Glass-Ceramics for Electronic Components and Circuits," *IEEE Trans. Parts, Hybrids, Packag.*, vol. 9, no. 4, pp. 247–256, Dec. 1973, doi: 10.1109/TPHP.1973.1136735.

[42] A. Sakamoto and S. Yamamoto, "Glass-Ceramics: Engineering Principles and Applications," *Int. J. Appl. Glas. Sci.*, vol. 1, no. 3, pp. 237–247, Sep. 2010, doi: 10.1111/j.2041-1294.2010.00027.x.

[43] H. Wang, J. Liu, J. Zhai, and B. Shen, "Ultra High Energy-Storage Density in the Barium Potassium Niobate-Based Glass-Ceramics for Energy-Storage Applications," *J. Am. Ceram. Soc.*, vol. 99, no. 9, pp. 2909–2912, Sep. 2016, doi: 10.1111/jace.14446.

[44] X. Fu, C. H. Zhang, C. Q. Li, K. J. Li, and Y. B. Zuo, "Design and Processing of Temperature Resistant Enamel Coating Materials," *Appl. Mech. Mater.*, vol. 457–

458, pp. 168–171, Oct. 2013, doi: 10.4028/www.scientific.net/AMM.457-458.168.

[45] L. Samiee, H. Sarpoolaky, and A. Mirhabibi, “Microstructure and adherence of cobalt containing and cobalt free enamels to low carbon steel,” *Mater. Sci. Eng. A*, vol. 458, no. 1–2, pp. 88–95, Jun. 2007, doi: 10.1016/j.msea.2006.12.108.

[46] A. I. Andrew, S. Pagliuca, and W. D. Faust, “Porcelain (Vitreous) Enamels - Industrial Enamelling Processes,” 2011.

[47] E. YILMAZ, “Taban Malzemeye Emaye Arayüz İlişkilerinin Emaye Kalitesine Etkisi,” İstanbul Teknik Üniversitesi, 2014.

[48] S. I. A., B. V. G., F. V. K., G. E. S., and N. A. B., “Influence of initial components mechanical activation on the properties of protective enamel coating on the cast-iron surface,” *J. od Serbian Fed. Univ. Eng. Technol.*, vol. 5, pp. 63–71, 2012.

[49] F. Russo, S. Rossi, and A. M. Compagnoni, “Porcelain Enamel Coatings,” *Encyclopedia*, vol. 1, no. 2, pp. 388–400, Apr. 2021, doi: 10.3390/encyclopedia1020032.

[50] E. Güngör, “Termik Santrallerin Döner Tip Hava Isıtıcılarında Kullanılan Isı Değiştirici Plakalar İçin Emaye Kaplama Optimizasyonu,” İstanbul Teknik Üniversitesi, 2015.

[51] B. KARASU, İ. SAÇKAN, and M. TAPLI, “Emayenin Dünü ve Bugünü,” *El-Cezeri Fen ve Mühendislik Derg.*, May 2019, doi: 10.31202/ecjse.660254.

[52] “Vitreous Enamel Association, ‘VEA,’ Media & Marketing Services and CWN Design.” https://www.vea.org.uk/what-is-enamel (accessed Feb. 15, 2020).

[53] H. T. Queen, “The Vitreous Enameller’s Association, "The Institute of Materials, Minerals and Mining,.” https://www.iom3.org/vitreous-enamellers-society/concise-historyenamel (accessed Feb. 15, 2020).

[54] A. A. Andrews, S. Pagliuca, and W. D. Faust, “Raw materials for enamels,” in *Porcelain Enamels: The Preparation, Application and Properties of Enamels*, Tipografia Commerciale Mantova, 2011.

[55] W. D. Faust, “Porcelain (Vitreous) Enamels and Industrial Enamelling Processes,” 2012.

[56] N. S. C. MILLAR and C. WILSON, “Vitreous Enamel Coatings,” in *Corrosion*, Elsevier, 1994, pp. 16:3-16:12.

[57] E. Scrinzi and S. Rossi, “The aesthetic and functional properties of enamel coatings on steel,” *Mater. Des.*, vol. 31, no. 9, pp. 4138–4146, Oct. 2010, doi: 10.1016/j.matdes.2010.04.030.

[58] ISO, “International Organization for Standardization.” https://www.iso.org/ics/25.220.50/x/. (accessed May 16, 2020).

[59] "IEI The International Enamellers Institute, “No Title.” http://www.iei-world.org/pagine/enamel.asp (accessed Feb. 15, 2020).

[60] R. A. Eppler, *Glazes and glass coatings / by Richard A. Eppler and Douglas R. Eppler*. Westerville, OH: American Ceramic Society, 2000.

[61] R.D. Shanno; and A.L. Freidberg, “Titania Opacified Porcelain Enamels,” *Univ. Illinois Bull.*, vol. 57, 1960.

[62] K. Benzesik, meltem ipekçi Terzioğlu, F. Şahin, and O. Yücel, "Optimizing the Migration Behavior of Enamel Coatings Used as Food Contact Materials," 2018, [Online]. Available: https://www.researchgate.net/publication/329327438.

[63] A. P. Tomsia and J. A. Pask, "Chemical reactions and adherence at glass/metal interfaces: an analysis," *Dent. Mater.*, vol. 2, no. 1, pp. 10–16, 1986.

[64] A. H. Dietzel, *Emaillierung*. Berlin, Heidelberg: Springer Berlin Heidelberg, 1981.

[65] A. Zucchelli, M. Dignatici, M. Montorsi, R. Carlotti, and C. Siligardi, "Characterization of vitreous enamel–steel interface by using hot stage ESEM and nano-indentation techniques," *J. Eur. Ceram. Soc.*, vol. 32, no. 10, pp. 2243–2251, Aug. 2012, doi: 10.1016/j.jeurceramsoc.2012.03.008.

[66] A. I. Andrew, S. Pagliuca, and W. D. Faust, "Enamel Properties and Tests, Porcelain (Vitreous) Enamels and Industrial Enamelling Processes The Preparation, Application and Properties of Enamels," 2011.

[67] A. I. Andrew, S. Pagliuca, and W. D. Faust, "Fundamentals and Cosiderations, Porcelain (Vitreous) Enamels and Industrial Enamelling Processes The Preparation, Application and Properties of Enamels," 2011.

[68] ASTM - American Society for Testing and Materials International, *ASTM C385-58(2018), Standard Test Method for Thermal Shock Resistance of Porcelain-Enameled Utensils*. 2018.

[69] M. Shu, H. Yin, Q. Zhong, X. Shi, And H. Han, "Effect Of Glass Powder On Acid Resistance Of Enamel Coating," *Surf. Rev. Lett.*, Vol. 24, No. 03, P. 1750036, Apr. 2017, Doi: 10.1142/S0218625x17500366.

[70] S. G. Schäfer and V. E. Annamalai, "Degradation of Glass Linings and Coatings," in *Reference Module in Materials Science and Materials Engineering*, Elsevier, 2016.

[71] A. I. Andrew, S. Pagliuca, and W. D. Faust, "'Chemical and Electrical Properties,' in Porcelain (Vitreous) Enamels and Industrial Enamelling Processes The Preparation, Application and Properties of Enamels," 2011.

[72] P. W. McMillan, "Crystallization of a Glass-Ceramic by Epitaxial Growth," London, 1979.

[73] A. I. Andrew, S. Pagliuca, and W. D. Faust, "'Milling and Milling Additions,' in Porcelain (Vitreous) Enamels and Industrial Enamelling Processes The Preparation, Application and Properties of Enamels," 2011, pp. 389–420.

[74] S. Baycık, "Granüle Yüksek Fırın Cüruflarının Karo Sektöründe Kullanılabilirliğinin Araştırılması," İstanbul Technical University, 2003.

[75] A. Mittal, "Steel for enamelling and enamelled steel," *(User Manual)*, 2014.

[76] A. Davran, "Enamelling Applications On Metal From Past to Future," IZMIR UNIVERSITY, 2011.

[77] S. Paytuncu, "Emaye Okulu Ders Notları," 2011, pp. 145–149.

[78] A. Çavuşoğlu, "Emaye okulu ders notları, II," in *International Ceramic, Glass, Porcelain Enamel, Glaze and Pigment Congress*, 2011, vol. 11, pp. 13–36.

[79] T. Zhang, Y. Bao, and D. T. Gawne, "Process model of plasma enamelling," *J. Eur. Ceram. Soc.*, vol. 23, no. 7, pp. 1019–1026, Jun. 2003, doi: 10.1016/S0955-

2219(02)00235-2.

[80] A. Yıldız, Ö. Genç, and S. Bektaş, "Enstrümental Analiz Yöntemleri," *Hacettepe Üniversitesi Yayınları*, ANKARA, 1997.

[81] B. Valeur and M. N. Berberan-Santos, "A Brief History of Fluorescence and Phosphorescence before the Emergence of Quantum Theory," *J. Chem. Educ.*, vol. 88, no. 6, pp. 731–738, Jun. 2011, doi: 10.1021/ed100182h.

[82] W. M. Yen and M. J. Weber, *Inorganic Phosphors*. CRC Press, 2004.

[83] J. Hölsä, "Persistent Luminescence Beats the Afterglow: 400 Years of Persistent Luminescence," *Electrochem. Soc. Interface*, vol. 18, no. 4, pp. 42–45, Dec. 2009, doi: 10.1149/2.F06094IF.

[84] E. Wiedemann, "Ueber Fluorescenz und Phosphorescenz I. Abhandlung," *Ann. der Phys. und Chemie*, vol. 270, no. 7, pp. 446–463, 1888, doi: 10.1002/andp.18882700703.

[85] M. Lastusaari *et al.*, "The Bologna Stone: history's first persistent luminescent material," *Eur. J. Mineral.*, vol. 24, no. 5, pp. 885–890, Sep. 2012, doi: 10.1127/0935-1221/2012/0024-2224.

[86] J. Xu and S. Tanabe, "Persistent luminescence instead of phosphorescence: History, mechanism, and perspective," *J. Lumin.*, vol. 205, pp. 581–620, Jan. 2019, doi: 10.1016/j.jlumin.2018.09.047.

[87] T. Sidot, "Recherches sur la crystallisation de quelque sulphures métalliques et sur les propriétés de la blende hexagonale," *Comptes Rend. Ac. Sci*, vol. 62, pp. 999–1001, 1866.

[88] P. F. Smet, J. Botterman, K. Van den Eeckhout, K. Korthout, and D. Poelman, "Persistent luminescence in nitride and oxynitride phosphors: A review," *Opt. Mater. (Amst).*, vol. 36, no. 11, pp. 1913–1919, Sep. 2014, doi: 10.1016/j.optmat.2014.05.026.

[89] R. E. Rojas-Hernandez, F. Rubio-Marcos, M. Á. Rodriguez, and J. F. Fernandez, "Long lasting phosphors: $SrAl_2O_4$:Eu, Dy as the most studied material," *Renew. Sustain. Energy Rev.*, vol. 81, pp. 2759–2770, Jan. 2018, doi: 10.1016/j.rser.2017.06.081.

[90] M. Akiyama, C.-N. Xu, Y. Liu, K. Nonaka, and T. Watanabe, "Influence of Eu, Dy co-doped strontium aluminate composition on mechanoluminescence intensity," *J. Lumin.*, vol. 97, no. 1, pp. 13–18, Apr. 2002, doi: 10.1016/S0022-2313(01)00419-7.

[91] S. Abe, K. Uematsu, K. Toda, and M. Sato, "Luminescent properties of red long persistence phosphors, $BaMg_2Si_2O_7$:Eu^{2+}, Mn^{2+}," *J. Alloys Compd.*, vol. 408–412, pp. 911–914, Feb. 2006, doi: 10.1016/j.jallcom.2005.03.092.

[92] M. JUNG, W. PARK, and D. YOON, "Photoluminescence characteristics of red phosphor Eu^{3+}, Sm^{3+} co-doped Y_2O_3 for white light emitting diodes," *Sensors Actuators B Chem.*, vol. 126, no. 1, pp. 328–331, Sep. 2007, doi: 10.1016/j.snb.2007.02.032.

[93] C. Yuesheng, Z. Ping, and Z. Zhentai, "Eu^{2+} and Dy^{3+} co-doped $Sr_3Al_2O_6$ red long-afterglow phosphors with new flower-like morphology," *Phys. B Condens. Matter*, vol. 403, no. 21–22, pp. 4120–4122, Nov. 2008, doi: 10.1016/j.physb.2008.08.011.

[94] J. Xu, S. Tanabe, A. D. Sontakke, and J. Ueda, “Near-infrared multi-wavelengths long persistent luminescence of Nd^{3+} ion through persistent energy transfer in Ce^{3+}, Cr^{3+} co-doped $Y_3Al_2Ga_3O_{12}$ for the first and second bio-imaging windows,” *Appl. Phys. Lett.*, vol. 107, no. 8, p. 81903, 2015.

[95] H. Kanno, K. Noda, and K. Matsui, “New long-afterglow phosphors: Yb^{2+}-doped strontium aluminates,” *Chem. Phys. Lett.*, vol. 580, pp. 103–107, Aug. 2013, doi: 10.1016/j.cplett.2013.06.064.

[96] P. Głuchowski, W. Stręk, M. Lastusaari, and J. Hölsä, “Optically stimulated persistent luminescence of europium-doped $LaAlO_3$ nanocrystals,” *Phys. Chem. Chem. Phys.*, vol. 17, no. 26, pp. 17246–17252, 2015.

[97] N. Basavaraju, K. R. Priolkar, D. Gourier, A. Bessière, and B. Viana, “Order and disorder around Cr^{3+} in chromium doped persistent luminescent AB_2O_4 spinels,” *Phys. Chem. Chem. Phys.*, vol. 17, no. 16, pp. 10993–10999, 2015.

[98] H. Wu, Y. Hu, L. Chen, and X. Wang, “Enhancement on the afterglow properties of $Sr_2MgSi_2O_7$: Eu^{2+} by Er^{3+} codoping,” *Mater. Lett.*, vol. 65, no. 17–18, pp. 2676–2679, Sep. 2011, doi: 10.1016/j.matlet.2011.05.079.

[99] P. I. Paulose, “Luminescence studies of certain doped phosphors and classy materials,” 2002.

[100] P. I. Paulose, “Luminescence Studie of certain Doped Phosphors and Glassy Material, School of Pure&Applied Physics,” *Mamatha Gandhi Univ. Phd. Thesis*, vol. 137, 2002.

[101] K. Van den Eeckhout, P. F. Smet, and D. Poelman, “Persistent Luminescence in Eu^{2+}-Doped Compounds: A Review,” *Materials (Basel).*, vol. 3, no. 4, pp. 2536–2566, Apr. 2010, doi: 10.3390/ma3042536.

[102] T. Aitasalo *et al.*, “Persistent luminescence and synchrotron radiation study of the : materials,” *Radiat. Meas.*, vol. 42, no. 4–5, pp. 644–647, Apr. 2007, doi: 10.1016/j.radmeas.2007.01.058.

[103] S. K. Singh, “Red and near infrared persistent luminescence nano-probes for bioimaging and targeting applications,” *RSC Adv.*, vol. 4, no. 102, pp. 58674–58698, 2014, doi: 10.1039/C4RA08847F.

[104] Y. Li *et al.*, “Tailoring of the trap distribution and crystal field in Cr^{3+}-doped non-gallate phosphors with near-infrared long-persistence phosphorescence,” *NPG Asia Mater.*, vol. 7, no. 5, pp. e180–e180, May 2015, doi: 10.1038/am.2015.38.

[105] H. Yamamoto and T. Matsuzawa, “Mechanism of long phosphorescence of $SrAl_2O_4$:Eu^{2+}, Dy^{3+} and CaAl2O4:Eu^{2+}, Nd^{3+},” *J. Lumin.*, vol. 72–74, pp. 287–289, Jun. 1997, doi: 10.1016/S0022-2313(97)00012-4.

[106] T. Nakamura *et al.*, “High frequency EPR of europium(ii)-doped strontium aluminate phosphors,” *J. Mater. Chem.*, vol. 10, no. 11, pp. 2566–2569, 2000, doi: 10.1039/b004061o.

[107] Y. Li, M. Gecevicius, and J. Qiu, “Long persistent phosphors—from fundamentals to applications,” *Chem. Soc. Rev.*, vol. 45, no. 8, pp. 2090–2136, 2016, doi: 10.1039/C5CS00582E.

[108] T. Aitasalo *et al.*, “Persistent luminescence phenomena in materials doped with rare earth ions,” *J. Solid State Chem.*, vol. 171, no. 1–2, pp. 114–122, Feb. 2003,

doi: 10.1016/S0022-4596(02)00194-9.

[109] J. Hölsä, T. Aitasalo, H. Jungner, M. Lastusaari, J. Niittykoski, and G. Spano, "Role of defect states in persistent luminescence materials," *J. Alloys Compd.*, vol. 374, no. 1–2, pp. 56–59, Jul. 2004, doi: 10.1016/j.jallcom.2003.11.064.

[110] P. Dorenbos, "Energy of the first $^4f_7 \rightarrow {}^4f_6{}^5d$ transition of Eu^{2+} in inorganic compounds," *J. Lumin.*, vol. 104, no. 4, pp. 239–260, Aug. 2003, doi: 10.1016/S0022-2313(03)00078-4.

[111] P. Dorenbos, "The Eu^{3+} charge transfer energy and the relation with the band gap of compounds," *J. Lumin.*, vol. 111, no. 1–2, pp. 89–104, Jan. 2005, doi: 10.1016/j.jlumin.2004.07.003.

[112] H. Yuasa and S. Kuno, "Intersystem Crossing Mechanisms in the Room Temperature Phosphorescence of Crystalline Organic Compounds," *Bull. Chem. Soc. Jpn.*, vol. 91, no. 2, pp. 223–229, Feb. 2018, doi: 10.1246/bcsj.20170364.

[113] K. A. Gschneidner, J.-C. G. Bunzli, and V. K. Pecharsky, *Handbook on the physics and chemistry of rare earths*, vol. 34. Elsevier, 2005.

[114] M. Lastusaari *et al.*, "Wavelength-sensitive energy storage in $Sr_3MgSi_2O_8:Eu^{2+},Dy^{3+}$," *J. Therm. Anal. Calorim.*, vol. 121, no. 1, pp. 29–35, Jul. 2015, doi: 10.1007/s10973-015-4571-7.

[115] J. Yan *et al.*, "Luminescence and electronic properties of $Ba_2MgSi_2O_7:Eu^{2+}$: a combined experimental and hybrid density functional theory study," *J. Mater. Chem. C*, vol. 2, no. 39, pp. 8328–8332, 2014, doi: 10.1039/C4TC01332H.

[116] Y. Li, Y. Wang, Y. Gong, X. Xu, and M. Zhou, "Design, synthesis and characterization of an orange-yellow long persistent phosphor: $Sr_3Al_2O_5Cl_2:Eu^{2+},Tm^{3+}$," *Opt. Express*, vol. 18, no. 24, p. 24853, Nov. 2010, doi: 10.1364/OE.18.024853.

[117] H. Lin *et al.*, "Bandgap Tailoring via Si Doping in Inverse-Garnet $Mg_3Y_2Ge_3O_{12}:Ce^{3+}$ Persistent Phosphor Potentially Applicable in AC-LED," *ACS Appl. Mater. Interfaces*, vol. 7, no. 39, pp. 21835–21843, Oct. 2015, doi: 10.1021/acsami.5b06071.

[118] L. L. Noto, S. S. Pitale, M. A. Gusowki, J. J. Terblans, O. M. Ntwaeaborwa, and H. C. Swart, "Afterglow enhancement with In3+ codoping in $CaTiO_3:Pr^{3+}$ red phosphor," *Powder Technol.*, vol. 237, pp. 141–146, Mar. 2013, doi: 10.1016/j.powtec.2013.01.029.

[119] P. Boutinaud, L. Sarakha, and R. Mahiou, "$NaNbO_3:Pr^{3+}$: a new red phosphor showing persistent luminescence," *J. Phys. Condens. Matter*, vol. 21, no. 2, p. 025901, Jan. 2009, doi: 10.1088/0953-8984/21/2/025901.

[120] Y. Jin, Y. Hu, L. Chen, X. Wang, G. Ju, and Z. Mou, "Luminescence Properties of Dual-Emission (UV/Visible) Long Afterglow Phosphor $SrZrO_3:Pr^{3+}$," *J. Am. Ceram. Soc.*, vol. 96, no. 12, pp. 3821–3827, Dec. 2013, doi: 10.1111/jace.12590.

[121] L. C. V. Rodrigues *et al.*, "Discovery of the Persistent Luminescence Mechanism of $CdSiO_3:Tb^{3+}$," *J. Phys. Chem. C*, vol. 116, no. 20, pp. 11232–11240, May 2012, doi: 10.1021/jp212021k.

[122] R. Pang *et al.*, "Luminescence properties of a novel reddish orange long-lasting phosphorescence phosphor $Zn_2P_2O_7:Sm^{3+}$,Li^+," *RSC Adv.*, vol. 5, no. 101, pp.

82704–82710, 2015, doi: 10.1039/C5RA14589A.

[123] R. Pang *et al.*, “Tunable long lasting phosphorescence due to the selective energy transfer from defects to luminescent centres via tunnelling in Mn^{2+} and Tm^{3+} co-doped zinc pyrophosphate,” *Dalt. Trans.*, vol. 43, no. 25, p. 9661, 2014, doi: 10.1039/c4dt00223g.

[124] Y. Tokiwa, C. Stingl, M.-S. Kim, T. Takabatake, and P. Gegenwart, “Characteristic signatures of quantum criticality driven by geometrical frustration,” *Sci. Adv.*, vol. 1, no. 3, Apr. 2015, doi: 10.1126/sciadv.1500001.

[125] Y. Yang *et al.*, “A novel Yb^{2+} doped SrS long persistent luminescence phosphors,” *Opt. Mater. (Amst).*, vol. 36, no. 11, pp. 1822–1825, Sep. 2014, doi: 10.1016/j.optmat.2014.04.029.

[126] W. M. Yen, S. Shionaya, and H. Yamamoto, *Phosphor Handbook*, Second Edi. tokyo: CRC Press, 2006.

[127] W. M. Yen, S. Shionaya, and H. Yamamoto, *Phosphor Handbook*, Second Edi. Tokyo: CRC Press, 2006.

[128] W. M. Yen, S. Shionaya, and H. Yamamoto, *Phosphor Handbook*, Second Edi. tokyo, 2006.

[129] W. M. Yen, S. Shionaya, and H. Yamamoto, *Phosphor Handbook*, Second Edi. tokyo: CRC Press, 2006.

[130] ISO, “Vitreous and porcelain enamels — Determination of resistance to chemical corrosion — Part 2: Determination of resistance to chemical corrosion by boiling acids, boiling neutral liquids, alkaline liquids and/or their vapours,” Geneve, 2017.

[131] ISO, “ISO 2813 - Paints and varnishes. Determination of gloss value at 20 degrees, 60 degrees and 85 degrees,” Geneve, 2014.

[132] W. H. Zachariasen, “The Atomic Arrangement In Glass,” *J. Am. Chem. Soc.*, Vol. 54, No. 10, Pp. 3841–3851, Oct. 1932, Doi: 10.1021/ja01349a006.

[133] A. Rupesh Kumar, T. G. V. M. Rao, N. Veeraiah, and M. Rami Reddy, “Fluorescence spectroscopic studies of Mn^{2+} ions in $SrO–Al_2O_3–B_2O_3–SiO_2$ glass system,” *Opt. Mater. (Amst).*, vol. 35, no. 3, pp. 402–406, Jan. 2013, doi: 10.1016/j.optmat.2012.09.008.

[134] A. Belkébir *et al.*, “Structural characterisation of glassy phases in the system $Na_2O–Al_2O_3–P_2O_5$ by MAS and solution NMR, EXAFS and vibrational spectroscopy,” *Spectrochim. Acta Part A Mol. Biomol. Spectrosc.*, vol. 55, no. 7–8, pp. 1323–1336, Jul. 1999, doi: 10.1016/S1386-1425(98)00316-3.

[135] Y. Gandhi, M. V. R. Rao, C. S. Rao, T. Srikumar, I. V. Kityk, and N. Veeraiah, “Influence of aluminum ions on fluorescent spectra and upconversion in codoped $CaF_2–Al_2O_3–P_2O_5–SiO_2$:$Ho^{3+}$ and Er^{3+} glass system,” *J. Appl. Phys.*, vol. 108, no. 2, p. 023102, Jul. 2010, doi: 10.1063/1.3464257.

[136] I. A. Severenkov, E. V. Ustyugova, L. A. Alekseeva, T. V. Zaichuk, and Y. A. Spiridonov, “Glass Formation and Crystallization in Strontium-Aluminum-Silicate Glass: Influence of Modifying Additives on Melting and Crystallization,” *Glas. Ceram.*, vol. 78, no. 7–8, pp. 259–263, Nov. 2021, doi: 10.1007/s10717-021-00392-y.

[137] C. Zhang, F. Zhang, W. S. Cao, and Y. A. Chang, “Thermodynamic modeling of

the Al–Si–Sr–O quaternary system," *Intermetallics*, vol. 18, no. 8, pp. 1419–1427, Aug. 2010, doi: 10.1016/j.intermet.2010.01.032.

[138] P. K. Ojha, S. K. Rath, T. K. Chongdar, N. M. Gokhale, and A. R. Kulkarni, "Physical and thermal behaviour of Sr–La–Al–B–Si based SOFC glass sealants as function of SrO content and B_2O_3/SiO_2 ratio in the matrix," *J. Power Sources*, vol. 196, no. 10, pp. 4594–4598, May 2011, doi: 10.1016/j.jpowsour.2011.01.021.

[139] Y. Wu, L. Zhu, and H. Mao, "Tunable luminescence and energy transfer for $Ce^{3+}/Tb^{3+}/Sm^{3+}$ doped $SrAl_2Si_2O_8$ phosphors," *Ceram. Int.*, vol. 44, no. 8, pp. 10015–10019, Jun. 2018, doi: 10.1016/j.ceramint.2018.03.030.

[140] I. Daniel, P. Gillet, and S. GHOSE, "A new high-pressure phase transition in anorthite ($CaAI_2Si_2O_8$) revealed by Raman spectroscopy," *Am. Mineral.*, vol. 80, pp. 645–648, Jun. 1995.

[141] J. J. Freeman, A. Wang, K. E. Kuebler, B. L. Jolliff, And L. A. Haskin, "Characterization Of Natural Feldspars By Raman Spectroscopy For Future Planetary Exploration," *Can. Mineral.*, Vol. 46, No. 6, Pp. 1477–1500, Dec. 2008, Doi: 10.3749/Canmin.46.6.1477.

[142] L. A. Gorelova, S. K. Filatov, M. G. Krzhizhanovskaya, and R. S. Bubnova, "High temperature behaviour of danburite-like borosilicates $MB_2Si_2O_8$ (M=Ca, Sr, Ba)," *Phys. Chem. Glas. Eur. J. Glas. Sci. Technol. Part B*, vol. 56, no. 5, pp. 189–196, Oct. 2015, doi: 10.13036/17533562.56.5.189.

[143] L. A. Gorelova, A. S. Pakhomova, S. V. Krivovichev, L. S. Dubrovinsky, and A. V. Kasatkin, "High pressure phase transitions of paracelsian $BaAl_2Si_2O_8$," *Sci. Rep.*, vol. 9, no. 1, p. 12652, Sep. 2019, doi: 10.1038/s41598-019-49112-1.

[144] L. A. Gorelova, A. S. Pakhomova, M. G. Krzhizhanovskaya, B. Winkler, S. V. Krivovichev, and L. S. Dubrovinsky, "Pressure-Induced Phase Transitions in Danburite-Type Borosilicates," *J. Phys. Chem. C*, vol. 124, no. 47, pp. 26048–26061, Nov. 2020, doi: 10.1021/acs.jpcc.0c08616.

[145] A. Pakhomova *et al.*, "A closer look into close packing: pentacoordinated silicon in a high-pressure polymorph of danburite," *IUCrJ*, vol. 4, no. 5, pp. 671–677, Sep. 2017, doi: 10.1107/S2052252517010612.

[146] L. A. Gorelova *et al.*, "Crystal Structure Evolution of Slawsonite $SrAl_2Si_2O_8$ and Paracelsian $BaAl_2Si_2O_8$ upon Compression and Decompression," *J. Phys. Chem. C*, vol. 125, no. 23, pp. 13014–13023, Jun. 2021, doi: 10.1021/acs.jpcc.1c02949.

[147] J. Zhao, L. Lei, R. Ye, J. Zhang, X. Zhang, and S. Xu, "Sunlight activated ultra-stable long persistent luminescence glass ceramic for outdoor information display," *J. Adv. Ceram.*, vol. 11, no. 6, pp. 974–983, Jun. 2022, doi: 10.1007/s40145-022-0595-1.

[148] D. R. Neuville, L. Cormier, and D. Massiot, "Al coordination and speciation in calcium aluminosilicate glasses: Effects of composition determined by 27Al MQ-MAS NMR and Raman spectroscopy," *Chem. Geol.*, vol. 229, no. 1–3, pp. 173–185, May 2006, doi: 10.1016/j.chemgeo.2006.01.019.

[149] P. McMillan, B. Piriou, and A. Navrotsky, "A Raman spectroscopic study of glasses along the joins silica-calcium aluminate, silica-sodium aluminate, and silica-potassium aluminate," *Geochim. Cosmochim. Acta*, vol. 46, no. 11, pp. 2021–2037, Nov. 1982, doi: 10.1016/0016-7037(82)90182-X.

[150] A. Atila, S. Ouaskit, and A. Hasnaoui, “Ionic self-diffusion and the glass transition anomaly in aluminosilicates,” *Phys. Chem. Chem. Phys.*, vol. 22, no. 30, pp. 17205–17212, 2020, doi: 10.1039/D0CP02910F.

[151] C. Romano, B. Poe, V. Mincione, K. U. Hess, and D. B. Dingwell, “The viscosities of dry and hydrous $XAlSi_3O_8$ (X=Li, Na, K, $Ca_{0.5}$, $Mg_{0.5}$) melts,” *Chem. Geol.*, vol. 174, no. 1–3, pp. 115–132, Apr. 2001, doi: 10.1016/S0009-2541(00)00311-9.

[152] A. Atila, E. M. Ghardi, S. Ouaskit, and A. Hasnaoui, “Atomistic insights into the impact of charge balancing cations on the structure and properties of aluminosilicate glasses,” *Phys. Rev. B*, vol. 100, no. 14, p. 144109, Oct. 2019, doi: 10.1103/PhysRevB.100.144109.

[153] A. Navrotsky, K. L. Geisinger, P. McMillan, and G. V. Gibbs, “The tetrahedral framework in glasses and melts - inferences from molecular orbital calculations and implications for structure, thermodynamics, and physical properties,” *Phys. Chem. Miner.*, vol. 11, no. 6, pp. 284–298, Jan. 1985, doi: 10.1007/BF00307406/METRICS.

[154] J. F. Sousa, A. C. A. Silva, N. O. Dantas, F. G. Rego-Filho, and A. S. Gouveia-Neto, “Luminescence and energy-transfer analysis in Dy^{3+}/Pr^{3+}-codoped TeO_2:ZnO glass,” *J. Lumin.*, vol. 226, p. 117466, Oct. 2020, doi: 10.1016/j.jlumin.2020.117466.

[155] S. A. Saleem, B. C. Jamalaiah, M. Jayasimhadri, A. Srinivasa Rao, K. Jang, and L. Rama Moorthy, “Luminescent studies of Dy^{3+} ion in alkali lead tellurofluoroborate glasses,” *J. Quant. Spectrosc. Radiat. Transf.*, vol. 112, no. 1, pp. 78–84, Jan. 2011, doi: 10.1016/j.jqsrt.2010.08.017.

[156] K. V. Krishnaiah, K. U. Kumar, and C. K. Jayasankar, “Spectroscopic properties of Dy^{3+}-doped oxyfluoride glasses for white light emitting diodes,” *Mater. Express*, vol. 3, no. 1, pp. 61–70, Mar. 2013, doi: 10.1166/mex.2013.1094.

[157] J. Li, J.-G. Li, S. Liu, X. Li, X. Sun, and Y. Sakka, “Greatly enhanced Dy^{3+} emission via efficient energy transfer in gadolinium aluminate garnet ($Gd_3Al_5O_{12}$) stabilized with Lu3+,” *J. Mater. Chem. C*, vol. 1, no. 45, p. 7614, 2013, doi: 10.1039/c3tc31413h.

[158] M. Yu *et al.*, “Fabrication, Patterning, and Optical Properties of Nanocrystalline YVO_4:A (A = Eu^{3+}, Dy^{3+}, Sm^{3+}, Er^{3+}) Phosphor Films via Sol−Gel Soft Lithography,” *Chem. Mater.*, vol. 14, no. 5, pp. 2224–2231, May 2002, doi: 10.1021/cm011663y.

[159] A. M. Srivastava, M. Jennings, and J. Collins, “The interconfigurational ($^4f_1{}^5d_1 \rightarrow {}^4f_2$) luminescence of Pr^{3+} in $LuPO_4$, $K_3Lu(PO_4)_2$ and $LiLuSiO_4$,” *Opt. Mater. (Amst).*, vol. 34, no. 8, pp. 1347–1352, Jun. 2012, doi: 10.1016/j.optmat.2012.02.016.

[160] K. A. Bashar *et al.*, “Tunable white-light emission from Pr^{3+}/Dy^{3+} co-doped B_2O_3 - TeO_2 PbO - ZnO Li_2O - Na_2O glasses,” *Opt. Mater. (Amst).*, vol. 88, pp. 558–569, Feb. 2019, doi: 10.1016/j.optmat.2018.12.028.

[161] P. P. Pawar, S. R. Munishwar, and R. S. Gedam, “Physical and optical properties of Dy^{3+}/Pr^{3+} Co-doped lithium borate glasses for W-LED,” *J. Alloys Compd.*, vol. 660, pp. 347–355, Mar. 2016, doi: 10.1016/j.jallcom.2015.11.087.

[162] E. F. Schubert, *Light-Emitting Diodes*. Cambridge University Press, 2006.

[163] Q. . Zhang, K. Pita, W. Ye, and W. . Que, “Influence of annealing atmosphere and temperature on photoluminescence of Tb^{3+} or Eu^{3+}-activated zinc silicate thin film phosphors via sol–gel method,” *Chem. Phys. Lett.*, vol. 351, no. 3–4, pp. 163–170, Jan. 2002, doi: 10.1016/S0009-2614(01)01370-7.

[164] W. R. Stevens, *Building physics: lighting: seeing in the artificial environment*. Elsevier, 2013.

[165] N. V. and N. Lee, “Dy^{3+}/Pr^{3+} co-doped fluoro-borosilicate glasses: Energy transfer induced color-tunable luminescence,” *Mater. Res. Bull.*, vol. 142, p. 111381, Oct. 2021, doi: 10.1016/j.materresbull.2021.111381.

[166] D. K. Sardar, D. M. Dee, K. L. Nash, R. M. Yow, J. B. Gruber, and R. Debnath, “Optical characterization and ligand-field splitting of Er^{3+}($^4f_{11}$) energy levels in a fluorine containing tellurite glass,” *J. Appl. Phys.*, vol. 102, no. 8, p. 083105, Oct. 2007, doi: 10.1063/1.2799073.

[167] C. R. Kesavulu *et al.*, “Influence of Er^{3+} ion concentration on optical and photoluminescence properties of Er^{3+}-doped gadolinium-calcium silica borate glasses,” *J. Alloys Compd.*, vol. 683, pp. 590–598, Oct. 2016, doi: 10.1016/j.jallcom.2016.04.314.

[168] G. Lakshminarayana *et al.*, “Er^{3+}/Dy^{3+} codoped B_2O_3-TeO_2-PbO-ZnO-Li_2O-Na_2O glasses: Optical absorption and fluorescence features study for visible and near-infrared fiber laser applications,” *J. Non. Cryst. Solids*, vol. 503–504, pp. 366–381, Jan. 2019, doi: 10.1016/j.jnoncrysol.2018.10.025.

[169] X. Hu, S. Yi, B. Liang, G. Hu, and Y. Wang, “Synthesis and photoluminescence properties of Er^{3+} and Dy^{3+} doped Na_2NbAlO_5 phosphors,” *J. Rare Earths*, vol. 36, no. 8, pp. 789–794, Aug. 2018, doi: 10.1016/j.jre.2018.01.013.

[170] F. Zhang, Z. Xiao, L. Yan, F. Zhu, and A. Huang, “Visible luminescence properties of Er^{3+}–Dy^{3+} codoped tellurite glasses,” *Appl. Phys. A*, vol. 101, no. 4, pp. 777–780, Dec. 2010, doi: 10.1007/s00339-010-5966-8.

PUBLICATIONS

Conference Papers

1. “Investigation of Luminescent Behaviour of Er^{3+} Doped SrO-Al_2O_3-SiO_2-Based Glass-Ceramic Coatings” Soylu A., Kaya M., Cengiz T., Cicek B., V. International Ceramic, Glass, Enamel, Glaze and Paint Congress (SERES’21), Eskisehir, Turkey, 13-15.10.2021, seres2021.org.

2. “Glass-Ceramic Coating for Whiteboard Applications” Soylu A., Copoglu N., Cengiz T., Cicek B., 14th ECerS Conference for Young Scientists in Ceramics (CYCS-21), 20-23.10.2021, Novi Sad, Serbia, Book of Abstract, ISBN 978-86-6253-136-0